



Open Access Articles

Uniform California Earthquake Rupture Forecast, Version 3 (UCERF3) —The Time-Independent Model

The Faculty of Oregon State University has made this article openly available.
Please share how this access benefits you. Your story matters.

Citation	Field, E. H., Arrowsmith, R. J., Biasi, G. P., Bird, P., Dawson, T. E., Felzer, K. R., ... & Zeng, Y. (2014). Uniform California Earthquake Rupture Forecast, Version 3 (UCERF3)—The Time-Independent Model. Bulletin of the Seismological Society of America, 104(3), 1122-1180. doi:10.1785/0120130164
DOI	10.1785/0120130164
Publisher	Seismological Society of America
Version	Version of Record
Terms of Use	http://cdss.library.oregonstate.edu/sa-termsofuse

Uniform California Earthquake Rupture Forecast, Version 3 (UCERF3) —The Time-Independent Model

by Edward H. Field, Ramon J. Arrowsmith, Glenn P. Biasi, Peter Bird, Timothy E. Dawson, Karen R. Felzer, David D. Jackson, Kaj M. Johnson, Thomas H. Jordan, Christopher Madden, Andrew J. Michael, Kevin R. Milner, Morgan T. Page, Tom Parsons, Peter M. Powers, Bruce E. Shaw, Wayne R. Thatcher, Ray J. Weldon II, and Yuehua Zeng

Abstract The 2014 Working Group on California Earthquake Probabilities (WGCEP14) present the time-independent component of the Uniform California Earthquake Rupture Forecast, Version 3 (UCERF3), which provides authoritative estimates of the magnitude, location, and time-averaged frequency of potentially damaging earthquakes in California. The primary achievements have been to relax fault segmentation and include multifault ruptures, both limitations of UCERF2. The rates of all earthquakes are solved for simultaneously and from a broader range of data, using a system-level inversion that is both conceptually simple and extensible. The inverse problem is large and underdetermined, so a range of models is sampled using an efficient simulated annealing algorithm. The approach is more derivative than prescriptive (e.g., magnitude–frequency distributions are no longer assumed), so new analysis tools were developed for exploring solutions. Epistemic uncertainties were also accounted for using 1440 alternative logic-tree branches, necessitating access to supercomputers. The most influential uncertainties include alternative deformation models (fault slip rates), a new smoothed seismicity algorithm, alternative values for the total rate of $M_w \geq 5$ events, and different scaling relationships, virtually all of which are new. As a notable first, three deformation models are based on kinematically consistent inversions of geodetic and geologic data, also providing slip-rate constraints on faults previously excluded due to lack of geologic data. The grand inversion constitutes a system-level framework for testing hypotheses and balancing the influence of different experts. For example, we demonstrate serious challenges with the Gutenberg–Richter hypothesis for individual faults. UCERF3 is still an approximation of the system, however, and the range of models is limited (e.g., constrained to stay close to UCERF2). Nevertheless, UCERF3 removes the apparent UCERF2 overprediction of M 6.5–7 earthquake rates and also includes types of multifault ruptures seen in nature. Although UCERF3 fits the data better than UCERF2 overall, there may be areas that warrant further site-specific investigation. Supporting products may be of general interest, and we list key assumptions and avenues for future model improvements.

Manuscript Organization

Because of manuscript length and model complexity, we begin with an outline of this report to help readers navigate the various sections:

1. Introduction

- Background
- Model Framework
- Model Uncertainties
- Participants, Review, and Consensus Building

2. Fault Models

- Definition

- Fault Zone Polygons

- Logic-Tree Branches

- Development Process

3. Deformation Models

- Geologic Slip Rate Constraints

- Geologic Deformation Model

- Deformation Models from Joint Inversion of Geodetic and Geologic Data

- Creep and Aseismicity

- Implied Moment Rates
- Logic-Tree Branch Weights
- 4. Earthquake Rate Models and the “Grand Inversion”
 - Methodology
 - Implementation Ingredients
 - Inversion Setup and Associated Gridded Seismicity
 - Gardner–Knopoff Aftershock Filter
- 5. Results
 - Model Evaluation Challenges
 - Model Fits to Data
 - Fits to Data Not Used in the Inversion
 - Hazard-Related Metrics
 - Sensitivity Tests
- 6. Discussion
 - Improvements Over UCERF2
 - Model Limitations
 - Future Improvements
- 7. Conclusions and Recommendations
- 8. Data and Resources
- 9. Acknowledgments
- 10. References

Except where noted, all magnitudes (M) referenced here represent moment magnitude.

Introduction

Background

The 38 million residents of California live among some of the most active earthquake faults in the United States, so efforts to promote public safety and community resilience require credible assessments of the earthquake hazard. The best tool for quantifying the earthquake threat is probabilistic seismic-hazard analysis (PSHA; see Table 1 for list of acronyms), which quantifies the likelihood that ground shaking will exceed various levels during a given time period (Cornell, 1968). End users of PSHA include those charged with land-use planning, building-code revisions, disaster preparation and recovery, emergency response, and the design of lifelines and critical facilities, as well as organizations that promote public education for risk mitigation (National Research Council, 2011).

One of the main modeling components of PSHA is an earthquake rupture forecast (ERF), which quantifies the probability of all damaging earthquakes in a region for a given timespan, above some magnitude threshold, and at some level of discretization deemed adequate for hazard assessment. ERFs are also useful for choosing earthquake-planning scenarios (e.g., Wald *et al.*, 2005) and for quantifying what events might be unfolding in an earthquake early warning system (e.g., Cua *et al.*, 2009).

Two different entities have traditionally developed official ERFs for California. One is the National Seismic Hazard Mapping Program (NSHMP) of the U.S. Geological Survey (USGS), which has developed statewide, time-independent (long-term) models for use in the national seismic-hazard

Table 1
List of Acronyms

Acronym	Definition
10in50	10%-in-50-year exceedance probability
1in100	1%-in-100-year exceedance probability
2in50	2%-in-50-year exceedance probability
ABM	Averaged block model
BSSC	Building Seismic Safety Council
CEA	California Earthquake Authority
CEPEC	California Earthquake Prediction Evaluation Council
CGS	California Geological Survey
COV	Coefficient of variation
<i>EllsworthB</i>	Ellsworth B (WGCEP, 2003) magnitude–area relationship (equation 2)
ERF	Earthquake rupture forecast
ETAS	Epidemic-type aftershock sequence
ExCom	Executive Committee
FM	Fault model
GPS	Global Positioning System
GR	Gutenberg–Richter
<i>HanksBakun08</i>	Hanks and Bakun (2008) magnitude–area relationship (equation 1)
InSAR	Interferometric Synthetic Aperture Radar
LA	Los Angeles
MFD	Magnitude–frequency distribution
MOC	Management Oversight Committee
MRI	Mean recurrence interval
MRT	Multidisciplinary Research Team
NEHRP	National Earthquake Hazards Reduction Program
NEPEC	National Earthquake Prediction Evaluation Council
NSHMP	National Seismic Hazard Mapping Program
<i>Off-Fault Spatial Seis PDF (or Spatial PDF)</i>	Spatial distribution of off-fault gridded seismicity set by choosing one of the spatial probability density maps
OpenSHA	Open-source, Java-based platform for conducting seismic-hazard analysis
PGA	Peak ground acceleration
PSHA	Probabilistic seismic-hazard analysis
RELM	Regional Earthquake Likelihood Models
SA	Spectral acceleration
SAF	San Andreas fault
SCEC	Southern California Earthquake Center
SF	San Francisco
Shaw09mod	Modified version of Shaw (2009) magnitude–area relationship, as justified in Appendix E (Shaw, 2013b) (equation 3)
<i>Spatial PDF (or Off-Fault Spatial Seis PDF)</i>	Spatial distribution of off-fault gridded seismicity set by choosing one of the spatial probability density maps
SRP	Scientific Review Panel
USGS	United States Geological Survey
UCERF	Uniform California Earthquake Rupture Forecast
WGCEP	Working Group on California Earthquake Probabilities

maps (e.g., Algermissen *et al.*, 1982; Frankel *et al.*, 1996, 2002; Petersen *et al.*, 2008). The other official ERFs were from the Working Groups on California Earthquake Probabilities

(e.g., WGCEP, 1988, 1990, 1995, and 2003), which developed time-dependent models based on the Reid (1911) elastic rebound theory (in which probabilities drop on a fault after experiencing a rupture and build back up with time as tectonic stresses reaccumulate). These WGCEP models, however, only covered a subset of California; see Field (2007) for a review.

The 1994 Northridge earthquake led to an insurance-availability crisis, which prompted the California legislature to create the California Earthquake Authority (CEA), a publicly managed provider of residential earthquake insurance that is funded primarily by participating private insurance companies. CEA currently holds about two-thirds of all such policies in California, making it one of the largest residential earthquake insurance providers in the world. The enabling legislation for CEA states that insurance rates shall be based on the “best available science” and that any statewide variability in insurance rates must reflect actual risk differentials. These requirements created the demand for a time-dependent forecast based on uniform methodologies across the state, which was lacking in the official models developed previously. Consequently, a new WGCEP effort was commissioned in September 2004 and charged with developing a Uniform California Earthquake Rupture Forecast (UCERF). The project was collaborative between the USGS, the California Geological Survey (CGS), and the Southern California Earthquake Center (SCEC), with significant funding from CEA. This working group came to be known as WGCEP, 2007.

The first model developed by WGCEP, 2007, was a prototype, UCERF1 (Petersen, Cao, *et al.*, 2007), assembled from available components without conforming to a consistent time-dependent methodology statewide. The final consensus model, UCERF2, was released to the public in April 2008 as a USGS Open-File Report, including 16 appendixes (WGCEP, 2007), and the main report was also published in the *Bulletin of the Seismological Society of America* (Field *et al.*, 2009). UCERF2 was the first statewide, time-dependent model that used consistent methodologies, data-handling standards, and uncertainty treatment in all regions. The entire model was implemented in OpenSHA (Field *et al.*, 2003; see Data and Resources), an open-source, object-oriented computational framework for seismic hazard, which enabled unprecedented flexibility with respect to PSHA calculations for any or all of the alternative time-dependent components. The development was also fully coordinated with the NSHMP, as the time-independent version of UCERF2 was adopted for use in the 2008 USGS national seismic-hazard maps (Petersen *et al.*, 2008).

Although WGCEP, 2007, was successful in terms of stated goals, a number of issues were identified in the “Model Limitations and Opportunities for Future Improvements” section of the report. The most salient of these were (1) to relax segmentation assumptions and include multifault ruptures and (2) to incorporate spatiotemporal clustering for the time-dependent forecasting of aftershocks and other triggered earthquake sequences. Both of these issues were subsequently, and

dramatically, exemplified following the UCERF2 publication, by events such as the 2011 M 9 Tohoku earthquake with respect to segmentation (e.g., Kagan and Jackson, 2013), the 2011 M 6.3 Christchurch earthquake in terms of spatiotemporal clustering (e.g., Kaiser *et al.*, 2012), and both the 2010 M 7.2 El Mayor–Cucapah and 2012 M 8.6 Sumatra earthquakes in regard to multifault ruptures (e.g., Hauksson *et al.*, 2011; Meng *et al.*, 2012). There is also now a substantial body of literature on the viability of multifault ruptures (e.g., Segall and Pollard, 1980; Knuepfer, 1989; Harris *et al.*, 1991; Harris and Day, 1993; Lettis *et al.*, 2002; Duan and Oglesby, 2006; Wesnousky, 2006; Shaw and Dieterich, 2007; Black and Jackson, 2008; and Finzi and Langer, 2012).

A persistent problem in WGCEP and NSHMP studies of California seismicity has been the overprediction, or bulge, in the modeled event rates between M 6.5 and 7.0 (e.g., the “earthquake deficit” described in WGCEP, 1995). The UCERF2 rates also showed a bulge in this magnitude range, requiring *ad hoc* adjustments to lower them to within the 95% confidence bounds of observed rates. WGCEP, 2007, speculated that the relaxation of strict segmentation would provide a better solution to the bulge problem, and they noted that the multifault ruptures observed in the 1992 Landers, California, and 2002 Denali, Alaska, earthquakes supported this hypothesis.

In addition to the 2011 M 6.3 Christchurch earthquake, which demonstrated that aftershocks could be more damaging than their mainshock (Kaiser *et al.*, 2012), the 2009 L’Aquila, Italy, earthquake also exemplified the potentially dire effects of earthquake triggering (van Stiphout *et al.*, 2010). In fact, an international commission convened in the aftermath of the latter earthquake (Jordan *et al.*, 2011) concluded that we need to move more aggressively toward operational earthquake forecasting (OEF), which, by definition, would include both authoritative, real-time forecasts and official protocols for communicating implications to the public (Jordan *et al.*, 2011). Furthermore, OEF is now listed as one of the strategic-action priorities of the USGS, with a goal of providing “effective situational awareness” during hazardous events and core responsibilities that include issuing warnings and providing timely information to emergency managers, the media, and the public (Holmes *et al.*, 2013, pp. 32–33).

Recognizing the limitations of UCERF2 and the rapid pace of earthquake forecasting research, the USGS, CGS, and SCEC reconstituted WGCEP in 2010 and, with support from CEA, charged it with developing a new model, UCERF3. This report presents the resultant time-independent component of UCERF3, in which we relaxed segmentation and included multifault ruptures via a generalized inversion approach. A number of other issues have been addressed as well, and virtually all datasets have been revised and updated. Four different UCERF3 models were developed, evaluated, and formally reviewed during the course of this project: versions 3.0, 3.1, 3.2, and 3.3. The latter is the final time-independent model presented here as UCERF3. Although a

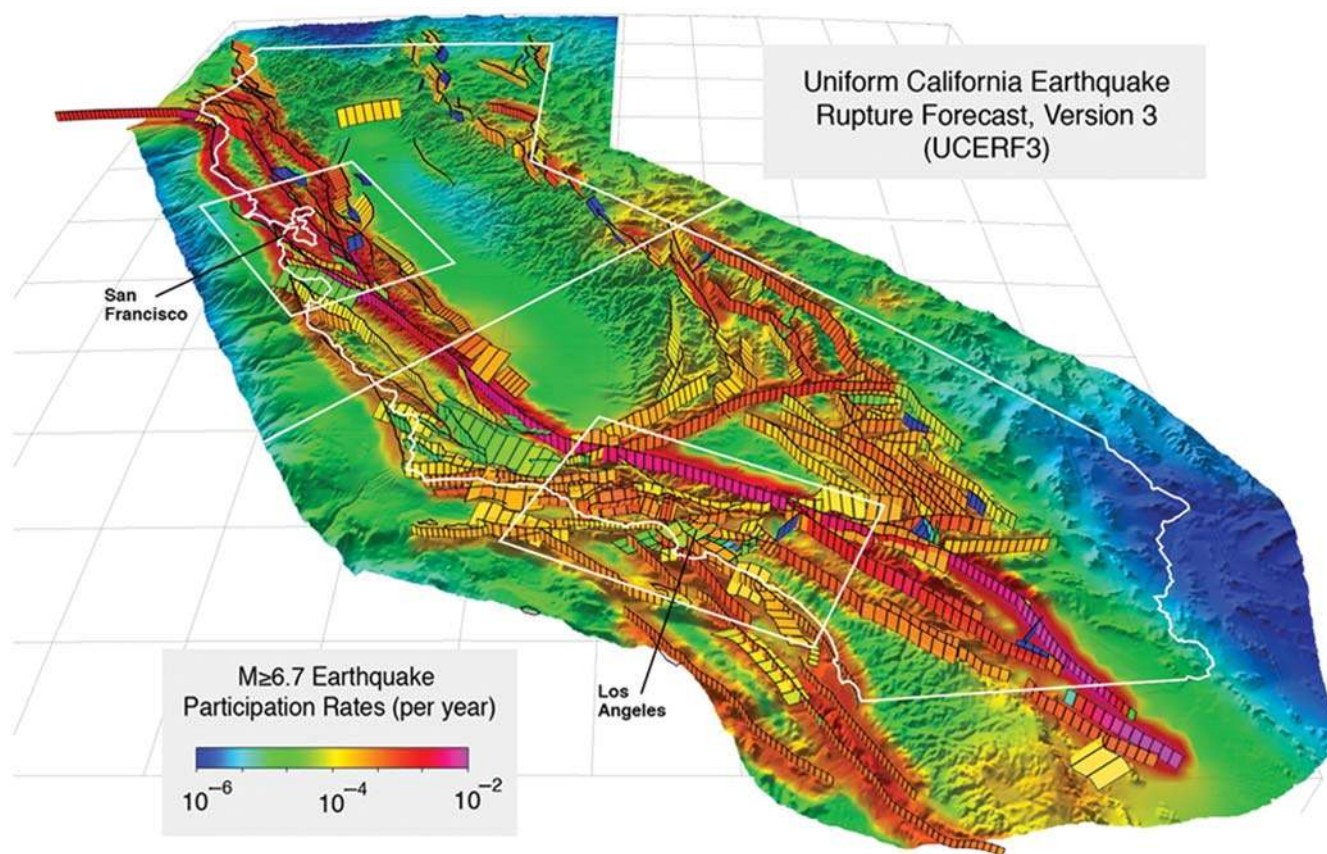


Figure 1. 3D perspective view of California, showing the 2606 fault sections (black rectangles) of UCERF *Fault Model 3.1* (FM 3.1). Colors indicate the long-term rate at which each area participates in $M \geq 6.7$ earthquakes, averaged over all 720 UCERF3 logic-tree branches for FM 3.1 and including aftershocks. The entire colored area represents the UCERF model region, which comprises California and a buffer zone. The white boxes define the San Francisco Bay area and Los Angeles regions used in various calculations, and the white line crossing the state is our definition of northern versus southern California. The Cascadia megathrust is not shown on this map; it and the Mendocino transform fault (which is shown) extend beyond the UCERF model region.

detailed version history is not provided in this report, the more important changes are discussed in the context of lessons learned.

The spatial domain of UCERF3 is the same as that used for UCERF2, shown by the polygon surrounding California in Figure 1. This is sometimes referred to as the “RELM” region, as it was first adopted for the purpose of developing and testing alternative forecasts in the Regional Earthquake Likelihood Models (RELM) project (Field, 2007; Schorlemmer *et al.*, 2007). RELM has since expanded into the Collaboratory for the Study of Earthquake Predictability (Zecher *et al.*, 2010), and the continued use of this evaluation region will greatly facilitate formal, independent testing of UCERF3.

As with its predecessor, UCERF3 development has been coordinated with the NSHMP, and the time-independent component presented here has been formally adopted in the 2014 revisions to national seismic-hazard maps. The model for the Cascadia subduction zone, which extends partway into northern California from Oregon and Washington, was developed by a separate NSHMP working group. Coordination with UCERF3 was achieved via joint participation in workshops (Table 2). Because the Cascadia model is largely de-

coupled from UCERF3 and presented elsewhere (Frankel and Petersen, 2013), we do not discuss it here.

The complete documentation of the UCERF3 time-independent model, including appendixes and supplementary materials, is available as a USGS Open-File Report (Field *et al.*, 2013). A number of key products were developed for UCERF3, most of which are represented in the various appendixes listed in Table 3. Each appendix was reviewed by the UCERF3 Scientific Review Panel (SRP), defined in the *Participants, Review, and Consensus Building* section, and often by additional experts selected by the SRP chair. Although some of these appendixes also have been published as peer-reviewed journal papers, we refer to these appendixes here by the corresponding letter given in Table 3, as well as the full reference to the report. All are noteworthy achievements in and of themselves, and many will be of broader interest. For example, the UCERF3 deformation models (Appendix C, Parsons *et al.*, 2013) can be used in developing physics-based earthquake simulators (e.g., Tullis *et al.*, 2012).

The time-dependent components of UCERF3 will be the topic of future reports. For instance, we attempt to include spa-

Table 2
WGCEP14 Consensus-Building Workshops and Meetings

	Date	Activity Description*
2009	Dec 1–2	UCERF3 Kick-Off and Planning Meeting
2010	Feb 17–18	WGCEP All-Hands Meeting
	Apr 1–2	Workshop on Incorporating Geodetic Surface Deformation Data in UCERF3
	Jun 30	UCERF3 Methodology Assessment—Issues and Research Plan (Report 1) Submitted
	Aug 2	Fault-to-Fault Jumps Task Meeting
	Sep 12–15	SCEC Annual Meeting
	Nov 3–4	CEPEC/NEPEC Meeting
	Nov 10–11	Scientific Review Panel Meeting
	Nov 18–19	Cascadia Subduction Zone Workshop
	Dec 31	UCERF3 Methodology Assessment—Proposed Solutions to Issues (Report 2) Submitted
2011	Jan 12	WGCEP All-Hands Meeting
	Mar 2–3	Distribution of Slip in Large Earthquakes Meeting
	Apr 6	Statewide Fault Model and Paleoseismic Data Workshop (in northern California)
	Apr 8	Statewide Fault Model and Paleoseismic Data Workshop (in southern California)
	May 31	Proposed UCERF3 Plan (Report 3) Submitted
	Jun 4–5	Workshop on UCERF3 Deformation Models
	Jun 8	Workshop on Time-Dependent Models
	Jun 9	Workshop on the Use of Physics-Based Simulators
	Jun 10	Workshop on Instrumental and Historical Seismicity
	Jun 11	Workshop on Distribution of Slip in Large Earthquakes
	Jun 13–14	Scientific Review Panel Meeting
	Jun 30	SRP Review of Proposed UCERF3 Plan (Report 4) Submitted
	Sep 11–14	SCEC Annual Meeting
	Sep 30	Final UCERF3 Plan (Report 5) Submitted
	Oct 24	UCERF3 Plan Overview (Emphasizing the Grand Inversion for Users)
	Oct 25	Joint UCERF3 and NGA-W2 Workshop on Common Issues
	Dec 15	Cascadia Subduction Zone Workshop
2012	Jan 5–6	WGCEP All-Hands Meeting
	Jan 26	UCERF3 Deformation Model Meeting
	Mar 21–22	Cascadia Subduction Zone Workshop
	Mar 31	Preliminary UCERF3 Model (Report 6) Submitted
	Apr 30	Review of Preliminary UCERF3 Model (Report 7) Submitted
	May 8–9	Scientific Review Panel Meeting
	Jul 9	UCERF3 Model Framework (Report 8) Submitted
	Oct 17–18	California Workshop of the National Seismic Hazard Mapping Project (NSHMP)
2013	Jan 24	UCERF3 Fault-by-Fault Evaluation Meeting 1
	Jan 25	UCERF3 Fault-by-Fault Evaluation Meeting 2
	Feb 13–14	UCERF3 Fault-by-Fault Evaluation Meeting 3
	Feb 21	Workshop on Use of UCERF3 in the USGS National Seismic Hazard Map

*Abbreviations are listed in Table 1.

tiotemporal earthquake clustering by merging a point-process epidemic-type aftershock sequence model (ETAS; Ogata, 1988) into our finite-fault-based framework. Our ultimate aim is to deploy UCERF3 as part of an operational earthquake forecast, although doing so will require additional work with respect to real-time network interoperability. Other goals for the time-dependent model include addressing self-consistency issues with respect to elastic-rebound probability calculations in unsegmented models (Field *et al.*, 2009) and further investigating the implications of apparent seismicity rate changes with respect to the likelihood of large damaging earthquakes (the empirical model of WGCEP, 2003, and in UCERF2; e.g., Reasenberg *et al.*, 2003).

The unique approach taken in developing UCERF3 has necessitated an extensive set of PSHA calculations, both for logic-tree sensitivity tests and for determining adequacy with respect to averaging over stochastic elements of the long-

term model. This unanticipated requirement extended the duration of the project, but the fact that we include hazard calculations herein is a notable first among WGCEPs. Although the UCERF3 platform now lends itself to continual updates and improvements, the features and options adopted here were dictated by deadlines of the Building Seismic Safety Council (BSSC).

Model Framework

The UCERF3 framework, like that of UCERF2, has been constructed from the four main model components shown in Figure 2. The fault model gives the physical geometry of the larger, known, and more active faults; the deformation model gives slip-rate and creep estimates for each fault section, as well as deformation rates off the modeled faults (if available); the earthquake rate model gives the long-term rate of all earth-

Table 3
Appendixes to the Full Documentation of the UCERF3 Time-Independent Model (Field *et al.*, 2013)*

Appendix	Title	Authors
A	Updates to the California Reference Fault Parameter Database: UCERF3 Fault Models 3.1 and 3.2	Dawson, T. E.
B	Geologic Slip-Rate Data and Geologic Deformation Model	Dawson, T. E., and R. J. Weldon, II
C	Deformation Models for UCERF3.3	Parsons, T., K. M. Johnson, P. Bird, J. M. Bormann, T. E. Dawson, E. H. Field, W. C. Hammond, T. A. Herring, R. McCaffrey, Z.-K. Shen, W. R. Thatcher, R. J. Weldon, II, and Y. Zeng
D	Compilation of Creep Rate Data for California Faults and Calculation of Moment Reduction Due to Creep	Weldon, II, R. J., D. A. Schmidt, L. J. Austin, E. M. Weldon, and T. E. Dawson
E	Evaluation of Magnitude-Scaling Relationships and Depth of Rupture	Shaw, B. E.
F	Distribution of Slip in Ruptures	Biasi, G. P., R. J. Weldon, II, and T. E. Dawson
G	Paleoseismic Sites Recurrence Database	Weldon, II, R. J., T. E. Dawson, G. P. Biasi, C. Madden, and A. R. Streig
H	Maximum Likelihood Recurrence Intervals for California Paleoseismic Sites	Biasi, G. P.
I	Probability of Detection of Ground Rupture at Paleoseismic Sites	Weldon, II, R. J., and G. P. Biasi
J	Fault-to-Fault Rupture Probabilities	Biasi, G. P., T. Parsons, R. J. Weldon, II, and T. E. Dawson
K	The UCERF3 Earthquake Catalog	Felzer, K. R.
L	Estimate of the Seismicity Rate and Magnitude–Frequency Distribution in California from 1850 to 2011	Felzer, K. R.
M	Adaptive Smoothed Seismicity Model	Felzer, K. R.
N†	Grand Inversion Implementation and Testing	Page, M. T., E. H. Field, K. R. Milner, and P. M. Powers
O	Gridded Seismicity Sources	Powers, P. M., and E. H. Field
P	Models of Earthquake Recurrence and Down-Dip Edge of Rupture for the Cascadia Subduction Zone	Frankel, A. D., and M. D. Petersen
Q	The Empirical Model	Felzer, K. R.
R	Compilation of Slip in the Last Event Data and Analysis of Last Event, Repeated Slip, and Average Displacement for Recent and Prehistoric Ruptures	Madden, C., D. E. Haddad, J. B. Salisbury, O. Zielke, J. R. Arrowsmith, R. J. Weldon, II, and J. Colunga
S	Constraining ETAS Parameters from the UCERF3 Catalog and Validating the ETAS Model for $M \geq 6.5$ Earthquakes	Hardebeck, J. L.
T	Defining the Inversion Rupture Set Via Plausibility Filters	Milner, K. R., M. T. Page, E. H. Field, T. Parsons, G. P. Biasi, and B. E. Shaw

*All appendixes can be cited as independent elements of *USGS Open-File Report 2013-1165* on UCERF3.

†Appendix N is also published as Page *et al.*, 2014.

quakes throughout the region (at some level of discretization); and the earthquake probability model gives the likelihood that each event will occur during a specified time span, perhaps conditioned on additional information such as date of the last event. The first three of these model components are discussed in the [Fault Models](#), [Deformation Models](#), and [Earthquake Rate Models](#) and the “Grand Inversion” sections. These are sufficient for time-independent PSHA, as the assumed Poisson probability model depends only on long-term rates. Truly time-dependent probability models, based on renewal and clustering processes, will be the topic of future publications.

We acknowledge there are situations in which the distinction in Figure 2 can break down, such as when differen-

tiating a multifault rupture (in the earthquake rate model) from the case in which one fault very quickly triggers another (in the earthquake probability model). The distinction nevertheless remains both a modeling convenience and a practical necessity to the extent that building codes remain based on long-term rates of events.

This modularization also aids in the implementation of alternative models (e.g., the logic-tree branches discussed in the [Model Uncertainties](#) section) and in the replacement of model elements with new components. Building on OpenSHA, [WGCEP, 2007](#), put considerable effort into developing an open-source, object-oriented, and extensible UCERF cyberinfrastructure, including the use of distributed

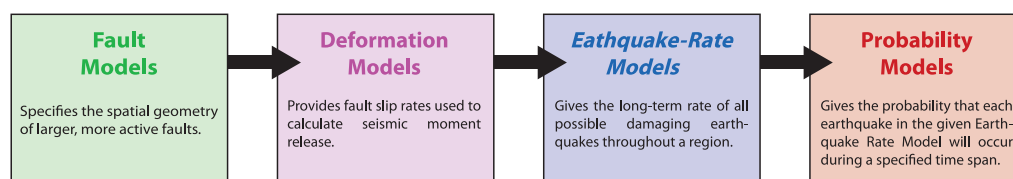


Figure 2. The four main model components of the UCERF3 framework.

data resources and flexible analysis tools. UCERF3 represents a dividend on these investments, which we have augmented with new computational capabilities, including the use of supercomputers to solve for earthquake rates and to generate large numbers of hazard curves.

Model Uncertainties

As a result of a lack of consensus on how to forecast earthquakes, it is important that our model adequately portray epistemic uncertainties, which represent our incomplete understanding of how the earthquake system works, as well as the aleatory uncertainties, which represent the inherent randomness assumed in any given model of the system (Senior Seismic Hazard Analysis Committee, 1997). The history of WGCEPs can be viewed as a progression of including more and more epistemic uncertainties. For example, WGCEP, 1988, did not consider a possible recurrence of the two largest historical events (the great 1857 and 1906 earthquakes), whereas WGCEP, 2003, represented a quantum leap in having 10,000 different models for the Bay Area alone.

As in UCERF2, we represent epistemic uncertainties using a logic tree structured according to the four main model components. Our final branch options and associated weights for the UCERF3 time-independent model are shown in Figure 3. (UCERF3 logic-tree branches from Fig. 3 are shown in *italic* throughout this article.) Note that some branch options are given zero weight but are shown nonetheless in case practitioners want to reconsider their applicability in special (e.g., site-specific) studies. The set of non-zero-weighted branches gives rise to 1440 different UCERF3 models.

UCERF3 represents an important step in the WGCEP quest for a more complete representation of epistemic uncertainty. For example, rather than assuming or prescribing earthquake-generating attributes of the various seismic sources, as in previous NSHMP and WGCEP models, we take a more derivative approach to system-level behavior by solving for a much wider range of models that are consistent with the data. Of course, UCERF3 is still an approximation of the actual system (e.g., imposing strict separation between on-fault and off-fault earthquakes). Because “all models are wrong, but some are useful” (Box, 1979), the relevant question for practitioners is whether UCERF3 is a better representation of future earthquake activity than UCERF2 for the purpose of managing seismic risk.

Participants, Review, and Consensus Building

The organizational structure used in this study is similar to WGCEP, 2007, comprising an Executive Committee (ExCom), a Management Oversight Committee (MOC), an SRP, and a large group of contributing experts. The ExCom was responsible for convening experts, reviewing options, and making decisions about model components. The MOC allocated resources and approved project plans, budgets, and schedules; it also oversaw the model review and delivery processes. The SRP is an independent, participatory body of

experts who reviewed the project plans, research results, and model elements. In particular, the SRP provided WGCEP with guidance regarding model viability and the range of models needed to adequately represent epistemic uncertainties. Other WGCEP contributors include research scientists, resource experts, model advocates, and information technology professionals. Members of these groups are listed in the Acknowledgments. We also note that CEA’s multidisciplinary research team (MRT) participated in UCERF3 reviews but were not directly involved in the model development or any decisions about branch options.

The discussion of model options and consensus building was achieved through a series of community workshops (Table 3), which included participants from the broader community. Some workshops focused on the scientific ingredients going into UCERF3, while others were aimed at informing user communities and getting their feedback. Numerous smaller working group meetings also occurred but are not listed in Table 3.

Although all participants, including the SRP, influenced decisions with respect to logic-tree branches and their weights, the ExCom had responsibility for the final decisions. In the case of deformation models, for which the ExCom felt that special expertise was needed, an *ad hoc* evaluation committee was convened to advise on branch weights (discussed in the Logic-Tree Branch Weights section). The entire UCERF3 process was monitored by representatives of the National Earthquake Prediction Evaluation Council (NEPEC), which formally advised the USGS Director, and the California Earthquake Prediction Evaluation Council (CEPEC), which formally advised the California Office of Emergency Services.

Fault Models

The UCERFs are primarily fault-based earthquake rupture forecasts, in that most large earthquakes (~80%) occur on the possible rupture surfaces defined by a fault model (Fig. 2). The fault database developed for UCERF2 has been updated with both revisions and additions, with special consideration being given to fault endpoints for the purpose of defining multifault rupture possibilities. Full details are given in Appendix A (Dawson, 2013), and a summary of the more important changes is presented here.

Definition

A fault model gives the spatial geometry of the larger, active faults throughout the region, with alternative models representing epistemic uncertainties in the fault system geometry. By definition, a fault model is composed of a list of fault sections, where each fault section is represented by the following:

- a fault section name (e.g., “San Andreas [Parkfield]”),
- a fault trace (list of latitudes, longitudes, and depths for the upper fault edge),
- upper and lower seismogenic depth estimates,

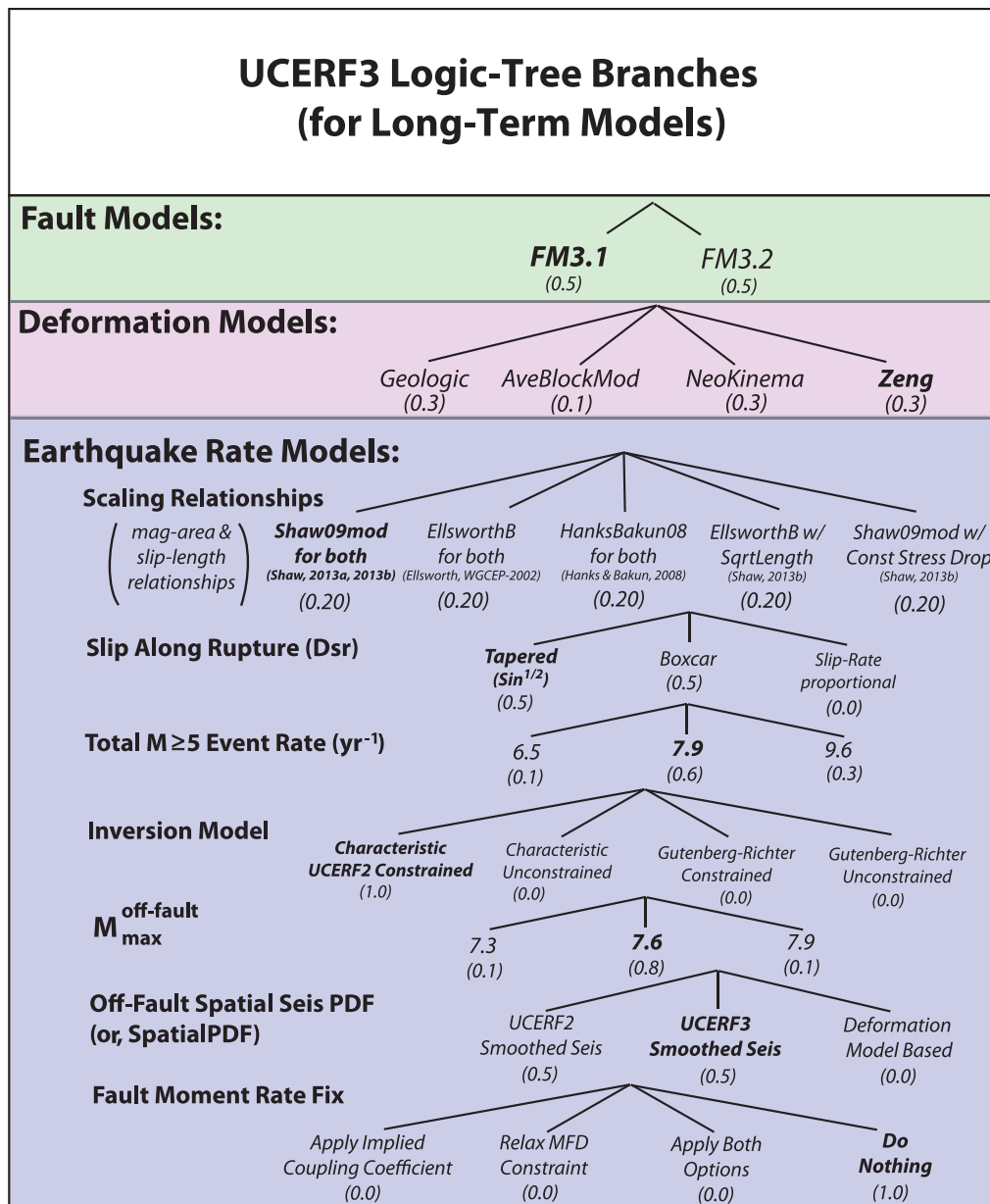


Figure 3. UCERF3 long-term model logic-tree branches with weights given in parentheses. The branches are organized by the basic model components in Figure 2: fault models (green), deformation models (purple), and earthquake rate models (blue). The branches and weighting decisions, as well as reference branch values for sensitivity tests (bold typeface), are described in the sections for each component. UCERF3 has a total of 1440 nonzero branches.

- an average dip estimate,
- an average rake estimate (although this can be modified by a deformation model), and
- a fault zone polygon (an areal representation of a fault zone).

Because distinct fault sections are defined only to the extent that one or more of these attributes vary along strike, some sections can be quite long (e.g., the northern San Andreas fault has only four sections). The complete master list of fault sections for California is given in the fault section database (Appendix A; Dawson, 2013). Some of these sections are mutually exclusive (e.g., representing alternative representa-

tions). The list of fault sections in each fault model is therefore considered to be a separate, complete, viable representation of the large, known, and active faults throughout the region.

Fault Zone Polygons

Previous models, including UCERF2, have been somewhat ambiguous with respect to what each fault section actually represents. For example, it is not clear whether the 2010 El Mayor–Cucapah earthquake (Hauksson *et al.*, 2011) was an event on the UCERF2 Laguna Salada fault source or whether it was part of the gridded/background seismicity

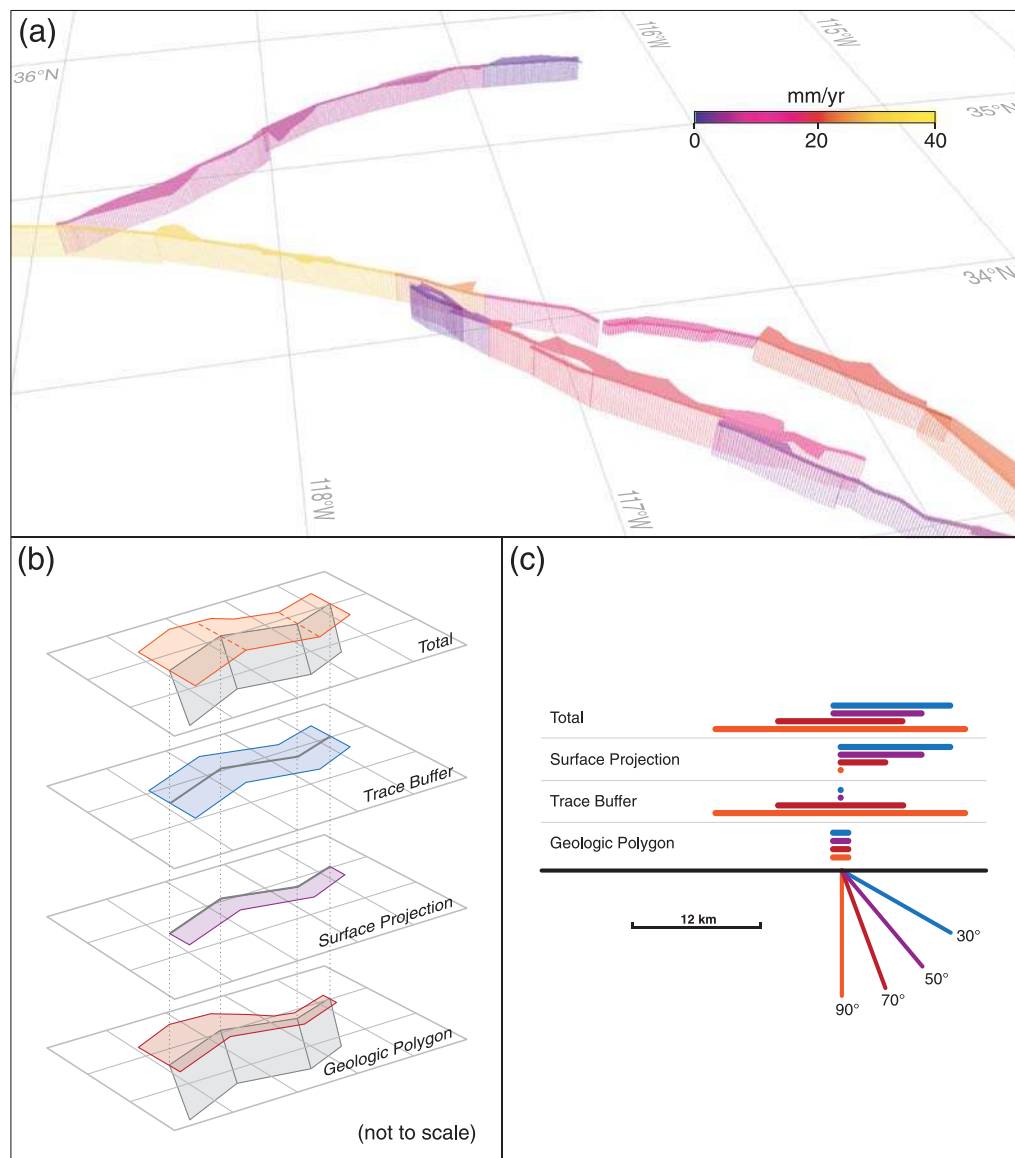


Figure 4. The definition and creation of fault zone polygons. (a) Perspective view of the Garlock, southern San Andreas, and San Jacinto fault systems, color coded by slip rate (other faults in this region are not shown). Down-dip projections of the faults are stippled, and the geologically defined surface polygons are solid. The geologic polygons typically extend to 1 km on either side of the fault traces but in many places are much broader to accommodate additional mapped surface features. (b) Schematic diagram of the union of geologic, surface projection, and trace buffer polygons to form the final fault zone polygon used in UCERF3. The exemplified fault dips at $\sim 70^\circ$, so the buffer polygon extends to 6 km on either side of the fault trace. The dashed orange lines in the complete polygon mark the subdivisions used to define polygons for the individual fault sections. (c) A strike perpendicular cross section of a fault, showing how dip variations influence the widths of the trace buffer, the surface projection, and the complete fault zone polygon used in UCERF3.

defined in that model. We therefore introduced fault zone polygons to be more specific in UCERF3, with each fault section now representing a proxy for all events that nucleate inside its polygon. Complete definitions are given in Appendix O (Powers and Field, 2013), which are only summarized here.

Ideally, a fault zone polygon would represent all of the following:

- whether the fault section represents a simple surface or a broader, braided system of faults;
- the area over which the deformation-model slip rate applies;

- the faults to which observed microseismicity is attributed;
- the area over which elastic-rebound-based probability reductions are applied after an earthquake; and
- whether a future large earthquake is identified as a rupture of a UCERF3 modeled fault.

As exemplified in Figure 4a, geologically based polygons were initially assigned to each fault section (Appendix A; Dawson, 2013), thereby satisfying the first criteria listed above. However, for some faults, such as the San Andreas, this zone is as narrow as 1 km on each side of the fault, which

is too thin for the other intended uses listed here. This reflects the fact that there is no single polygon definition that will perfectly satisfy all intended uses.

A fault zone width was effectively defined in UCERF2 based on standards established previously by the NSHMP in distinguishing fault-based sources from gridded, off-fault seismicity. Specifically, the maximum magnitudes for gridded seismicity were previously reduced in the vicinity of fault-based sources to avoid overlap with the minimum magnitude of fault sources (e.g., Petersen *et al.*, 2008). Although this led to a checkerboard pattern for the zones around faults (according to the grid cells assigned to each fault), the average width of their zones was about 12 km on either side of vertically dipping faults.

WGCEP has therefore adopted a default width of 12 km on both sides of vertically dipping faults (the “trace buffer” described in Fig. 4), with this tapering to the surface projection for faults dipping less than 50°. Final fault zone polygons are then the combination (or union) of three independently defined polygons (Fig. 4b): the geologically defined polygon for the fault, the surface projection of the fault if dipping, and the trace buffer. The width of the buffer polygon on either side of a fault trace scales linearly from 0 km at 50° dip to 12 km at 90° dip (Fig. 4c). This provides vertical faults with a broad zone of influence that scales down as dip decreases and the area of the surface projection polygon increases. Figure 4b demonstrates how the three polygons are combined. This fault zone definition is both consistent with past NSHMP practice and avoids the checkerboard pattern. It is still somewhat simplified and arbitrary, however, so potential hazard implications of this choice need to be considered carefully in any given application, as we will illustrate in the [Characteristic Branches](#) section.

Logic-Tree Branches

UCERF3 comprises two alternative fault models: *FM 3.1* and *FM 3.2*, which are analogous to the fault model alternatives *FM 2.1* and *FM 2.2* used in UCERF2. These two new models, shown in Figure 5, represent alternative representations of several fault groups. Reducing all possible combinations to just two models introduces artificial correlation between the alternatives for different faults; however, the groupings are judicious choices in terms of minimizing the number of logic-tree branches (every additional fault model requires 720 new logic-tree branches), and the PSHA calculations discussed in the [Results](#) section indicate adequacy for at least the most common hazard metrics.

Development Process

Fault models *FM 3.1* and *3.2* were developed in coordination with the Statewide Community Fault Model project, which builds on SCEC’s community fault model development (Plesch *et al.*, 2007). Two workshops were held to solicit feedback from the broader community in April of 2011 (Table 3). Relative to UCERF2, the primarily modifications are (1) 153 new fault sections were added, mostly in northern

California, and about 95 fault sections were revised (the numbers are not exact due to some being a bit of both); (2) fault endpoints were re-examined by reviewing more detailed geologic maps, to enable better quantification of multifault rupture probabilities; and (3) connector fault sections were added between larger faults where deemed appropriate, to enable multifault ruptures or, where needed, to define block boundaries for the deformation models. Figure 5 shows the fault sections that were added, modified, or left unchanged from UCERF2. Further details on how these fault models were constructed are given in Appendix A (Dawson, 2013).

Deformation Models

The rate of large earthquakes on the explicitly modeled faults depends on assigned slip rates, which are provided by the deformation models described here. This section also describes how these slip rates and rupture areas are modified by creep processes. Fault slip rates can be derived from measured and dated geologic offsets and perhaps interpolated or extrapolated along faults. Slip rates can also be estimated by modeling geodetic measurements such as Global Positioning System (GPS) observations (e.g., Fig. 6). Because it is impossible to identify and model all faults, another contribution to hazard is “off-fault” deformation (in quotes here because this deformation occurs at least partially on unmodeled faults, which can be inferred from observed seismicity and/or GPS observations).

Only about 30% of UCERF2 faults had measured slip rate estimates, and most of these had an estimate at only a single location. UCERF2 deformation models were therefore based on expert-opinion evaluation of geologic and geodetic data. In addition to on-fault slip rates, off-fault deformation was represented by a set of geographic polygons, referred to as “type C zones,” each of which was assigned an effective slip rate (Fig. 5a). As an *a posteriori* check, UCERF2 deformation models were summed across various transects to confirm that total plate tectonic rates were well matched.

For UCERF3, we have developed four different deformation models. One is a geologically “pure” model (uninfluenced by GPS observations), whereas the other three are kinematically consistent models that directly include both geologic and geodetic constraints. By using these models, we minimize reliance on expert judgment to broker discrepancies between geodetic and geologic data, as was done in UCERF2. Importantly, this approach has provided data-driven slip rate estimates for faults with no prior assigned rates (which were excluded from UCERF2) and has filled in slip rates along faults with sparse observations. The latter three models also provide off-fault strain rate maps, allowing us to abandon the UCERF2 type C zones.

Geologic Slip Rate Constraints

Because UCERF2 expert-opinion slip rates were influenced by both geologic and geodetic data, an effort was made

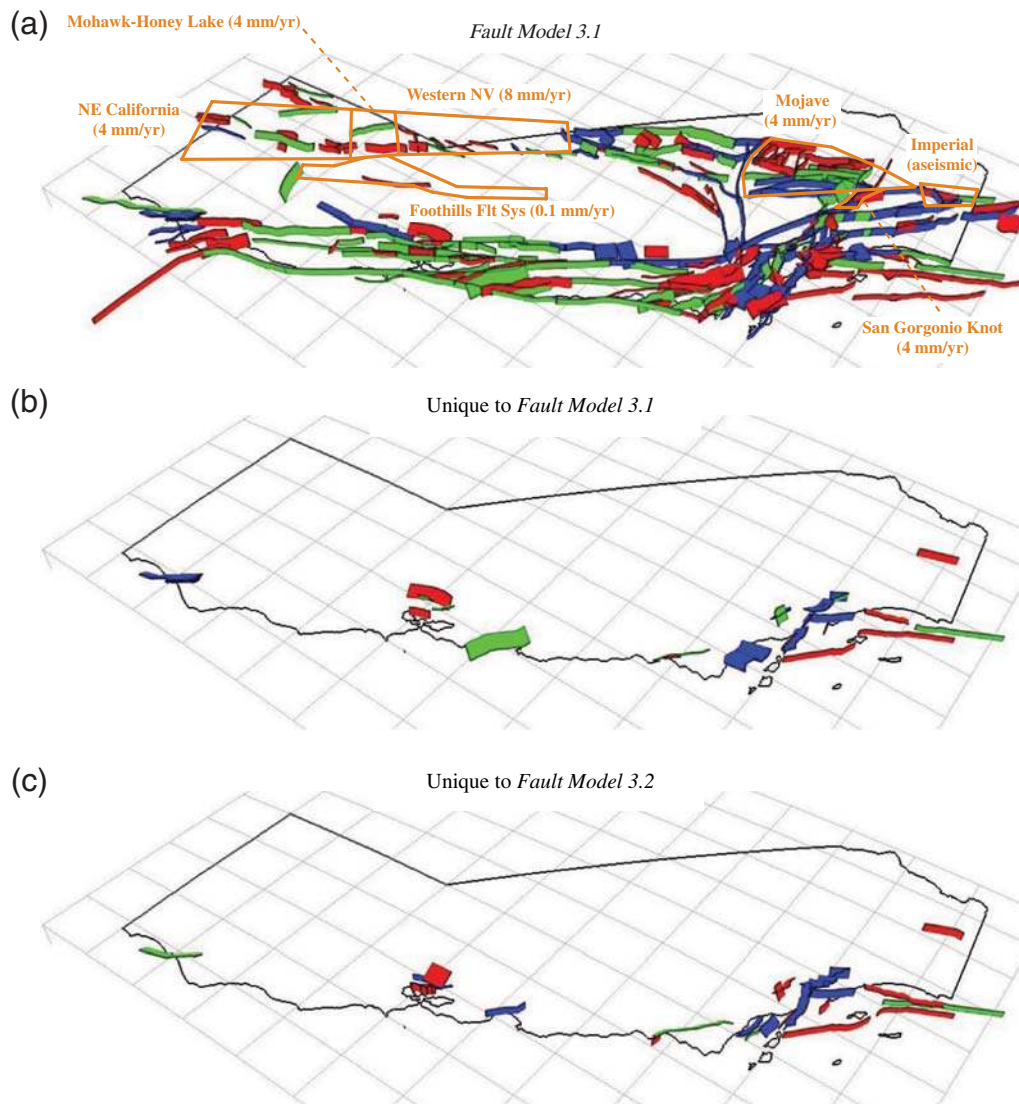


Figure 5. Perspective map of California showing (a) UCERF3 *Fault Model 3.1* and fault sections unique to (b) *FM 3.1* and (c) *FM 3.2*. Fault sections are colored to identify those that were added (red), modified (green), and unchanged (blue) since UCERF2. Some of the modifications are relatively trivial (e.g., name change only); see Appendix A (Dawson, 2013) for precise details. Type C zones applied in UCERF2 (orange polygons; see text for explanation) are labeled with their modeled deformation rates. The Cascadia subduction zone is not shown here but is given in Appendix P (Frankel and Petersen, 2013).

in UCERF3 to extract and compile the geologic-only constraints at points on faults where such data exist (Appendix B, Dawson and Weldon, 2013). In addition to geologic slip rates, Appendix B also includes the supporting data, such as information about the site location, offset features, dating constraints, number of events, reported uncertainties, comments, and separate qualitative ratings of the offset features, dating constraints, and overall slip rate. In the majority of cases, these data were compiled from the original sources, although extensive use was also made of the written summaries included in the USGS Quaternary Fault and Fold Database (Machette *et al.*, 2004).

Given the number of Quaternary active faults in California, the dataset of geologic slip rates is somewhat sparse. The compilation includes ~230 reported slip rates,

of which about 150 reported rates are ranked as moderately to well constrained. Of the ~350 fault sections in the UCERF3 fault model, only about 150 fault sections are directly constrained by slip rate data (Fig. 7b). This emphasizes the fact that slip rates in previous models, as in the pure geologic model here, are often extrapolated over large along-fault distances, and that values for most fault sections are not directly constrained by geologic data.

Geologic Deformation Model

One of the new UCERF3 deformation models is a purely geologic model that includes no constraints from geodesy or plate motion models (Appendix B, Dawson and Weldon, 2013). As with the other deformation models, the output

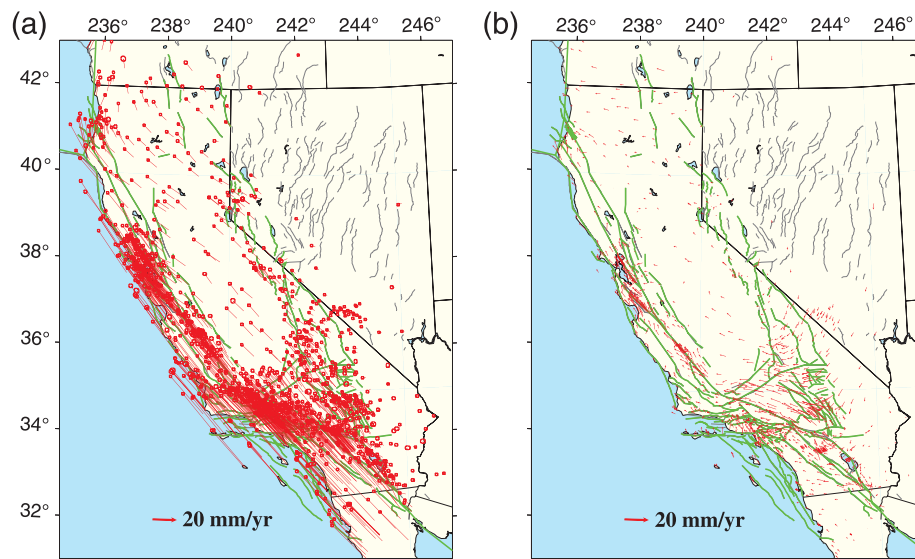


Figure 6. (a) Distribution of UCERF3 GPS velocity vectors for California, referenced to the North America plate (from Appendix C, [Parsons et al., 2013](#)). (b) The residual velocities computed as the difference between observed GPS velocities and those predicted by the UCERF2 Deformation Model 2.1. The velocity scales of the two plots are the same. The residual vectors imply that UCERF2 generally underestimates the average statewide deformation rate, although we do not know how much of the actual deformation is aseismic.

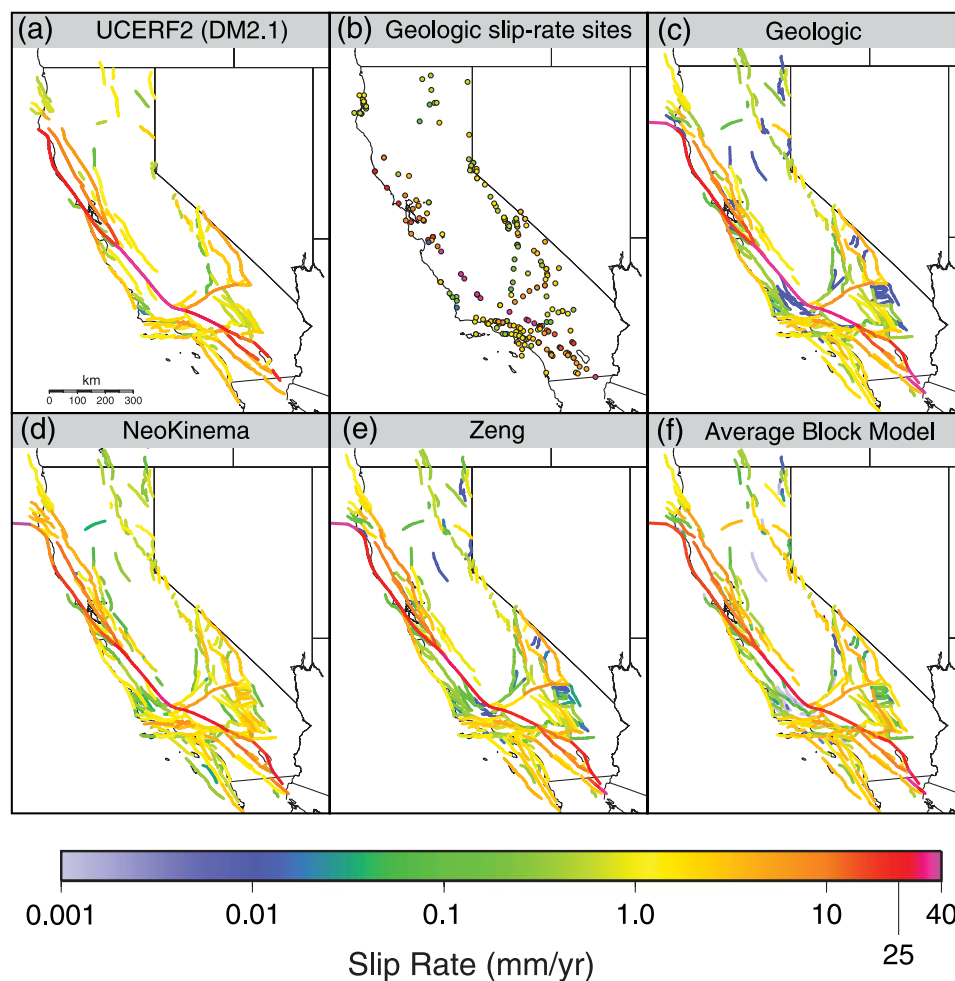


Figure 7. (a) Fault slip rates for the UCERF2 Deformation Model 2.1, (b) sites of geologic slip-rate constraints, and (c–f) fault slip rates for the four UCERF3 deformation models for *Fault Model 3.1*.

is an estimated slip rate at all points on the modeled faults. Where available, these slip rates were assigned using the revised geologic data in Appendix B (Dawson and Weldon, 2013); elsewhere, best-estimate values were taken from UCERF2, except where the latter included hybrid slip rates (from both geology and geodesy) or where the old slip rates were inconsistent with other types of data, such as the USGS rate category (Machette *et al.*, 2004) or published slip rates.

A number of fault sections had no previously assigned slip rate, and these were simply excluded from UCERF2. Such sections have been assigned to a rate category in UCERF3, based primarily on recency of activity, but also on geomorphic expression and comparison to similar, nearby faults with slip rate constraints. The following criteria were applied when using recency of activity to assign slip rate bounds:

- Quaternary active (<1.6 Ma yrs) 0.0 to 0.2 mm/yr
- Late Pleistocene (<~130,000 yrs) 0.2 to 1.0 mm/yr
- Holocene (<~11,000 yrs) 1.0 to 5.0 mm/yr

Very few faults were placed into the last category, primarily because the fastest slipping faults are already well characterized throughout California. The exceptions to this are offshore faults, which are difficult to study. In the absence of other data, the best estimate for each category was selected using a relationship between the number of UCERF fault sections and known slip rates. This weighted mean approach is described in Appendix B (Dawson and Weldon, 2013). The geologic deformation model is displayed in Figure 7c. Table 4 lists the moment rate contributions from the various types of sources in UCERF2, and Table 5 lists the implied moment rates for the new deformation models. Of particular note is that the new faults (UCERF2 faults that lacked slip rates plus the new faults added to UCERF3) constitute a collective moment rate of 0.27×10^{19} N·m/yr (for *FM 3.1*), which is more than half of the total off-fault moment rate in UCERF2 (0.47×10^{19} N·m/yr). The latter represents the off-fault background and type C zone contributions in Table 4. Discounting the added faults, the moment rate of the UCERF3 Geologic Deformation model is about 1% above that of the UCERF2 model.

Deformation Models from Joint Inversion of Geodetic and Geologic Data

Several workshops and meetings were convened to address the UCERF3 goal of deriving slip rates and off-fault strain maps from kinematically consistent inversions of GPS and geologic data (Table 3). Appendix C (Parsons *et al.*, 2013) describes both the GPS database, shown here in Figure 6, and the three UCERF3 deformation models developed by inverting those data together with the geologic constraints:

- *NeoKinema*: A model obtained by inverting geologic, geodetic, and principal stress data using the finite element method of Bird (2009) to estimate the long-term velocity field both on and off faults. It is not based on a block geometry.

Table 4
Moment Rates for the Various Types of Sources in UCERF2

Source Type	Moment Rate (\dot{M}_0)*	Percent of Total Seismic†	Percent of Total‡
California faults ‡	1.73	76%	73%
Non-California faults§	0.07	3%	3%
Off-faults background	0.37	16%	16%
C zones (seismic) #	0.10	5%	4%
C zones (aseismic) #	0.10		4%
Total (seismic)	2.27	100%	
Total (including aseismic)	2.37		100%

* \dot{M}_0 is in units of 10^{19} N·m/yr or 10^{26} dyn·cm/yr.

†The third and fourth columns represent dividing values in the second column by the “Total (seismic)” and “Total (including aseismic)” values, respectively.

‡Value reflects the 10% reduction for smaller earthquakes (generally $M < 6.5$, which are treated as background seismicity) and aftershocks. The UCERF2 faults are only a subset of the UCERF3 fault model, to which about 160 new fault sections have been added.

§Faults outside of California (in Nevada and Oregon) but within the UCERF model region.

||Value does not include type C zones or deep seismicity near Cascadia (in the NSHMP file *agrd_deeps_out*) but does include aftershocks and the special areas for Brawley (1.6×10^{16} N·m/yr), Mendocino (3.7×10^{17} N·m/yr), and creeping San Andreas Fault (1.9×10^{16} N·m/yr).

#Half the moment rate in type C zones was assumed aseismic in UCERF2.

- *Zeng*: A model by Zeng and Shen (2014) representing faults as buried dislocations in a homogeneous elastic half-space. Each fault segment slips at a solved-for slip rate beneath a locking depth, except at a few segments where shallow creep is allowed. A continuity constraint allows adjustment between more and less block-like deformation. The model here is on the less block-like end of that spectrum.
- *Averaged Block Model (ABM)*: A model constructed by averaging five different block models using a kinematically consistent method. The input models were updates of McCaffrey’s DefNode (McCaffrey, 2002, 2005), Hammond’s block model (Hammond *et al.*, 2011), Johnson’s quasi-block model (Johnson and Fukuda, 2010), and special (more block-like) versions of NeoKinema and Zeng’s model. The averaging used the slip rates from all five block-model inversions as data in a unified block model inversion. Residual in-block strain that results from slip on block boundaries is mapped onto identified faults using a buried-dislocation approach, as described previously for the Zeng model (for details, see Appendix C, Parsons *et al.*, 2013). The leftover strain that cannot be reasonably accommodated on faults is the “off-fault” portion (listed in Table 5).

Each deformation model provides slip rate estimates for every UCERF3 fault section. Each also provides off-fault deformation in the form of strain rate tensors on a $0.1^\circ \times 0.1^\circ$ grid covering California, which is converted to an off-fault moment rate grid as described in Appendix C (Parsons *et al.*, 2013). All three models were constrained by a consensus

Table 5
Moment Rates \dot{M}_0 for the UCERF3 Deformation Models*

Fault Model	Deformation Model	On-Fault \dot{M}_0	On-Fault \dot{M}_0 For New Faults [‡]	% From New Faults	\dot{M}_0 Change on UCERF2 faults [§]	Off-Fault \dot{M}_0	Off-Fault \dot{M}_0 Change from UCERF2	Total \dot{M}_0 (including off-fault aseismic)	Total \dot{M}_0 Increase over UCERF2 [¶]	% of Total Off Faults	M_{\max}^{**} $M \geq 8(\text{years})^{**}$	MRI
3.1	ABM ^{††}	1.93	0.35	18%	−9%	0.92	44%	2.85	20%	32%	8.41	207
	Geologic	2.02	0.27	13%	1%							
	NeoKinema	1.76	0.32	18%	−17%	1.02	60%	2.78	17%	37%	8.39	214
	Zeng	1.88	0.28	15%	−8%	0.88	37%	2.76	16%	32%	8.38	216
3.2	ABM	1.92	0.37	19%	−10%	0.92	44%	2.84	20%	33%	8.41	207
	Geologic	2.02	0.28	14%	1%							
	NeoKinema	1.75	0.32	18%	−17%	1.04	63%	2.79	18%	37%	8.39	213
	Zeng	1.88	0.29	16%	−8%	0.88	37%	2.76	16%	32%	8.38	216
2.1	UCERF2	1.73	0.00	0%	0%	0.64	0%	2.37	0%	27%	8.15	385

*Value includes fault-specific down-dip widths and creep-based moment rate reductions; default is 0.1 where no creep data exist. For reference, the average lower seismogenic depth is ~ 12 km in the UCERF3 fault models; with surface creep the average seismogenic thickness is ~ 11 km. Note that UCERF3 does not include most of the UCERF2 “Non-CA Faults” listed in Table 4, so contributions from these are included off fault here. The value of 1.73 listed for UCERF2 includes a 10% reduction for small earthquakes and aftershocks (Table 4), but this is compensated by UCERF3 applying the default aseismicity of 0.1 (which was zero in UCERF2). \dot{M}_0 values are in units of 10^{19} N·m/yr.

[†]These are the on-fault values divided by the value of 1.73 for UCERF2.

[‡]Moment rate contributions from only the more than 150 new fault sections added in UCERF3 (not included in UCERF2). For the geologic model with Fault Model 3.1, 49% percent of the increase (0.28×10^{19} N·m/yr) is from the following two new faults: Cerro Prieto (0.083×10^{19} N·m/yr) and Mendocino (0.054×10^{19} N·m/yr).

[§]Change in on-fault moment rate for the same faults as used in the UCERF2 model.

^{||}Values from off-fault strain rates given in Appendix C (Parsons *et al.*, 2013), which assume a seismogenic thickness of 11 km and include any aseismic processes (because we have no basis for separating them out). The UCERF2 value includes contributions from both “C-Zones (aseismic)” and “Non-CA Faults” (Table 4), the latter because most of the “Non-CA Faults” have been excluded in UCERF3.

[¶]Relative to the UCERF2 total value of 2.37×10^{19} N·m/yr (Table 4), which includes contributions from “C-Zones (aseismic)” in Table 4. The UCERF3 on-fault values have aseismic contributions removed, but there may be aseismic contributions in the UCERF3 off-fault values.

^{**}Maximum magnitude (M_{\max}) and mean recurrence interval (MRI) of $M \geq 8$ earthquakes implied by a truncated Gutenberg–Richter distribution constrained to have the observed rate of $7.9 M \geq 5$ events/yr (appendix L) and a b -value of 1.0.

^{††}ABM, averaged block model.

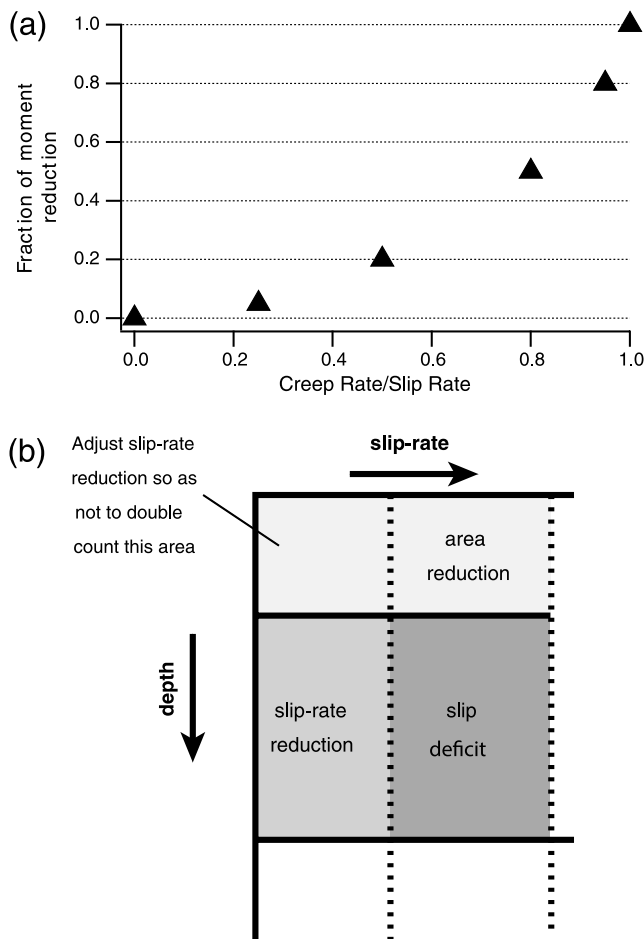


Figure 8. (a) The UCERF3 creep model, which specifies moment rate reduction as a function of the creep-rate-to-slip-rate ratio (referred to as “creep fraction” in the text). (b) The moment rate reductions in the UCERF3 creep model are applied in two ways—as an aseismicity factor, which reduces seismogenic area, and as a coupling coefficient, which reduces the slip rate. See main text, Appendix D (Weldon, Schmidt, *et al.*, 2013) and Appendix N (Page *et al.*, 2013) for further details.

GPS velocity field constructed for this purpose (Appendix C, Parsons *et al.*, 2013), as well as by the geologic slip rate constraints from Appendix B (Dawson and Weldon, 2013). The slip rates for these deformation models are shown in Figure 7. The new fault zone polygons, introduced and defined previously in the **Fault Models** section, were not utilized in the deformation modeling process here.

Creep and Aseismicity

This section describes how inferred creep processes are used to reduce seismogenic rupture areas and slip rates. Here, the term “creep” refers to interseismic creep, which operates over decadal and longer time periods, rather than the post-seismic creep that follows most earthquakes. Appendix D (Weldon, Schmidt, *et al.*, 2013), documents observations of creep on California faults and develops a new methodology to estimate seismic moment rate reductions due to creep.

Their work approximately doubles the number of creep estimates that were available in UCERF2, primarily by utilizing Interferometric Synthetic Aperture Radar (InSAR) and dense geodetic network data. Appendix D also applies a model developed by Savage and Lisowski (1993) to infer how creep extends to depth and examines observations of microrepeating earthquakes (recognized as repeatedly rupturing asperities embedded within a creeping fault surface) to see if they are consistent with the model-predicted creep reduction with depth.

As in UCERF2, the aseismicity factor is defined as the fraction of rupture area, between the upper and lower seismogenic depths, that is reduced by creep, whereas the coupling coefficient defines what fraction of the slip rate is fully seismic (not due to creep). Consequently, nonzero aseismicity factors primarily reduce rupture magnitudes (due to area reduction), whereas coupling coefficients less than 1.0 reduce event rates (due to the slip rate reduction). Both reduce seismic moment rates. This application assumes that any actual rupture into surface creeping areas is nonseismogenic and that some fraction of the slip rate at lower depths can be released aseismically.

Only aseismicity factors were applied in UCERF2, and only about 20% of UCERF2 fault sections had nonzero values. Furthermore, UCERF2 aseismicity factors were assumed to be equal to the surface creep rate divided by the total average slip rate, a ratio hereafter referred to as the “creep fraction.” It is now understood, however, that most creep is shallow and decreases rapidly with depth. By integrating over a depth-dependent creep model, we developed a new relationship for moment rate reduction versus creep fraction (Appendix D, Weldon, Schmidt, *et al.*, 2013). The result, plotted in Figure 8, shows that the moment rate reduction increases less rapidly with creep fraction than in UCERF2; the latter is a straight line with a slope of 1.0. For each fault section, the partitioning of the moment rate reduction between aseismicity factor and coupling coefficient depends on this creep fraction. For values less than 0.9:

$$\text{aseismicity factor} = \text{creep fraction},$$

and

$$\text{coupling coefficient} = 1.0.$$

For creep fractions between 0.9 and 0.95, or for creep fractions between 0.9 and 1 on the San Andreas creeping section:

$$\text{aseismicity factor} = 0.9,$$

and

$$\text{coupling coefficient} = 1.0 - 10 \times (\text{creep fraction} - 0.9).$$

That is, coupling coefficient varies linearly from 0.0 to 0.5 for creep fractions between 0.9 and 0.95, with the relatively complicated functional form being needed to avoid double counting (Fig. 8b). Values are capped for creep fractions above 0.95 according to the following:

aseismicity factor = 0.9,

and

coupling coefficient = 0.5.

As discussed in Appendix N (Page *et al.*, 2013), the transition threshold at 0.9 was chosen to ensure that Parkfield gets an area reduction consistent with the M 6.0 events that have historically occurred on that fault section. Slip rate reductions on highly creeping faults act to limit the rate of through-going ruptures (e.g., see Appendix N [Page *et al.*, 2013] for discussion of the San Andreas creeping section). The dependence on long-term slip rates implies that the moment rate reductions vary among the deformation models (average aseismicity factor and coupling coefficient values are listed for each fault section in the U3 Fault Section Data file given in the [Data and Resources](#) section).

In UCERF2, the moment rate reduction was set to zero for faults with no creep data. However, it is very difficult to recognize creep on most California faults, where slip rates are on the order of a few mm/yr, especially for low creep fractions. To account for this observational bias, UCERF3 applies a default aseismicity factor of 0.1 where data are lacking, which is the approximate average over all fault sections that have data, including those that are known not to creep. This implies a default 10% reduction in area and, consequently, in moment rate. Again, aseismicity factors are applied to fault areas when computing rupture magnitudes, and coupling coefficients are applied to slip rates before inverting for long-term event rates.

Implied Moment Rates

This section discusses the moment rate implications of the various deformation models. However, it is worth noting here that only the on-fault contributions directly influence the UCERF3 forecast. While the off-fault contributions are not directly used, they will serve as a useful basis for comparison to the values effectively implied by other UCERF3 assumptions. Moment rate statistics for the UCERF3 deformation models are compared with UCERF2 in Table 5; the on-fault values have been reduced by creep as described previously (see [Creep and Aseismicity](#) section), whereas off-fault values for the UCERF3 deformation models include any aseismic processes (which are currently unknown). The total implied moment rates for the UCERF3 deformation models range from 2.76×10^{19} N·m/yr to 2.85×10^{19} N·m/yr, which is a 16%–20% increase over the UCERF2 value of 2.37×10^{19} N·m/yr; the latter includes both the seismic and aseismic contributions listed in Table 5. This increase is consistent with the residuals shown in Figure 6b, which are independent of the UCERF3 models. Also listed are the implied M_{\max} and mean recurrence intervals for $M \geq 8$ events (assuming a truncated Gutenberg–Richter [GR] distribution), none of which appear unreasonable to us from a total moment rate perspective.

The on-fault moment rates for the UCERF3 models imply an increase between 1% and 17% relative to UCERF2, all of which result from adding new faults (total moment rate changes, considering only the same faults, vary between +1% and –17%). For the geologic deformation model, 49% of the new-fault increase comes from just two fault section additions: Cerro Prieto (0.083×10^{19} N·m/yr) and Mendocino (0.054×10^{19} N·m/yr).

Compared to UCERF2, off-fault moment rates increased from 37% to 60% among the new models. However, we note again that off-fault moment rates are not used as a direct constraint in UCERF3 (but are actually implied by other logic-tree choices, as discussed in the [Inversion Setup and Associated Gridded Seismicity](#) section). In terms of the percentage of the total moment rate that is off-fault, the new deformation models have values between 32% and 37%, a bit higher than the UCERF2-implied value of 27%.

Figure 9 shows the spatial distribution of the off-fault and total moment rates given by the three GPS-based models (the geologic deformation model does not provide off-fault deformation), as well as total moment rate ratios with respect to UCERF2 and the UCERF3 average. In general, the UCERF3 models are in better agreement with each other than with UCERF2, at least for off-fault moment rates. The ratios with UCERF2 show the biggest differences near the edges of the RELM region.

The total deformation model moment rate distributions can be compared to smoothed seismicity, which was used in UCERF2 for defining off-fault earthquakes rates. Two smoothed seismicity models are used in UCERF3, one from UCERF2, based on a 50 km Gaussian smoothing function, and a new model based on an adaptive smoothing approach. Both are discussed in the context of defining the forecast model (see [Off-Fault Spatial Seis PDF](#) section), and details on how they were created are given in Appendix M (Felzer, 2013c). Figure 10 compares the moment rate maps implied by these two smoothed-seismicity models with that of the average UCERF3 deformation model (see the figure caption for some important assumptions). The differences can be explained by one or more of the following: (1) problems with the deformation models, (2) temporal seismicity rate changes not reflected in the earthquake catalog, (3) inadequate after-shock declustering in the smoothed seismicity maps, (4) spatially dependent aseismicity, (5) catalog completeness issues in some areas, (6) the existence of characteristic magnitude–frequency distributions on faults, (7) Gutenberg–Richter b -value and/or maximum magnitude variability, or (8) that there is no significant difference given overall uncertainties. We had originally hoped to set off-fault event rates using smoothed seismicity and to then set maximum magnitudes to match the spatial variability of off-fault moment rates from the deformation models. This does not work, however, because some areas would need $M \geq 10$ events to satisfy both the seismicity and deformation model moment rates.

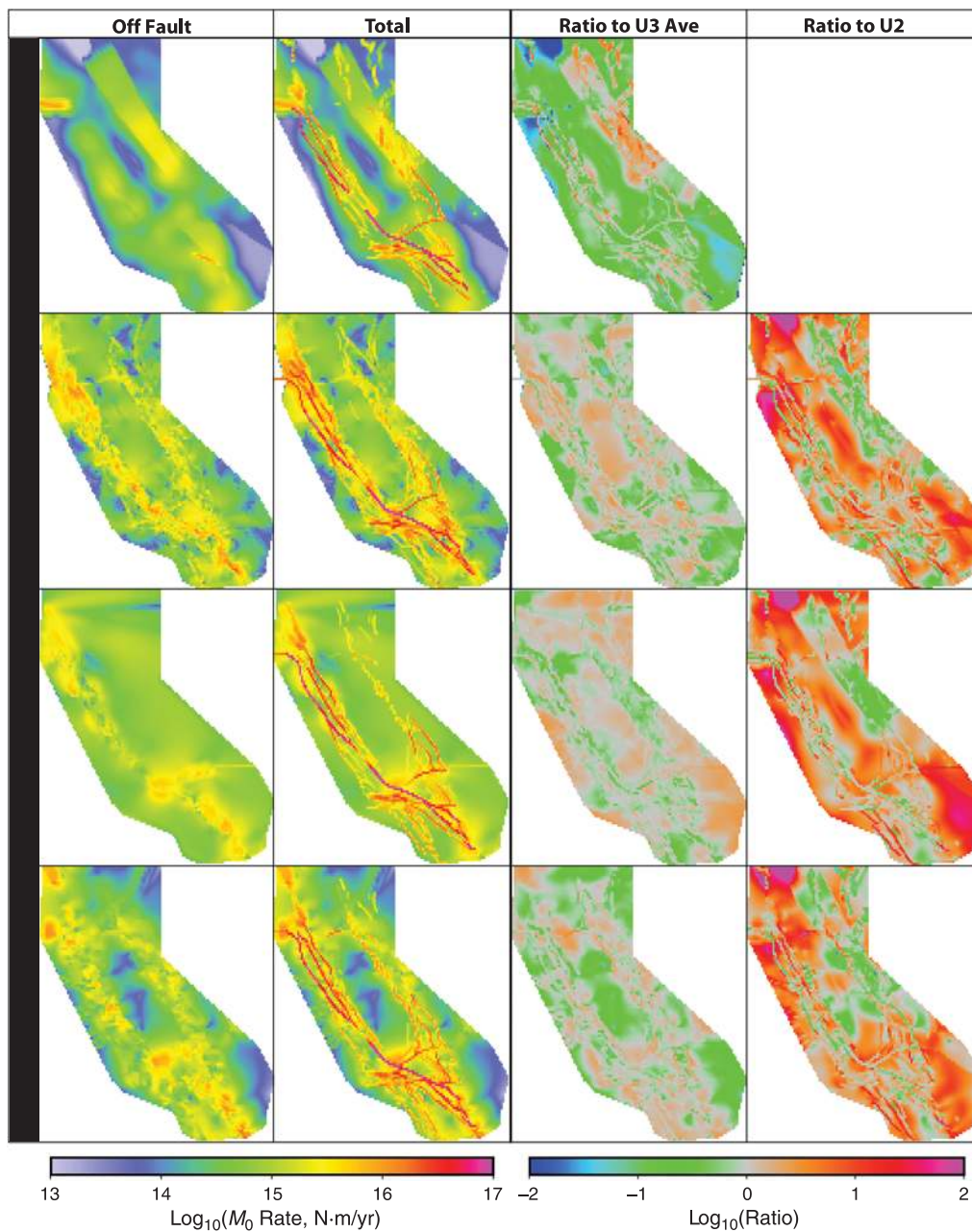


Figure 9. Spatial distribution of off-fault moment rates (first column) for the three UCERF3 deformation models that provide such estimates (and for *Fault Model 3.1* only), together with that implied by the UCERF2 forecast model (including both gridded sources and type C zones). Total moment rates (that is, including faults) are shown in the second column, and ratios with respect to the average UCERF3 results are shown in the third column (giving equal weight to each model, rather than the branch weights shown in Fig. 3). Ratios with respect to UCERF2 are shown in the fourth column. Details on how UCERF3 off-fault moment rate maps were computed, such as an assumed seismogenic thickness of 11 km, are given in Appendix C (Parsons *et al.*, 2013).

Logic-Tree Branch Weights

A complete description of deformation-model weighting is given in Appendix C (Parsons *et al.*, 2013), only a brief summary of which is provided here. All the UCERF3 deformation models fit their input datasets within overall observational uncertainties. The models generally fit the geologic observations better than the geodetic data, mostly because the former were given higher weight to avoid strong

along-fault slip rate variations that can occur when over-fitting geodetic data. By design, the geologic deformation model fits the geologic data averages exactly. However, the geologic constraints on a significant fraction of California faults (~30%) are very weak to nonexistent, which was the primary reason to commission geodetic models in the first place. NeoKinema represents the best fit to GPS data, with average misfits three times lower than for the ABM and Zeng deformation models. The Zeng deformation model applies

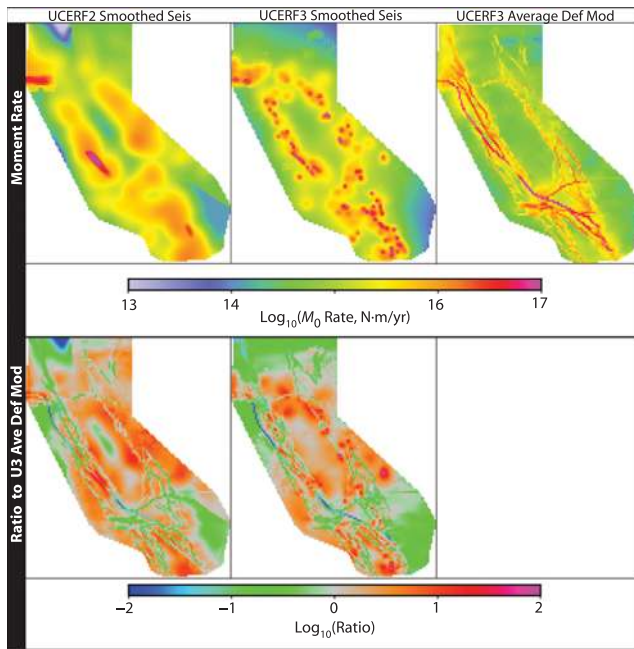


Figure 10. The spatial distribution of moment rates implied by the UCERF2 smoothed seismicity model (Appendix J, [Petersen, Mueller, et al., 2007](#)) and the new UCERF3 smoothed seismicity model (Appendix M, [Felzer, 2013c](#)), compared to the average UCERF3 deformation model (described in Fig. 9). The smoothed seismicity maps have the same total moment rate as the UCERF3 average, and they essentially assume a Gutenberg–Richter distribution with the same maximum magnitude everywhere. Also shown are ratios of the smoothed seismicity maps to the UCERF3 average (bottom row).

the minimum possible changes to geologic constraints in fitting GPS data and is explicitly constrained to stay within geologic bounds on most faults.

In addition to consistency with geologic and geodetic data, Appendix C ([Parsons et al., 2013](#)) also ranks the models in terms of overall moment rate, fit to plate tectonic rates and directions, and the amount of off-fault deformation. All information was given to an *ad hoc* expert committee for evaluation and weighting. Members had varying opinions with respect to the value of each evaluation metric, which led to a wide range of suggested branch weights, but most members gave more credence to geologic observations.

The models underwent further evaluation, review, and fine tuning following the *ad hoc* committee’s deliberations, with three fault-by-fault evaluation meetings being particularly influential (Table 3). The final UCERF3 weights are NeoKinema (30%), Zeng (30%), ABM (10%), and Geologic (30%) (also shown in Fig. 3).

The ABM deformation model has the lowest weight because it tends to have relatively high slip rates at its block boundaries, which might be an artifact of the approach. The Zeng deformation model reflects minimal changes to geologic constraints; therefore the collective weight for the more geologic models is 0.6, and that for the more geodetic models (ABM and NeoKinema) is 0.4. This balance reflects

our perspective on the applicability of short-term geodetic signals versus relatively long-term geologic slip rates in determining earthquake likelihoods in California. Whether the optimum balance should vary with forecast duration is a question for further study. We also note that final UCERF3 models do not necessarily match all slip rates exactly, because these constraints are weighed against others in the inversion. These deformation-model weights are therefore *a priori* and subject to effective modification.

Earthquake Rate Models and the “Grand Inversion”

The earthquake rate component of the UCERF3 model framework (Fig. 2) defines the long-term rate of all possible earthquake ruptures above the magnitude threshold, $M \geq 5$, and with a discretization sufficient to represent hazard. Each earthquake rate model comprises two types of sources: (1) ruptures with dimensions larger than the seismogenic depth occurring on explicitly modeled faults, referred to as “supra-seismogenic” on-fault ruptures, and (2) other earthquakes, modeled as seismicity on a $0.1^\circ \times 0.1^\circ$ geographic grid with each cell assigned a magnitude–frequency distribution (MFD) of earthquake nucleation rates. The gridded seismicity, which is sometimes referred to as background seismicity, is separated into events inside fault zone polygons (subseismogenic on-fault ruptures) and those outside all fault zone polygons (off-fault ruptures). Cells partly inside and partly outside a fault zone polygon are fractionally apportioned. The complete bookkeeping details are given in Appendix O ([Powers and Field, 2013](#)).

In UCERF2, the models for each fault were constructed separately, and background seismicity was then added. The UCERF3 procedure solves for the rates of all events simultaneously using the inversion method of [Field and Page \(2011\)](#), which builds on the work of [Andrews and Scherer \(2000\)](#). This unified, system-level approach enables the relaxation of fault segmentation and the inclusion of multifault ruptures, two major goals of UCERF3. Its implementation, details of which are also given in Appendix N ([Page et al., 2013](#)), has been dubbed the “grand inversion.” Aftershocks are directly included in the UCERF3 long-term rate model. To facilitate certain applications, we provide a procedure for removing aftershocks (in the [Gardner–Knopoff Aftershock Filter](#) section), which is consistent with previous NSHMP practice.

Methodology

We first consider only those ruptures that occur on the faults included in the UCERF3 fault and deformation models and only model events that have rupture lengths greater than or equal to the local seismogenic thickness. To relax segmentation, we subdivide each fault section into equal length subsections, with lengths that are about half the seismogenic thickness, resulting in $S = 2606$ total subsections for *FM 3.1* (Fig. 11), and $S = 2664$ subsections for *FM 3.2*. The

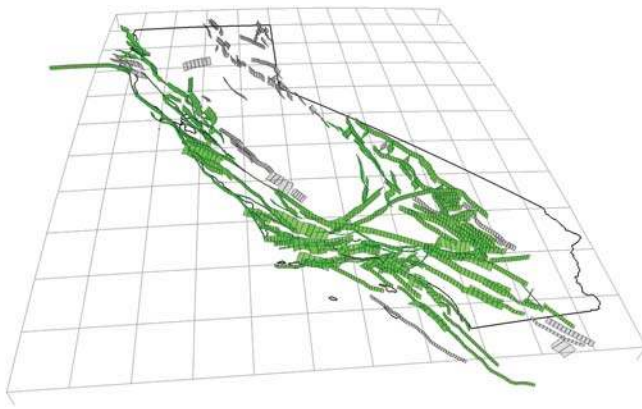


Figure 11. UCERF3 *Fault Model 3.1* sections divided into an integer number of equal length subsections (lengths equal to, or just less than, half the section's seismogenic thickness). All subsections shown in green are connected to all others in green without jumping more than 5 km between faults.

surfaces of possible ruptures are taken to be the complete set of two or more contiguous fault subsections. Requiring at least two subsections ensures that the minimum rupture lengths are approximately equal to the seismogenic thickness. The rupture set is filtered by retaining only ruptures that pass all of the following plausibility criteria, as detailed in Appendix T (Milner *et al.*, 2013):

1. All fault sections connect within 5 km or less, as assessed in Appendix J (Biasi, Parsons, *et al.*, 2013).
2. Ruptures cannot include a subsection more than once.
3. Ruptures must contain at least two subsections of any main fault section, unless the only way two fault sections can connect is through a single-subsection connector, as described in Appendix T (Milner *et al.*, 2013).
4. Ruptures can only jump between fault sections at their closest points (in 3D).
5. The maximum azimuth change between neighboring subsections is 60° , except for left-lateral to right-lateral connections such as Garlock to the San Andreas.
6. The maximum azimuth change between the first and last subsection is 60° , except for left-lateral to right-lateral connections such as Garlock to the San Andreas.
7. The maximum cumulative rake change (summing over each neighboring subsection pair) is 180° , based on rakes of the geologic deformation model to ensure rupture-set consistency.
8. The maximum cumulative azimuth change, computed by summing absolute values over each neighboring subsection pair, is less than 560° (a filter that reduces squirrelness; that is, many changes of azimuth).
9. Branch points (potential connections between main fault sections) must pass a Coulomb criterion that earthquake triggering between the two fault sections is physically reasonable, as described in Appendix T (Milner *et al.*, 2013).

This filtering produces 253,706 and 305,709 unique viable ruptures for *FM 3.1* and *FM 3.2*, respectively. In comparison,

mapping the UCERF2 ruptures onto their nearest equivalents in the *FM 3.1* yields only 7773 ruptures. The much larger UCERF3 rupture set reflects the high connectivity of the California fault system—nearly all the fault sections connect to each other without jumping more than 5 km (green subset in Fig. 11). Again, it is believed that ignoring this connectivity in UCERF2 may have contributed to an overprediction of moderate-size earthquake rates. In any case, UCERF2 generally lacks types of multifault ruptures that have been seen in nature.

It is important to note, however, that UCERF3 rupture sets are still an approximation of the system. For example, the 5 km fault separation cutoff, which is based on both theoretical and empirical studies (Harris and Day, 1993; Wesnousky, 2006), presumes knowledge of fault connectivity at depth that we do not have. Of the viable ruptures that pass the plausibility criteria, one could almost certainly identify at least a few that are in some ways less likely than ruptures that have been filtered out. The relevant question is whether the current approach is a better approximation than largely ignoring multifault ruptures (as in UCERF2). Moreover, seismic hazard is more sensitive to the combined magnitude–frequency distribution of nearby faults, rather than to the details of individual ruptures, as will be discussed in the Results section.

The inversion method estimates the long-term rates of the R viable ruptures $\{f_r; r = 1, 2, \dots, R\}$ by solving the system of equations described in Table 6. The equations can be weighted by the uncertainties in the data and/or by the degree of belief in the importance of a particular constraint. Conceptually, this approach is simpler, more objective, and more reproducible than that adopted in UCERF2. For example, the (largely artificial) distinction between type A and type B faults has been dropped, and type C zones have been merged into off-fault seismicity.

In addition to setting equation-set weights, subjectivity is also involved in assigning weights to alternative logic-tree branches. Both of these, however, can be guided by how well the models fit the data. What the grand inversion really represents is a system-level framework both for incorporating expert judgment and identifying a more complete range of models that are consistent with all available data. The framework is also extensible in that other equation-set constraints could easily be added to the list in Table 6; as we said repeatedly during development and review, “tell us what you don’t like about a result and you have given us a new inversion constraint.”

In an exploratory study, Field and Page (2011) solved the inverse problem by the nonnegative least squares algorithm of Lawson and Hanson (1974). This algorithm is not computationally feasible for an inversion using the statewide system of faults. Therefore, we have developed a parallelized code that can efficiently solve very large equation sets by simulated annealing, as described in Appendix N (Page *et al.*, 2013). Because of the stochastic nature of the algorithm, simulated annealing can also provide a range of models that sample the

Table 6

The Grand Inversion System of Equations Used in Solving for the Long-Term Rate of Fault-Based Ruptures

Equation Set	Description
$\sum_{r=1}^R D_{sr} f_r = v_s$	(1) Slip Rate Balancing: v_s is the subsection slip rate (from a deformation model) and D_{sr} is the slip on the s th subsection in the r th event, averaged over multiple occurrences of the rupture and as measured at midseismogenic depth.
$\sum_{r=1}^R G_{sr} P_r^{\text{paleo}} f_r = f_s^{\text{paleo}}$	(2) Paleoseismic Event Rate Matching: f_s^{paleo} is a paleoseismically inferred event rate estimate, G_{sr} specifies whether the r th rupture utilizes the s th subsection (0 or 1), and P_r^{paleo} is the probability that the r th rupture would be seen in a paleoseismic trench.
$R_s^m = \frac{R_{s-1}^m + R_{s+1}^m}{2}$	(3) Fault Section Smoothness Constraint: This enables forcing the nucleation rate, R , in the m th magnitude bin to vary smoothly along a fault section, where the $s-1$ and $s+1$ subsections are adjacent to the s th subsection.
$\lambda_r f_r = 0$	(4) Improbability Constraint: This allows us to force relatively improbable events to have a lower rate (e.g., based on multifault rupture likelihoods). A higher value adds more misfit for a given rupture rate, forcing the inversion to minimize that rupture rate further.
$f_r = f_r^{\text{a-priori}}$	(5) a priori Constraint: This constrains the rates of particular ruptures to target values, either on an individual basis (e.g., make Parkfield occur every ~25 years) or for a complete rupture set (e.g., as close as possible to those in UCERF2).
$\sum_{r=1}^R M_{gr}^m f_r = R_g^m$	(6) Regional MFD Constraint: This enables a geographic region, g , to be forced to have a specified magnitude–frequency distribution (MFD), such as Gutenberg–Richter. R_g^m represents the nucleation rate for the m th magnitude bin in the g th region. Matrix $M_{gr}^m f_r$ contains the product of whether the r th rupture falls in the m th magnitude bin (0 or 1) multiplied by the fraction of that rupture that nucleates in the g th region.
$\sum_{r=1}^R M_{sr}^m f_r = R_s^m$	(7) Fault Section MFD Constraint: This enables forcing subsections to have specific nucleation MFDs. R_s^m is the nucleation rate for the m th magnitude bin on the s th subsection. Matrix $M_{sr}^m f_r$ contains the product of whether the r th rupture falls in the m th magnitude bin (0 or 1) multiplied by the fraction of that rupture that nucleates on the s th subsection.

f_r represents the frequency or rate of the r th rupture (what we are solving for). Important implementation details, such as equation-set weighting, are given in Appendix N (Page et al., 2013).

solution space of the inverse problem, which generally is underdetermined, or mixed determined at best. This sampling can be used to represent the epistemic uncertainty associated with model nonuniqueness.

Appendix N also discusses a number of important inversion implementation details, including the tuning of equation-set weights, the sensitivity of the results to those weights, final misfits with respect to the various data constraints, reproducibility tests based on synthetic datasets, and alternative simulated annealing algorithms. With respect to the influence of model nonuniqueness on hazard estimates, the [Sensitivity Tests](#) section demonstrates that this is not an issue, at least not for traditional hazard metrics.

Implementation Ingredients

This section describes the various data and models used in the grand inversion, organized according to the equation sets of Table 6.

Slip Rate Balancing (Equation Set 1). Equation set (1) of Table 6 involves satisfying the fault section slip rates (v_s) defined by the given deformation model and reduced by the coupling coefficient defined in the [Creep and Aseismicity](#) section. Doing so requires knowledge of the average slip on the s th subsection in the r th rupture (D_{sr}), where the average is over multiple occurrences of the event and where the slip value is that at midseismogenic depths. Using such slip rate matching, rather than the moment rate balancing of previous WGCEPS, avoids potential depth-of-rupture ambiguities.

We first compute the average slip for a given rupture D_r and then partition this among the subsections to get D_{sr} .

The magnitude of each rupture is computed from a magnitude–area relationship $M(A_r)$, in which A_r is the sum of associated section areas (each reduced by its aseismicity factor). In UCERF2, the [Hanks and Bakun \(2008\)](#) and [Ellsworth B \(WGCEP, 2003\)](#) relationships were used with equal weights. For UCERF3, we have also included a slightly modified version of the [Shaw \(2009\)](#) relationship, as justified in [Shaw \(2013a\)](#) and Appendix E ([Shaw, 2013b](#)). These three relationships, referred to hereafter as *HanksBakun08*, *EllsworthB*, and *Shaw09mod*, are plotted in Figure 12, and their functional forms are as follows.

HanksBakun08 ([Hanks and Bakun, 2008](#)):

$$M = 3.98 + \log(A) \quad \text{if } A \leq 537 \text{ km}^2 \quad (M \leq 6.71) \\ = 3.07 + (4/3) \log(A) \quad \text{if } A > 537 \text{ km}^2 \quad (1)$$

EllsworthB ([WGCEP, 2003](#)):

$$M = 4.2 + \log(A) \quad (2)$$

Shaw09mod ([Shaw, 2009, 2013a](#)):

$$M = 3.98 + \log(A) + \left(\frac{2}{3}\right) \log \left(\frac{2 \max(1.0, \sqrt{\frac{A}{W_o^2}})}{1 + \max(1.0, \sqrt{\frac{A}{7.4 W_o^2}})} \right) \quad (3)$$

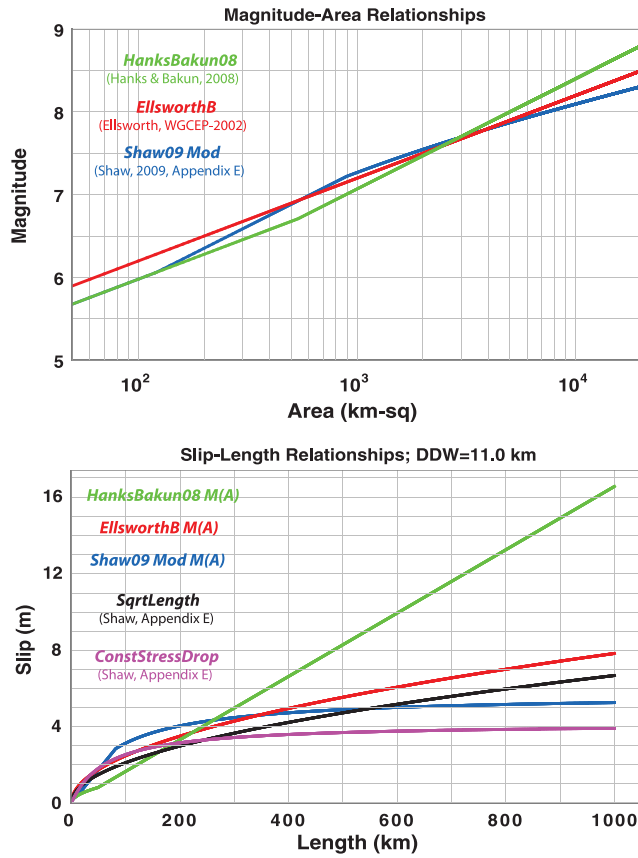


Figure 12. The magnitude–area (top) and slip–length (bottom) relationships used in UCERF3, which are documented in Appendix E (Shaw, 2013b). The $M(A)$ -derived slip–length curves at the bottom assume an average seismogenic thickness of 11 km in converting area to length.

In these relationships, M is magnitude, A is area (km, and reduced by aseismicity factor), and W_o is the original down-dip width (unreduced by aseismicity).

Two different approaches are used to get D_r for each rupture. One, used in UCERF2, involves converting the magnitude from the $M(A_r)$ relationship to moment and then dividing by the rupture area A_r and shear modulus μ to get D_r :

$$D_r = \frac{M_{0r}}{\mu A_r} = \frac{10^{1.5 \times M(A_r) + 9.05}}{\mu A_r},$$

in which M_{0r} is the moment of the r th rupture. The shear modulus (μ) is assumed to be 3.0×10^{10} Pa throughout this report.

Because A_r is based on the depth of microseismicity, D_r might be an overestimate if slip extends below such depths in larger ruptures. Therefore, an alternative is to obtain D_r using one of two viable slip–length scaling relationships, which have been derived from surface-slip observations (Shaw, 2013a), and updated here in Appendix E (Shaw, 2013b) using the enhanced UCERF3 surface slip database in Appendix F (Biasi, Weldon, and Dawson, 2013). The first, which assumes slip scales as the square root of length, is given as

Table 7

Magnitude–Area and Slip–Length Model Combinations Used in UCERF3

Magnitude–Area Relationship	Slip–Length Relationship	Branch Weight (%)
<i>EllsworthB</i>	<i>EllsworthB</i>	20
<i>HanksBakun08</i>	<i>HanksBakun08</i>	20
<i>Shaw09mod</i>	<i>Shaw09mod</i>	20
<i>EllsworthB</i>	<i>SqrtLength</i>	20
<i>Shaw09mod</i>	<i>ConstStressDrop</i>	20

See Appendix E (Shaw, 2013b) for full equations and explanations.

SqrtLength:

$$D_r = 0.22 \sqrt{L_r}, \quad (4)$$

in which L_r is length in km. The second, which assumes constant stress drop, is given as

ConstStressDrop:

$$D_r = 0.151 \left[\frac{7}{3L_r} + \frac{1}{30} \right]^{-1}. \quad (5)$$

Appendix E of Shaw (2013b) gives the full functional forms in terms of physical parameters. Neither of these relationships is applicable when the average aseismicity factor is ≥ 0.2 ; in such cases, D_r is obtained from magnitude and area.

Examples obtained using these two slip–length models, as well as using the three magnitude–area relationships above, are given in Figure 12 (bottom). The slip–length models generally give a smaller D_r for longer ruptures, which could be real (e.g., due to slip penetrating below the depth of microseismicity) or it could represent a bias in slip measurements (e.g., surface values being lower than those at seismogenic depths). Adding these slip–length relationships therefore provides an element of epistemic uncertainty not included in UCERF2.

As discussed in Appendix E, some magnitude–area and slip–length relationship combinations are incompatible with the underlying assumptions. For example, using *HanksBakun08* (equation 1) to get magnitude from area and then using *ConstStressDrop* (equation 5) to get slip from length can lead to unreasonably large widths for long ruptures. Table 7 lists the combinations allowed in UCERF3, together with their associated weights, which are also shown in Figure 3. All branches are given equal weight in UCERF3.

We need to partition D_r among the subsections used by each rupture to get D_{sr} , which again represents the average over multiple occurrences of the rupture. As discussed in Appendix F (Biasi, Weldon, and Dawson, 2013), the preferred choice is the observationally based tapered-slip (square-root-sine) model of Weldon *et al.* (2007), which is shown in Figure 13. This tapered-slip model was applied in UCERF2 when solving for the rate of ruptures on type

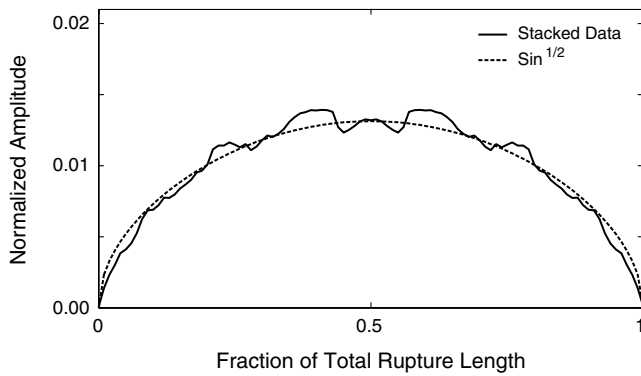


Figure 13. Mean rupture profile based on a stack of 13 mapped surface ruptures. The stack was obtained by normalizing the observed profiles to unit length and averaging them with their reflections about the midpoint. The details of this analysis are presented in UCERF2 Appendix E (Weldon *et al.*, 2007).

A faults. The assumption here is that intraevent, along-strike slip variability averages out over multiple occurrences to yield the tapered shape. In UCERF3, this tapered-slip model is also applied to multifault ruptures, implying that there is no pinching out of the average slip at fault stepovers.

The choice of D_{sr} model should be consistent with how slip rates vary in the deformation model; for example, if slip is persistently low at fault stepovers, then the slip rates should be lower there too. Because the deformation models do not resolve such along-strike slip rate variations, applying a multirainbow shape is not warranted, especially given the epistemic uncertainty about what is happening at seismogenic depths. However, because the deformation model slip rates do not ramp down toward the ends of faults that terminate (i.e., where there are no connections to other faults), applying the tapered slip might artificially introduce a higher rate of smaller earthquakes to satisfy slip rates at these endpoints. To minimize this potential problem, UCERF3 also uses a uniform (boxcar) slip distribution ($D_{sr} = D_r$) as an alternative logic-tree branch, and the two options are given equal weight. A more correct solution may be to taper both the slip and the slip rates at fault terminations or intersections. Better observations are needed to constrain how the multifault slip functions actually vary in nature.

The UCERF3 framework is capable of applying the WGCEP (2003) D_{sr} model, in which the slip is proportional to the slip rate of each subsection. However, this option is given zero weight for the same reasons it was excluded in UCERF2—lack of observational support and implications that some ruptures cannot happen. There is some evidence to support a characteristic slip model in which the amount of slip on a subsection is similar for all ruptures (Hecker *et al.*, 2013), but applying this would be difficult because of very limited observational constraints, which would require the propagation of large epistemic uncertainties that have unknown spatial correlations. Instead, we compare the slip-per-event implications of UCERF3 with the results from Hecker *et al.* (2013).

Because the inversion is solving for the rate of seismogenic thickness and larger ruptures, the slip rates in equation set (1) need to be reduced to account for the moment released in subseismogenic events. This correction differs between the *Characteristic* and *Gutenberg–Richter* logic-tree branches (listed under *Inversion Model* in Fig. 3), details of which are given in the *Inversion Setup and Associated Gridded Seismicity* section.

Paleoseismic Event Rate Matching (Equation Set 2). Equation set (2) in Table 6 matches event rates derived from paleoseismic trench studies. Not all ruptures that occur beneath a site are paleoseismically observable, so we use the factor P_r^{paleo} to specify the probability that the r th rupture will be seen in a trench study. In UCERF3, there are two types of event rate constraints: (1) direct event rates derived from paleoseismically observed dates of events; and (2) proxy event rates obtained from average slip-per-event data, in which the proxy rate equals slip rate divided by the average slip. We distinguish f_r^{paleo} and P_r^{paleo} for these two data types as $f_r^{\text{paleo-event-rate}}$ and $P_r^{\text{paleo-event-rate}}$ versus $f_r^{\text{paleo-slip-proxy}}$ and $P_r^{\text{paleo-slip-proxy}}$, respectively.

Appendix G (Weldon, Dawson, and Madden, 2013) provides an updated compilation of event dates for various paleoseismic studies in California, and Appendix H (Biasi, 2013) provides estimates of the mean paleoseismic event rates, $f_r^{\text{paleo-event-rate}}$, implied by these data. The updated rates are compared with values used in UCERF2 in Table 8, where we now have 31 constraints (nine more than in UCERF2).

A new model for the probability of seeing a given rupture in a trench, $P_r^{\text{paleo-event-rate}}$ is given in Appendix I (Weldon and Biasi, 2013). The probability depends on both the average slip of the rupture D_r and the position of the site relative to the nearest end of the rupture, implying that one is less likely to observe surface offsets near the ends of a rupture, consistent with the tapered slip model. Table 9 lists representative values for $P_r^{\text{paleo-event-rate}}$. In principle, this could be done on a trench-by-trench basis to account for the unique depositional environment at each site. The probability model adopted in UCERF3, however, is generic.

Appendix R (Madden *et al.*, 2013) provides a compilation of average slip-per-event data, derived from either offset features or paleoseismic trench studies (where available) for California faults. These are reproduced here in Table 10, which also lists the associated proxy event rates, $f_r^{\text{paleo-slip-proxy}}$, implied by each deformation model. Although measurement uncertainties are given for the average slips in Appendix R (Madden *et al.*, 2013), the associated confidence bounds are not listed in Table 10 because they do not reflect the additional uncertainty due to the limited sampling of events. Appendix R also provides a model for $P_r^{\text{paleo-slip-proxy}}$, which represents a simple linear interpolation between the values listed here in Table 11.

Fault Section Smoothness Constraint (Equation Set 3). A problem we encountered in an earlier version of the model

Table 8
Event Rate Estimates and Mean Recurrence Intervals (MRIs) at Paleoseismic Sites*

Site	Latitude (°)	Longitude (°)	Mean Rate (per yr)	16%	84%	MRI (yr)	16%	84%	UCERF2
Calaveras fault—North	37.5104	−121.8346	1.62E-03	1.16E-03	2.24E-03	618	446	859	445
Compton	33.9660	−118.2629	3.76E-04	2.46E-04	5.72E-04	2658	1748	4059	
Elsinore—Glen Ivy	33.7701	−117.4909	5.58E-03	4.63E-03	6.77E-03	179	148	216	291
Elsinore fault—Julian	33.2071	−116.7273	3.08E-04	5.35E-05	5.62E-04	3251	1779	18702	1193
Elsinore—Temecula	33.4100	−117.0400	9.81E-04	5.23E-04	1.88E-03	1019	533	1914	741
Elsinore—Whittier	33.9303	−117.8437	3.13E-04	5.45E-05	5.73E-04	3197	1747	18358	1256
Frazier Mountain, SSAF	34.8122	−118.9034	6.73E-03	4.97E-03	9.09E-03	149	110	201	
Garlock Central (all events)	35.4441	−117.6815	6.97E-04	4.59E-04	1.06E-03	1435	941	2178	729
Garlock—Western (all events)	34.9868	−118.5080	8.13E-04	5.29E-04	1.25E-03	1230	798	1889	711
Green Valley—Mason Road	38.2341	−122.1619	3.41E-03	2.50E-03	4.66E-03	293	215	399	
Hayward fault—North	37.9306	−122.2977	3.14E-03	2.52E-03	3.92E-03	318	255	396	363
Hayward fault—South	37.5563	−121.9739	5.97E-03	5.24E-03	6.80E-03	168	147	191	210
N. San Andreas—Alder Creek	38.9813	−123.6770	1.15E-03	2.01E-04	2.11E-03	870	474	4984	
N. San Andreas—Santa Cruz	36.9626	−121.6981	9.10E-03	7.04E-03	1.18E-02	110	85	142	115
N. San Andreas—Fort Ross	38.5200	−123.2400	3.27E-03	2.74E-03	3.88E-03	306	258	366	360
N. San Andreas—North Coast	38.0320	−122.7891	3.79E-03	3.03E-03	4.73E-03	264	211	330	248
N. San Andreas—Offshore Noyo	39.5167	−124.3333	5.33E-03	4.63E-03	6.14E-03	188	163	216	
Puente Hills	33.9053	−118.1104	2.85E-04	2.32E-04	3.52E-04	3506	2842	4313	
San Gregorio—North	37.5207	−122.5135	9.81E-04	1.72E-04	1.80E-03	1019	554	5824	480
Rodgers Creek	38.2623	−122.5334	3.07E-03	1.99E-03	4.79E-03	325	209	503	
San Jacinto—Hog Lake	33.6153	−116.7091	3.21E-03	2.41E-03	4.28E-03	312	234	416	233
San Jacinto—Superstition	32.9975	−115.9436	1.97E-03	1.07E-03	3.65E-03	508	274	938	402
S. SAF—Carrizo Bidart	35.2343	−119.7887	8.72E-03	6.49E-03	1.17E-02	115	86	154	
S. San Andreas—Burro Flats	33.9730	−116.8170	4.87E-03	3.68E-03	6.41E-03	205	156	272	234
S. San Andreas—Coachella	33.7274	−116.1701	5.60E-03	4.16E-03	7.55E-03	179	132	241	
S. San Andreas—Indio	33.7414	−116.1870	3.61E-03	2.81E-03	4.61E-03	277	217	357	358
S. San Andreas—Pallett Creek	34.4556	−117.8870	6.70E-03	5.45E-03	8.26E-03	149	121	184	136
S. San Andreas—Pitman Canyon	34.2544	−117.4340	5.76E-03	4.47E-03	7.41E-03	174	135	224	261
S. San Andreas—Plunge Creek	34.1158	−117.1370	4.87E-03	3.67E-03	6.28E-03	205	159	272	361
S. SAF M. Creek—1000 Palms	33.8200	−116.3010	3.83E-03	3.07E-03	4.80E-03	261	208	326	303
S. San Andreas—Wrightwood	34.3697	−117.6680	9.43E-03	7.97E-03	1.12E-02	106	90	125	98

*From Appendix H (Biasi, 2013), based on the data compilation in Appendix G (Weldon, Dawson, and Madden, 2013). Comparisons to UCERF2 MRIs are also listed for sites that had data in that study. The 16% and 84% columns represent the 68% confidence bounds for the mean estimates.

(UCERF3.0) was that, in satisfying the above paleoseismic event rates, the inversion would simply put a high (or low) rate of events right at the paleoseismic sites. This produced artificially sharp peaks and troughs in the rate of events along strike. Equation set (3) (Table 6) mitigates this behavior by providing an along-fault smoothing constraint that minimizes curvature in the along-fault rate of events. We apply this smoothing only to fault sections that have one or more paleoseismic event-rate constraints, and confine it to the internal subsections of that section. That is, we do not apply this smoothing beyond the ends of fault sections because this would require additional assumptions and careful bookkeeping at fault branches.

Improbability Constraint (Equation Set 4). Improbability constraints can force a lower rate on any designated event or event type, such as multifault ruptures involving large jumps. Appendix J (Biasi, Parsons, *et al.*, 2013) summarizes the various observational and theoretical studies that can guide the assignment of improbability constraints. However, the Coulomb stress-transfer calculations given in Appendix T

were used to cull the total UCERF3 set down to a subset of ruptures that were deemed viable. Furthermore, the rates of multifault ruptures are already constrained in the inversion by both slip-rate balancing (larger ruptures consume more slip) and by the regional GR constraint (larger events have

Table 9
Sample Values from the Probability of Paleoseismic Detection Model ($P_r^{\text{paleo-event-rate}}$)*

Average Slip (D_r , meters)	Magnitude (Approximate)	Probability of Detection [†]		
		Dist = 0.05	Dist = 0.25	Dist = 0.5
0.08	5.5	0.01	0.02	0.02
0.16	6.0	0.06	0.11	0.14
0.88	6.5	0.53	0.62	0.64
2.04	7.0	0.80	0.82	0.83
3.20	7.5	0.95	0.96	0.97
4.36	8.0	0.98	0.99	0.99

*Values were used in equation set (2) of the inversion, from Appendix I (Weldon and Biasi, 2013).

[†]Dist is fractional distances from end of rupture.

Table 10
Average Slip Data from Appendix R (Madden *et al.*, 2013)*

Fault Section, Subsection Number	Latitude (°) [†]	Longitude (°) [†]	Average Slip (m)	ABM		Geologic		NeoKinema		Zeng	
				Proxy Rate	Proxy MRI	Proxy Rate	Proxy MRI	Proxy Rate	Proxy MRI	Proxy Rate	Proxy MRI
San Andreas (Carrizo) rev, 1	35.24	−119.79	3.52	7.57E-03	132	9.11E-03	110	8.52E-03	117	6.79E-03	147
San Andreas (Carrizo) rev, 5	35.05	−119.56	4.06	6.47E-03	155	7.89E-03	127	7.38E-03	135	5.88E-03	170
San Andreas (Carrizo) rev, 6	35.01	−119.50	4.61	5.66E-03	177	6.95E-03	144	6.50E-03	154	5.18E-03	193
San Andreas (Cholame) rev, 8	35.65	−120.20	2.50	1.06E-02	94	1.28E-02	78	9.47E-03	106	1.02E-02	98
San Andreas (Coachella) rev, 4	33.64	−116.06	2.99	6.12E-03	163	6.29E-03	159	5.16E-03	194	6.21E-03	161
San Andreas (Coachella) rev, 10	33.44	−115.82	3.20	5.73E-03	174	5.89E-03	170	4.83E-03	207	5.82E-03	172
San Andreas (Mojave S), 2	34.64	−118.35	2.87	6.05E-03	165	1.07E-02	94	8.87E-03	113	6.56E-03	152
San Andreas (Mojave S), 3	34.62	−118.28	2.85	6.08E-03	164	1.07E-02	93	8.92E-03	112	6.60E-03	152
Elsinore (Julian), 5	33.24	−116.78	1.12	2.99E-03	334	2.52E-03	396	1.23E-03	815	2.18E-03	458
Garlock (West), 10	35.13	−118.22	4.68	8.66E-04	1155	1.53E-03	654	1.15E-03	873	3.37E-04	2971
Garlock (West), 12	35.20	−118.09	3.46	1.23E-03	813	2.07E-03	484	1.55E-03	646	4.55E-04	2199
Garlock (Central), 15	35.57	−117.15	3.11	1.12E-03	892	2.12E-03	472	1.68E-03	595	2.27E-03	441
San Jacinto (Anza) rev, 1	33.68	−116.82	1.87	4.61E-03	217	7.05E-03	142	5.97E-03	168	6.46E-03	155
San Jacinto (Anza) rev, 5	33.51	−116.55	1.44	5.99E-03	167	9.15E-03	109	7.74E-03	129	8.38E-03	119
San Jacinto (Clark) rev, 0	33.47	−116.48	2.94	1.92E-03	521	2.57E-03	390	1.56E-03	641	1.99E-03	504
San Jacinto (Clark) rev, 1	33.43	−116.41	2.50	2.25E-03	444	3.01E-03	332	1.83E-03	546	2.33E-03	429
San Jacinto (Clark) rev, 4	33.31	−116.21	1.30	2.48E-03	404	3.52E-03	284	3.52E-03	284	4.49E-03	223
Compton, 2	33.97	−118.26	2.80	2.85E-04	3510	3.03E-04	3303	2.89E-04	3456	3.97E-04	2516
Puente Hills, 2	33.91	−118.11	2.77	2.05E-04	4872	3.06E-04	3264	4.02E-04	2485	4.34E-04	2304
Puente Hills, 2	33.91	−118.11	2.93	1.94E-04	5166	2.89E-04	3461	3.80E-04	2634	4.09E-04	2443
San Andreas (Carrizo) rev, 0	35.27	−119.83	5.42	4.91E-03	204	5.91E-03	169	5.53E-03	181	4.40E-03	227
San Andreas (Mojave S), 13	34.37	−117.67	3.15	5.51E-03	181	9.72E-03	103	8.08E-03	124	5.98E-03	167
San Andreas (Mojave S), 9	34.46	−117.89	6.00	2.89E-03	346	5.10E-03	196	4.24E-03	236	3.14E-03	319

*The first 17 rows are from table 5 of Madden *et al.* (2013) (average slip from offset features), and the last 6 rows are from their table 6 (based on paleoseismic trench studies). Also listed are the proxy mean event rates and proxy mean recurrence intervals implied by each deformation model. These sections/subsections correspond to Fault Model 3.1.

[†]Location (latitude, longitude) is approximately half way down the trace of the fault subsection listed in column 1.

lower collective rates), rendering an improbability constraint somewhat redundant. We therefore have not applied any improbability constraints in UCERF3, and this choice is supported by results presented in the [Fits to Data Not Used in the Inversion](#) section.

Other Constraints (Equation Sets 5, 6, and 7). The *a priori* constraint of equation set (5) (Table 6) forces individual ruptures to have specific rates. This constraint is only applied to the Parkfield section, where inversion ruptures that are similar to the historical Parkfield events are constrained to have a collective rate of 0.04 per year, corresponding to the observed recurrence interval of 25 years (Appendix N, Page *et al.*, 2013).

Table 11
Probability of Observing Surface Slip
($p_r^{\text{paleo-slip-proxy}}$)*

Slip (D_{sr} , meters)	Probability of Detection
0.0	0.0
0.25	0.1
≥2.0	0.95

*Probabilities are as given in Appendix R (Madden *et al.*, 2013). Values are linearly interpolated between those listed.

Equation set (6) (Table 6) represents a regional MFD constraint that prevents an overprediction, or bulge, at moderate magnitudes. Its application, however, requires the removal of both subseismogenic ruptures and off-fault seismicity. The details of this, as well as those of the fault section MFD constraints (equation set 7; Table 6), differ between the *Characteristic* and *Gutenberg–Richter* branches and are therefore discussed under the [Inversion Setup and Associated Gridded Seismicity](#) section. The remainder of this section discusses the additional inversion constraints that are common to all branches.

Total Regional Rate of $M \geq 5$ Events. A fundamental parameter and logic-tree branch choice is the total rate of $M \geq 5$ events/yr, denoted $R_{M \geq 5}^{\text{total}}$, that occur within the UCERF3 model region (shown in Fig. 1). The seismicity analysis in Appendix L (Felzer, 2013b) determines seismicity rates using data for the time periods 1850–2011 (historical and instrumental) and 1984–2011 (modern instrumental catalog). We use the UCERF2 catalog completeness thresholds calculated by Felzer (2007) for eight different regions and over a variety of different eras based on changes in data availability with time. One modification is a drop in the 1850–1865 completeness threshold from M 8.0 to 7.4, based on the determination that an $M > 7.4$ earthquake would probably have been felt over a sufficiently wide area to have

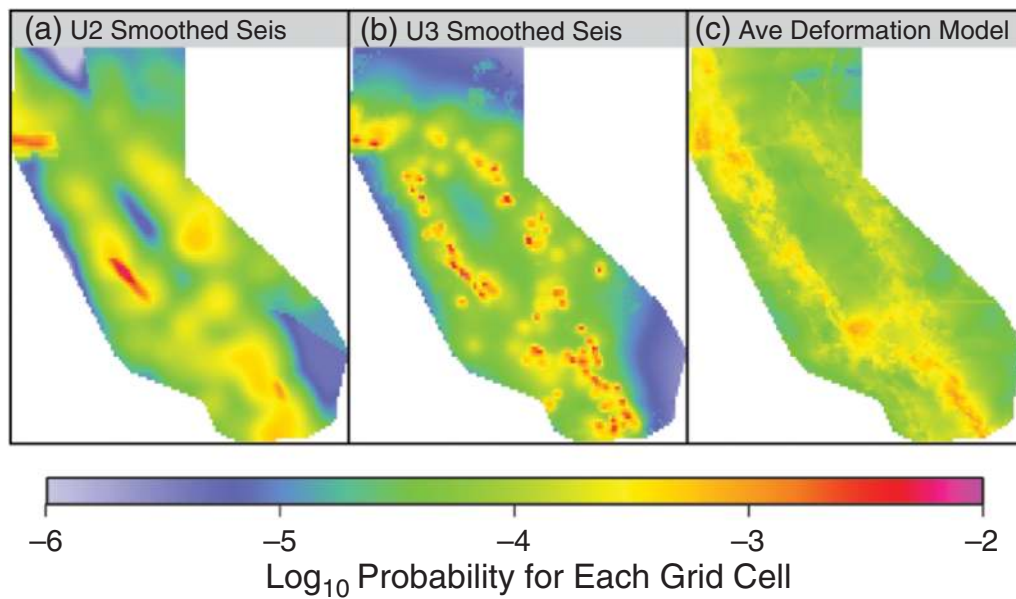


Figure 14. The various off-fault spatial seismicity probability density functions (*SpatialPDF*) used in UCERF3 for setting gridded seismicity (referred to as the *Off-Fault Spatial Seis PDF* logic-tree branch in Fig. 3). Values in each map sum to unity. (a) The UCERF2 smoothed seismicity model. (b) The UCERF3 smoothed seismicity model of [Felzer \(2013c, Appendix M\)](#), which has a higher resolution, adaptive smoothing kernel. (c) Spatial PDF implied by the average of the off-fault moment rate maps from Appendix C ([Parsons *et al.*, 2013](#)), which includes the ABM, NeoKinema, and Zeng deformation models and averages over maps for both Fault Models 3.1 and 3.2.

been noted, despite the sparse population. The lower magnitude cutoff has also been reduced from M 4 in UCERF2 to M 2.5 here, and all rate calculations include the UCERF2 corrections for magnitude uncertainties and rounding errors ([Felzer, 2007](#)).

The rates for each era were averaged together, weighted linearly by era duration. This differs from the [Weichert \(1980\)](#) method applied by the NSHMP and used in the UCERF2 smoothed seismicity model, in which each era is weighted by the number of earthquakes contained. The [Weichert \(1980\)](#) method produces a more accurate result if the underlying rates are the same in each era. However, if the seismicity rate changes with time, as implied by the empirical models of [WGCEP, 2003, 2007](#), the [Weichert \(1980\)](#) method produces a result that is heavily skewed toward the instrumental era. When computing an observed seismicity rate for UCERF2, the Weichert method was applied in three long time periods, and the results from those three time periods were averaged. This somewhat minimizes the effect of the weighting by the number of events in the Weichert method. By using more, smaller time periods in UCERF3, we have completely eliminated the assumptions of constant rate.

The 1850–2011 rate averages for each region were summed to obtain the total regional rate. A new global analog model has also been used to account for possible temporal rate variations, leading to the following branch options for $R_{M \geq 5}^{\text{total}}$: 6.5 events/yr (10% weight), 7.9 events/yr (60% weight), and 9.6 events/yr (30% weight). The preferred value (7.9) is 5% greater than the value of 7.5 given in UCERF2 (see Appendix I, [Felzer, 2007](#)), and the branch-averaged

UCERF3 value (8.3) is 11% greater than the UCERF2 value. In addition to dropping the Weichert method completely, part of this difference comes from five years of additional data and from decreasing the lower magnitude cutoff. Asymmetric weights are used here because the post-1850 era is more likely to be below, rather than above, the true average rate, especially given the lack of any $M \geq 8$ events during this time period.

It is important to note that the UCERF2 observed value of 7.5 was not used as an explicit constraint in that model, with the final implied UCERF2 value ($\sim 5.8 M \geq 5 \geq$ events/yr) being determined primarily by the smoothed seismicity model (UCERF2 Appendix J, [Petersen, Mueller, *et al.*, 2007](#)). Therefore, the gridded seismicity component of UCERF2 is more consistent with recent seismicity rates and thereby effectively includes the empirical time-dependent models of [WGCEP \(2003\)](#) and [\(2007\)](#). We believe the long-term rates are more appropriate for the UCERF3 earthquake rate model, especially because users will be able to apply any empirical model correction that makes it into the forthcoming time-dependent components. As a consequence, the preferred UCERF3 rate (7.9) is 36% greater than the effective UCERF2 model rate (5.8), and the UCERF3 branch-averaged rate (8.3) is 43% greater.

Off-Fault Spatial Seis PDF. The spatial distribution of off-fault gridded seismicity is set by choosing one of the spatial probability density maps shown in Figure 14 (referred to as the *Off-Fault Spatial Seis PDF* logic-tree branch in Figure 3, sometimes abbreviated as *SpatialPDF* here). One option is the UCERF2 smoothed seismicity map (Fig. 14a) from the

UCERF2 Appendix J (Petersen, Mueller, *et al.*, 2007), which is based on the Frankel (1995) methodology. This represents $M \geq 4$ events smoothed using a 2D Gaussian kernel with a sigma of 50 km and a somewhat narrower, anisotropic smoothing near a few active faults.

Another *SpatialPDF* option is the UCERF3 *Smoothed Seis* map shown in Figure 14b, which was developed by Felzer (2013c, Appendix M) using the adaptive smoothing algorithm of Helmstetter *et al.* (2007). Specifically, this considers $M \geq 2.5$ events, and the sigma of a 2D Gaussian smoothing kernel is determined by the distance to the n th closest earthquake, for which $n = 8$ was chosen based on optimization tests given in Appendix M (Felzer, 2013c). Such higher-resolution smoothing has had superior performance in the formal RELM tests (e.g., Zechar *et al.*, 2013) and is more consistent with surveys of precariously balanced rocks (e.g., Brune *et al.*, 2006). Nevertheless, UCERF2 smoothing may be more appropriate for the larger events that dominate hazard ($M > 6$) and/or for the longer-term forecasts of interest for building codes.

A third *SpatialPDF* option is to use the off-fault moment rate map associated with the chosen deformation model (Appendix C, Parsons *et al.*, 2013), which were shown previously in Figure 9, or the average of the three models that provide off-fault estimates (Fig. 14c). The specification of *SpatialPDF* branch weights differs between the *Characteristic* and *Gutenberg–Richter Inversion Model* options (Fig. 3) and will therefore be discussed in the *Inversion Setup and Associated Gridded Seismicity* section.

Fraction of Seismicity On Faults Versus Off Faults. Like previous WGCEP and NSHMP models, the UCERF3 framework explicitly differentiates between fault-based sources and off-fault (gridded) seismicity, starting with the deformation model. The fraction of observed seismicity attributable to on-fault versus off-fault events is implied by both the choice of *SpatialPDF* (Fig. 14) and the fault zone polygons (as a proxy for all events within). Summing the probability density function (PDF) values inside all fault zones implies the following percentage of on-fault seismicity:

- 53% for UCERF2 smoothed seismicity paired with *Fault Model 3.1*,
- 58% for UCERF2 smoothed seismicity paired with *Fault Model 3.2*,
- 53% for UCERF3 smoothed seismicity paired with *Fault Model 3.1*, and
- 59% for UCERF3 smoothed seismicity paired with *Fault Model 3.2*.

None of the deformation models are used to calculate the percentage of on-fault seismicity because doing so requires assuming the MFD at each location, as well as the fraction of moment that is released aseismically, both on and off fault.

Maximum Off-Fault Magnitude ($M_{\max}^{\text{off-fault}}$). Another logic-tree choice is the assumed maximum magnitude of off-fault seismicity, $M_{\max}^{\text{off-fault}}$. The three branch options applied in UCERF3 are 7.3, 7.6, and 7.9, with weights of 10%, 80%, and 10%, respectively (Fig. 3). For UCERF2, $M_{\max}^{\text{off-fault}}$ was spatially variable, being 7.6 in the type C zones and 7.0 for gridded seismicity elsewhere, with a custom reduction near faults to avoid double counting with fault-based sources. As such, $M_{\max}^{\text{off-fault}}$ has increased in UCERF3 for areas away from faults and outside type C zones, driven in part by the 2010 M 7.2 El Mayor–Cucapah earthquake exceeding the UCERF2 background-seismicity value of 7.0 (although whether this event was on or off fault is ambiguous in UCERF2, as noted in the *Fault Zone Polygons* section). Branch weights were based on expert-opinion consensus, with the low weight at M 7.3 being driven by high, implied off-fault aseismicity (when comparing consequent moment rates to the deformation model values in Table 5), and the low weight at M 7.9 reflecting a lack of evidence for such events (even though they are rare). The fact that three $M_{\max}^{\text{off-fault}}$ options are provided is an improvement over UCERF2, which only had a single branch for off-fault seismicity. The particular choices and associated weights adopted here are nevertheless somewhat subjective.

Inversion Setup and Associated Gridded Seismicity

Here we describe the *Characteristic* versus *Gutenberg–Richter* branch options for the *Inversion Model* (Fig. 3), including their conceptual motivation, how the remaining inversion constraints are constructed, and how the gridded seismicity is specified for each option. A supplementary file U3 preinversion analysis table (see *Data and Resources*) lists many of the metrics discussed here for each potential logic-tree branch.

Characteristic Branches. These branches represent the possibility that faulting is governed by “characteristic behavior,” which has come to mean one or more of the following: (1) segmentation of faulting, in which ruptures persistently terminate at certain locations; (2) an increased rate of events at higher magnitudes compared to an extrapolation of the Gutenberg–Richter magnitude–frequency distribution from smaller magnitudes; and (3) a narrow range of slip from event to event at a point on a fault. In principle, these attributes could be implemented as direct constraints in the grand inversion. However, distilling the essence of a characteristic model into independent inversion constraints has proven difficult.

For the UCERF3 model presented here, the *Characteristic* branch is defined by forcing (via equation set 7 from Table 6) each fault subsection to stay as close as possible to an *a priori* characteristic nucleation MFD, in which there is an increased rate of higher magnitude events. For both the new faults and those designated as type B in UCERF2, the total nucleation MFD for each fault section was constructed by putting one-third of the moment rate into a Gutenberg–

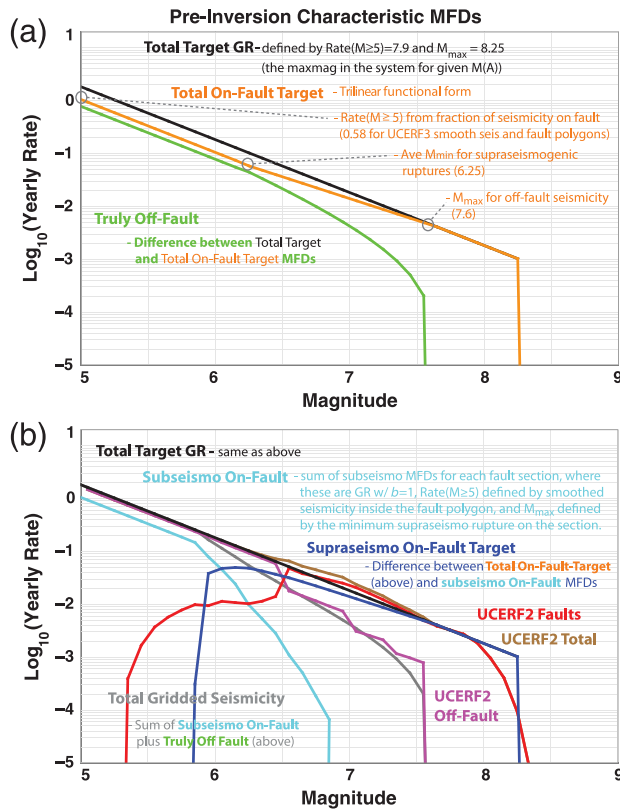


Figure 15. Examples of the various regional magnitude frequency distributions considered in setting up the *Characteristic Inversion Model* branches. See labels and main text for an explanation of each curve. This example is for the reference branch, which is shown with bold elements in Figure 3.

Richter distribution and two-thirds of the moment rate into a characteristic distribution. For the Gutenberg–Richter component, the minimum magnitude was set by the smallest supra-seismogenic rupture on that section (again, defined as having a length equal to the down-dip width); maximum magnitude was set by the total fault section area and the chosen magnitude–area relationship; b -value was set as 1.0 (aftershocks are included); and a -value was set to satisfy one-third of the section slip rate, reduced for subseismogenic ruptures as described in the *Inversion Setup and Associated Gridded Seismicity* section.

The characteristic component is represented with a single magnitude at the Gutenberg–Richter maximum magnitude, with an event rate that satisfies two-thirds of the slip rate (also reduced for subseismogenic ruptures). No aleatory variability in magnitude is given for the characteristic portion, although such variability can be added later for hazard calculations, as was done in UCERF2. The total characteristic nucleation MFD (the sum of both the Gutenberg–Richter and characteristic portions) is generally consistent with past NSHMP models. However, it is not exactly the same as that for type B faults in UCERF2, because the latter had branches for both connecting more type B faults (into mega faults) and for setting b -value to zero on the Gutenberg–Richter portion. These latter

options were introduced in UCERF2 only to mitigate an over-prediction of event rates near M 6.7 (the bulge problem), which is handled directly in the UCERF3 grand inversion.

For fault sections that were designated as type A in UCERF2, the characteristic nucleation MFD constraint is defined as that implied by UCERF2, averaged over all branches. This approach preserves the extra attention given to type A faults in UCERF2. The resultant characteristic nucleation MFD derived for each fault section is then divided evenly among the associated subsections (for use in equation set 7 in Table 6), which provides some along-fault smoothness in event rates along the main fault sections. Depending on the weight assigned to equation set (7), the grand inversion tries to stay as close as possible to these characteristic nucleation MFDs.

For the regional MFD constraint in equation set (6) (Table 6), a target MFD for the entire region is first constructed from the chosen logic-tree branch for total regional rate, $R_{M \geq 5}^{\text{total}}$, and the implied regional maximum magnitude, M_{\max} . The latter is computed from the largest area rupture in the fault system (given the chosen deformation model and magnitude–area relationship). The target MFD is further assumed to be a perfect truncated Gutenberg–Richter distribution with a b -value of 1.0. The latter is based on the state-wide analysis found in Appendix L (Felzer, 2013b), which gives a 98% confidence bound of $0.98 < b\text{-value} < 1.02$. The total target MFD, an example of which is shown as the black curve in Figure 15, is then partitioned into a supra-seismogenic on-fault MFD, for use in the regional MFD constraint of equation set (6) (Table 6), as well as MFDs for the subseismogenic on-fault seismicity and the truly off-fault seismicity.

Because a fault section is a proxy for all ruptures that nucleate within its fault zone polygon, the total rate of events for each fault section is determined by multiplying $R_{M \geq 5}^{\text{total}}$ by the sum of *SpatialPDF* values inside the section's fault zone polygon. Summing these rates over all fault sections gives the total rate of on-fault events (listed in the *Total Regional Rate of $M \geq 5$ Events* section, and illustrated on the left side of orange curve in Fig. 15a). Following UCERF2, the MFD for subseismogenic, on-fault ruptures is assumed to be Gutenberg–Richter up to the minimum magnitude of supra-seismogenic ruptures. In UCERF2, this supra-seismogenic transition was M 6.5, except where the characteristic magnitude was less, whereas in UCERF3 the transition is fault section dependent, owing to variations in seismogenic widths. Below the minimum supra-seismogenic magnitudes, the total on-fault target MFD (orange curve in Fig. 15a) must be parallel to the total target (black curve) and offset by the difference between $R_{M \geq 5}^{\text{total}}$ and the total off-fault rate. Above the maximum magnitude of the off-fault events, $M_{\max}^{(\text{off-fault})}$, the total target on-fault MFD (orange curve) must match the total regional target (black curve). In other words, the total on-fault target MFD has a b -value of 1.0 above and below these two transition points and assumes a straight line interpolation

in between (in log-rate space), meaning a constant, lower b -value at intermediate magnitudes (Fig. 15a).

The truly off-fault MFD (green curve in Fig. 15a) is simply the difference between the total target MFD (black curve) and the total on-fault target MFD (orange curve). The supra-seismogenic, on-fault MFD, shown as the blue line in Figure 15b, is the total on-fault target (orange curve) minus the total subseismogenic on-fault MFD (cyan curve, which represents the sum of all subseismogenic, on-fault MFDs).

The supra-seismogenic, on-fault MFD (blue curve in Fig. 15b) summarizes the total of all regional MFD constraints represented by equation set (6) (Table 6). In principle, this total could be broken into arbitrarily small subregions, but uncertainties on the rates in smaller areas impose practical limits. For UCERF3, the total MFD was divided into just two regional constraints, one for northern and one for southern California. Furthermore, equation set (6) is applied as an equality constraint below M 7.85 and as an inequality constraint at higher magnitudes (Appendix N, Page et al., 2013). The latter allows the final solution MFD to roll off more quickly than the target if allowed or required by the other data constraints.

The total gridded seismicity for UCERF3 (gray line in Fig. 15b) is sum of the off-fault MFD (green) and the total subseismogenic on-fault MFD (cyan). This result is generally consistent with the total UCERF2 gridded seismicity (magenta line in Fig. 15b), though smoother in shape and exhibiting lower rates at some magnitudes (consistent with the added UCERF3 faults taking moment rate from the gridded seismicity). The red line in Figure 15b shows the total MFD for fault-based sources in UCERF2, which by itself exceeds the total regional target around M 7.0—the bulge described in the UCERF2 report—which is eliminated in the grand inversion by imposing the constraints of equation set (6) (Table 6). The brown line in Figure 15b is the total MFD for UCERF2 (which equals magenta plus red).

Up to this point, the deformation-model moment rates (Table 5) have not been used in constructing the various target MFDs. A useful pre-inversion diagnostic is to compute implied coupling coefficients, defined here as the moment rate of the target MFD divided by the deformation model moment rate from Table 5. These diagnostics are listed separately for the total on-fault and off-fault model components, and for all logic-tree branches, in the U3 pre-inversion analysis table (see Data and Resources). These implied coupling coefficients can exceed 1.0 if the target MFD implies more moment rate than exists in the deformation model.

The off-fault coupling coefficients implied for a given deformation model depend primarily on the choice of $R_{M \geq 5}^{\text{total}}$ and $M_{\text{max}}^{(\text{off-fault})}$, and to a lesser extent on the *SpatialPDF*. The values implied from UCERF3 range from 0.17 (for the *NeoKinema* deformation model with $R_{M \geq 5}^{\text{total}} = 7.6$, $M_{\text{max}}^{(\text{off-fault})} = 7.3$, *UCERF3 Smoothed Seis*, and the *Shaw09-mod* magnitude–area relationship) to 0.62 (for *Geologic Deformation Model* with $R_{M \geq 5}^{\text{total}} = 9.6$, $M_{\text{max}}^{(\text{off-fault})} = 7.9$, *UCERF2 Smoothed Seis*, and the *EllsworthB* magnitude–area

relationship); values for all branches are given in the U3 pre-inversion analysis table (see Data and Resources). These coupling coefficients imply off-fault moment rate reductions of 38% to 83% (relative to that predicted by the deformation models). One could alternatively tune $M_{\text{max}}^{(\text{off-fault})}$ to some desired coupling coefficient. However, off-fault coupling coefficients are essentially unconstrained, and the parameterization in terms of $M_{\text{max}}^{(\text{off-fault})}$ is more intuitive for most hazard analysts. The possibility of using the implied off-fault coupling coefficients in deciding *a posteriori* branch weights is not pursued here, although as noted previously, it was a consideration in assigning the lower $M_{\text{max}}^{(\text{off-fault})}$ value of 7.3 a relatively small weight (10%).

The on-fault coupling coefficients implied by the deformation models are more potentially useful to modify the model. Values greater than 1.0 are remedied by the inversion rolling off the final MFD more rapidly at highest magnitudes relative to the target. Values less than 1.0 imply the slip rates are higher than can be accommodated by the target MFD, and the UCERF3 logic tree consequently has four *Fault Moment Rate Fix* options for this:

- *Apply Implied Coupling Coefficient* reduces the slip rates on all fault sections by the implied coupling coefficient.
- *Relax MFD Constraint* permits an overprediction bulge in the final MFD if needed to satisfy slip rates.
- *Apply Both Options* applies both of the preceding options.
- *Do Nothing* lets the inversion decide where to reduce slip rates in matching the target MFD.

For UCERF3, only the *Do Nothing* option is given nonzero weight, because fault moment rate reductions are not an important issue for the characteristic models (the majority of implied on-fault coupling coefficient values are greater than 1.0, with the lowest being 0.86; see the U3 pre-inversion analysis table in Data and Resources). This means the inversion will decide whether and where to reduce slip rates (balancing this against the other constraints in the inversion). An alternative approach might be to target specific faults with site-specific coupling coefficients. Indeed, the exclusion of the Mendocino, Cerro Prieto, and Brawley faults from previous NSHMP models was apparently done for this reason. However, we presently lack any basis for applying fault-specific coupling coefficients (beyond those already applied), and we want to avoid excluding any major faults from consideration.

The *Relax MFD Constraint* might still be appealing in order to relax the regional GR constraint (because there is some chance the UCERF2 bulge is real, even though there is no supporting evidence for it). The result of doing so, however, is quite consistent with keeping the GR constraint but applying the highest branch option for $R_{M \geq 5}^{\text{total}}$ (9.6 events/yr); that is, the *Relax MFD Constraint* tends to increase rates at all magnitudes equally (Appendix N, Page et al., 2013), so we effectively have this option in the model.

The logic tree in Figure 3 gives the following two branches for the characteristic *Inversion Model*:

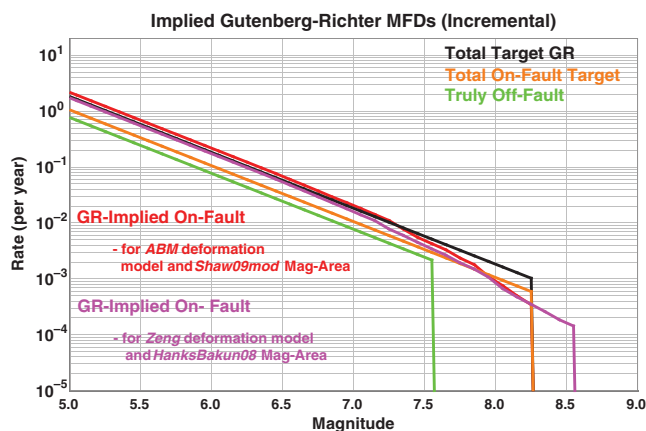


Figure 16. Magnitude–frequency distributions implied by the Gutenberg–Richter (GR) hypothesis. Total target GR (black line) satisfies the total regional rate (7.9 events/yr for UCERF3) and the M_{\max} implied by the largest event in the fault system (8.25 for the *Shaw09mod* magnitude–area relationship here). The total on-fault target (orange line) is the total target GR multiplied by the fraction of on-fault seismicity (58% here), and the truly off-fault (green line) MFD is the total target minus the total on-fault target, and then truncated at $M_{\max}^{\text{off-fault}} = M7.6$. The GR-implied on-fault curves (red and magenta lines) represent the MFDs implied by the GR hypothesis for two extreme branches (and with no off-fault seismicity being added), both of which fall well above the total on-fault target; results for all other GR branches with $R_{M \geq 5}^{\text{total}} = 7.6$ fall between these end members. The GR-implied curves roll off at the highest magnitudes because not all fault sections participate in the largest events.

- *Characteristic UCERF2 Constrained:* This applies the fault section nucleation MFD constraints described for equation set (7). Note that in an effort to avoid saying that any event cannot happen, rupture rates are prevented from going to zero by enforcing a minimum “water-level” rate, which is the rupture rate for a GR starting model multiplied by 0.01 (see Appendix N, [Page et al., 2013](#)).
- *Characteristic Unconstrained:* No fault section MFD constraints are applied here. This model is more underdetermined, so a larger set of inversion runs are needed to sample the solution space. Results can either be averaged or used to sprout additional subbranches of the logic tree.

Currently only the first of these options is given nonzero weight for two reasons: (1) to stay as close as possible to UCERF2, and (2) because the second option requires much more extensive exploration of the solution space, which we did not have time to conduct.

The fault slip rates are reduced in the inversion according to the moment rate implied by subseismogenic, on-fault ruptures. This reduction was originally done on a fault section basis, but high rates of observed seismicity in some areas produced subseismogenic MFDs that had moment rates greater than those assigned to the fault section, leading to negative corrected moments. Therefore, only a system-wide average is applied to reduce slip rates for subseismogenic ruptures in UCERF3. The reduction for each logic-tree

branch is derived by dividing the moment rate of the subseismogenic MFD (cyan curve in Fig. 15b) by the total on-fault moment rate from the deformation model (Table 5); the values among branches here vary from 4.1% to 10% (U3 pre-inversion analysis table in [Data and Resources](#)).

The off-fault gridded seismicity sources are defined by partitioning the associated MFD (green curve in Fig. 15a) among the regional grid cells that are outside fault zone polygons, weighted by the relative *SpatialPDF* value in each grid cell. The *Characteristic* branches use either the *UCERF2* or *UCERF3 Smoothed Seis* model (Fig. 14a or Fig. 14b), with equal weight being given to each. While there was some preference for the *UCERF3 Smoothed Seis* model, for reasons discussed in the *Off-Fault Spatial Seis PDF* section, preliminary hazard calculations showed it to imply significant hazard changes (discussed in the [Results](#) section). Given the remaining uncertainties on which smoothed seismicity map is most applicable for large damaging events in a long-term model, we ended up giving each equal weight. While there was also interest in applying the deformation model–based *SpatialPDF* options (model-specific maps shown in Fig. 9, or the average shown in Fig. 14c), we did not have time to do so.

The subseismogenic MFD for each fault section is distributed among the grid cells that fall within the associated fault zone polygon, consistent with the smoothed seismicity rates used to derive the subseismogenic MFDs. Given the *ad hoc* choices used to construct fault zone polygons (Fig. 4), the hazard implications of this methodology need to be understood. The primary influence of fault zone width is on the maximum magnitude for gridded seismicity near faults. Inside the polygons, this maximum magnitude is defined by the minimum magnitude of supra-seismogenic on-fault ruptures (6.3 on average), whereas outside the polygons it is specified by $M_{\max}^{\text{(off-fault)}}$, with UCERF3 logic-tree options of 7.3, 7.6, or 7.9. Therefore, changing the fault zone widths primarily changes the gridded seismicity maximum magnitudes near the outer edges of the polygon, which should have only a very small effect on UCERF3 hazard estimates because the hazard near faults is generally dominated by supra-seismogenic, on-fault ruptures.

Gutenberg–Richter Branches. These branches represent the possibility that earthquakes on individual faults are governed by a Gutenberg–Richter magnitude–frequency distribution. This GR hypothesis conflicts with all previous WGCEP and NSHMP models, which assumed that ruptures on large, well-developed faults exhibit characteristic behavior. Imposing GR behavior on faults in the UCERF2 framework exacerbates the MFD bulge near $M 6.7$, whereas the UCERF3 grand inversion reduces this problem by allowing multifault ruptures. Given the support the GR hypothesis has received in recent analyses (e.g., [Parsons and Geist, 2009](#)), we tried to accommodate such a branch on the UCERF3 logic tree.

The target MFDs for the GR case are simple to construct (Fig. 16). The total regional target (black line in Fig. 16) is again specified by the choice of $R_{M \geq 5}^{\text{total}}$ and M_{\max} and is

partitioned according to the fraction of seismicity that is on fault (e.g., 58% for UCERF3 smoothing), yielding the orange on-fault target MFD shown in Figure 16. The off-fault MFD (green line) is the difference truncated at the specified value of $M_{\max}^{(\text{off-fault})}$.

The GR hypothesis states that each fault section nucleates a GR distribution of earthquakes, with a b -value of 1.0 and a maximum magnitude defined by the largest rupture in which the section participates, including multifault ruptures. The rate of events, or the GR a -value, for each fault section can then be found by satisfying the section moment rate. Even before any inversion, we can sum all the consequent fault section MFDs to obtain a total GR-implied on-fault MFD. Two examples are shown in Figure 16. The red curve, which represents the *ABM Deformation Model* paired with the *Shaw09mod* magnitude–area relationship (equation 3), exceeds not only the on-fault target (orange), but also the total regional target (black). The magenta curve, which represents the *Zeng Deformation Model* paired with the *HanksBakun08* magnitude–area relationship (equation 1), is just below the total target and well above the on-fault target. Results for all other GR branches fall between these two cases.

This discrepancy can be quantified as an on-fault coupling coefficient, defined as the ratio of the total rate of the target on-fault MFD (orange in Fig. 16) to the total rate of the GR-implied on-fault MFD (red or magenta curve in Fig. 16). The implied coupling coefficients, listed in the U3 pre-inversion analysis table (see [Data and Resources](#)), range from 0.37 to 0.75 among all the GR branches in Figure 3 (slip rate reductions of 63% to 25%). One option for matching the target MFDs is to apply these implied coupling coefficients, which can be done via two of the *Fault Moment Rate Fix* options in the UCERF3 logic tree (Fig. 3):

- *Apply Implied Coupling Coefficient* reduces the slip rates on all fault sections by the implied coupling coefficient (same reduction on all faults).
- *Do Nothing* lets the inversion decide where to reduce slip rates in matching the target MFD.

The other two *Fault Moment Rate Fix* options listed in Figure 3, which include relaxing the regional MFD constraint altogether, cannot be applied because both violate the GR hypothesis.

Not all fault sections participate in the largest event, causing the on-fault GR MFDs to roll off at high magnitudes (red and magenta curves in Fig. 16). Hence, more moment has to be taken up by smaller earthquakes, which increases overall rate of events. The discrepancy would be reduced if all sections shared the same maximum magnitude, but this would require including many of the ruptures filtered out by our plausibility criteria or adding many more faults throughout the region to increase connectivity (which would add moment as well).

There is some evidence that faults might have a lower b -value than surrounding regions ([Page et al., 2011](#)). Assuming $b = 0.95$ on faults reduces the discrepancy a little, but

not enough to satisfy regional rates. The definition of fault zone polygons also has some influence in terms of the target on-fault rate, such that increasing their collective area would lessen the discrepancy. However, reasonable adjustments are not adequate. In fact, Figure 16 implies that the fault zone polygons would have to encompass the entire region (because the red and magenta curves essentially match the total target). Doing so would also worsen existing problems with the implied off-fault coupling coefficients (U3 pre-inversion analysis table in [Data and Resources](#)).

Other possible explanations are that the true total regional rate ($R_{M \geq 5}^{\text{total}}$) is significantly higher than our existing branch options, that shear rigidity is considerably less than that assumed (3.0×10^{10} Pa), or some combination of the possibilities discussed here. Any one of these GR corrections would have significant implications. For example, applying the implied coupling coefficients of 0.37 to 0.75 would reduce fault-based hazard by about 25% to 63%, whereas increasing the total regional rate would increase hazard by a similar amount.

An alternative is that the hypothesis is wrong; faults do not honor a GR nucleation MFD. In fact, this may be one of the most important UCERF3 findings. Either way, these branches would get very low relative weight given the extraordinary corrections needed to satisfy all data, leading us to abandon further pursuit for UCERF3, which was the advice of our SRP as well. Further details are therefore not provided here, although these branches remain fully implemented for those wishing to explore viability and/or practical implications further.

Gardner–Knopoff Aftershock Filter

The UCERF3 earthquake rate model includes aftershocks, whereas previous NSHMP models have removed such events using the Gardner–Knopoff declustering algorithm ([Gardner and Knopoff, 1974](#)). The definition of aftershocks implied by this type of declustering is out of date. For example, it implies that the fraction of aftershocks relative to mainshocks is magnitude dependent, whereas recent aftershock studies do not support such dependence (e.g., [Felzer et al., 2004](#)).

Nevertheless, the Gardner–Knopoff definition is still used in formulating and applying hazard policies (e.g., in current building codes that rely on the NSHMP models). To facilitate comparison and consistency with other earthquake hazard models, a procedure for removing Gardner–Knopoff aftershocks has been implemented in the UCERF3 framework.

Gardner–Knopoff declustering typically reduces the b -value from about 1.0 (full catalog) to about 0.8 (declustered catalog). For this reason, the NSHMP has generally used a b -value of 0.8 for modeling smaller events as gridded seismicity. The b -value difference can be combined with the fraction of $M \geq 5$ events designated as mainshocks by the declustering model to construct a Gardner–Knopoff filter. According to UCERF2 Appendix I ([Felzer, 2007](#)), the total number of $M \geq 5$ events per year in the UCERF region is 7.50 for the full catalog, compared with 4.17 for a Gardner–Knopoff de-

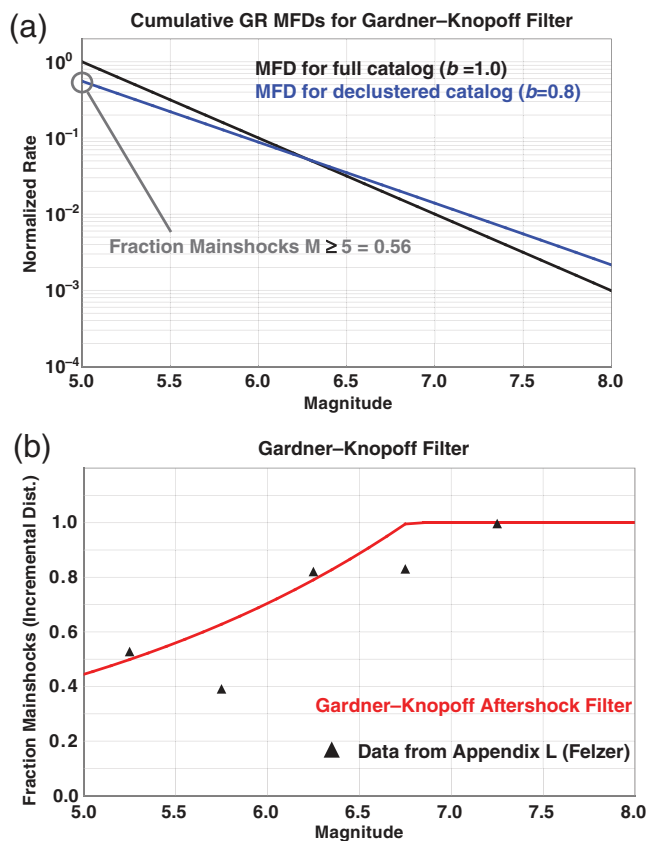


Figure 17. The Gardner–Knopoff aftershock filter. (a) A full-catalog cumulative MFD (black line, with b -value = 1.0 and normalized by the total rate of $M \geq 5$ events), together with the cumulative MFD implied by the Gardner–Knopoff aftershock declustering algorithm described in the text (blue line, with b -value = 0.8 and a relative total rate of 0.56, meaning 56% of $M \geq 5$ events are mainshocks according to this algorithm). (b) The UCERF3 Gardner–Knopoff aftershock filter (red curve), obtained by taking the ratio of incremental versions of the MFDs in (a) (blue divided by black) and capping values above 1.0 at 1.0 (above the crossover magnitude, which is M 6.8 for the incremental distributions). Also shown are data from table 16, Appendix L (Felzer, 2013b; black triangles).

clustered catalog, which implies that 56% of these events are Gardner–Knopoff mainshocks. The corresponding GR MFDs for both full and declustered catalogs are compared in Figure 17a. The UCERF3 Gardner–Knopoff aftershock filter is simply the ratio of the declustered MFD to total MFD in Figure 17a, capped at 1.0 above the point where the two MFDs crossover. This filter compares well with binned data values from table 16 in Appendix L (Felzer, 2013b), as shown here in Figure 17b.

In applying this Gardner–Knopoff aftershock filter, the rate of each UCERF3 rupture can be scaled by the value on the red curve in Figure 17b. This implicitly assumes that the fraction of aftershocks is location independent, which is consistent with past NSHMP applications. Observational evidence for a systematic spatial dependence is lacking, though the available data do not exclude that possibility.

From a practical perspective, our approach is the same as applied in UCERF2 for gridded sources. For fault-based sources, however, the two applications are a bit different. In UCERF2, all fault-based sources were effectively reduced by 3% to account for aftershocks (independent of magnitude), whereas the fractional reduction is magnitude dependent using the Gardner–Knopoff filter. Below M 6.7 (at which our filter has an $\sim 3\%$ reduction), the new methodology reduces rates more than in UCERF2, and above M 6.7 the new reduction is less (and zero above M 6.75). While these differences are generally quite small compared to other epistemic uncertainties in the model, there are situations in which the differences may require further consideration. For example, about 30% of $M \sim 6$ Parkfield earthquakes are aftershocks according to this new filter.

To ensure maximum consistency with UCERF2 and past NSHMP practice, the Gardner–Knopoff filter defined here is applied only to gridded-seismicity sources, whereas the rates of all supra-seismogenic ruptures are reduced by 3% (again, the latter being the UCERF2 value). This means the Gardner–Knopoff filter is not applied for supra-seismogenic ruptures.

Results

This section presents UCERF3 results, postponing important sensitivity tests to a later section (see [Sensitivity Tests](#)), both because those tests depend on evaluation metrics introduced here and because interpretations here are not influenced by the test results.

Model Evaluation Challenges

One of the primary challenges in evaluating UCERF3 is the increased number of viable ruptures in the fault system—more than 250,000, compared to less than 8000 mapped into our fault system by UCERF2. Furthermore, the rupture rates in UCERF2 were largely prescribed in terms of rupture extents and assumed MFDs, whereas these properties are derived in UCERF3 from the system-level inversion. Interpretation of UCERF3 results is therefore much more challenging. For example, a five-second visual examination of each UCERF3 rupture would take about 350 hours for just one of the 1440 alternative logic-tree branches. We therefore have to rely on aggregate evaluation metrics.

The grand inversion approach to UCERF3 would not be feasible without access to supercomputers. In addition to the large number of ruptures in each model, we also have to contend with a large number of alternative logic-tree branches (1440). Each simulated annealing run takes about five hours on a typical desktop computer (Appendix N, [Page et al., 2013](#)). Furthermore, simulated annealing finds the optimum solution by sampling the solution space somewhat randomly (using a so-called “smart” Monte Carlo procedure based on thermodynamics). For an overdetermined problem, it is guaranteed to find the global minimum if given infinite time (Granville et al., 1994). Our computation time is limited, however,

Table 12
Evaluation Metrics Currently Available in the UCERF3
Framework

Inversion Data Fits	Regional MFD plots Slip-rate plots (and misfits) Paleoevent rate plots (and misfits) Tabulation of equation-set residuals and pre-inversion metrics
Other Data Fits	Simulated annealing run diagnostics Event correlation between paleoseismic sites Fault jumping statistics Variability of average slip per event at points on faults (slip coefficient of variance, or slip COV) Frequency of different rupture lengths statistics
General Implications	Parent-section MFDs (also tabulated) Subregion MFDs (e.g., LA and SF boxes in Fig. 1) Participation rate maps Maps showing how often other fault sections participate with a particular section Implied segmentation (e.g., on SAF)
Hazard/Loss Metrics	Hazard curves at sites Tornado diagrams (showing which logic-tree branches are influential) Hazard maps (and their ratios to UCERF2) Risk-targeted ground-motion (RTGM) at sites (Luco <i>et al.</i> , 2007) Statewide loss estimates (e.g., Porter <i>et al.</i> , 2012)
3D Visualizations	

so it is important to quantify the convergence properties by examining the spread of results from repeated runs of the same problem. Multiple runs are also needed to sample underdetermined parts of the solution space. Such convergence properties, as well as the influence of alternative equation-set weights, are summarized in the [Sensitivity Tests](#) section, and some are discussed in more detail in Appendix N (Page *et al.*, 2013). For the results presented here, we ran 10 separate simulated annealing inversions for each branch, which will be shown to be more than adequate in terms of quantifying hazard. Multiplying 1440 logic-tree branches by 10 runs per branch and then by five hours of computation time for each run, implies about 72,000 hours of total computation time (8.2 years). Consequently, most of the results presented here were computed on the Stampede cluster at the University of Texas, which can accommodate as many as 6144 separate inversion runs at a time. We have also made extensive use of the cluster at the Center for High-Performance Computing and Communication, University of Southern California, which can accommodate up to 60 inversions at a time.

Dealing with the large numbers of ruptures and logic-tree branches has also necessitated the development of new evaluation metrics and visualization tools. Those currently available are listed in Table 12, most of which are exemplified here, with most others being used in the appendices.

Given the many differences between UCERF2 and UCERF3, a full, step-by-step accounting of the influence of each is infeasible, especially for every site of potential interest and for every evaluation metric. Therefore, our aims here are to identify and explain important differences with respect to UCERF2 and to characterize the influence of different UCERF3 logic-tree branches as best we can.

Preliminary models (e.g., UCERF3.0) included grand inversion results that used UCERF2 ingredients only (same deformation models, scaling relationships, etc.), with the hope that this would indicate where differences are strictly methodological. However, this analysis did not reveal anything unique compared to using new ingredients, so we do not present such results here.

Model Fits to Data

Here we summarize how well final models fit the various data constraints; Appendix N (Page *et al.*, 2013) has further details.

Regional MFDs. Figure 18 compares the envelope of the UCERF3 branch MFDs with the mean MFDs for UCERF2 for the entire California region. The inversion successfully eliminates the apparent UCERF2 overprediction near M 6.5. We also illustrate what happens if the UCERF2-like MFDs are applied strictly to all faults in UCERF3 (orange curve, obtained by giving equations set 7 [Table 6] infinite weight). In this case, the overprediction is even greater than in UCERF2, mostly due to the addition of new fault sections. Appendix N (Page *et al.*, 2013) shows that the final MFDs for a given branch match the associated pre-inversion targets very well. Table 13 lists the cumulative MFDs for both UCERF3 and UCERF2, averaged over all branches and including aftershocks. As expected, the rates have increased by $\sim 42\%$ for $M \geq 5$, decreased by $\sim 23\%$ at $M \geq 6.7$, and increased by $\sim 37\%$ for $M \geq 8$.

Slip Rates. The final slip-rate misfits (solution over target, branch-averaged) are listed for each fault section in the “*Ave-SolSlipRates*” sheet of the U3 Fault Section Data file (see [Data and Resources](#)), Figure 19 shows these misfits for *FM 3.1*, together with an equivalent plot for UCERF2. In general, the UCERF3 fits are better than for UCERF2, which tends to overpredict slip rates near the centers of fault sections and underpredict those near the ends. This is caused by the UCERF2 floating ruptures being given a uniform probability along strike and partly by the tapered-slip distribution.

There are two prominent overprediction (red) outliers for UCERF3 (Fig. 19). The southernmost represents the Elsinore–Glen Ivy fault section. Here the solution slip rate is pulled above the target, by a factor of 1.54, in fitting the paleoseismic event rate constraint on this section (Table 8), which is underpredicted by a factor of 0.73; improving the match to one worsens the fit to the other, illustrating data inconsistency. The other red outlier (Fig. 19), in central

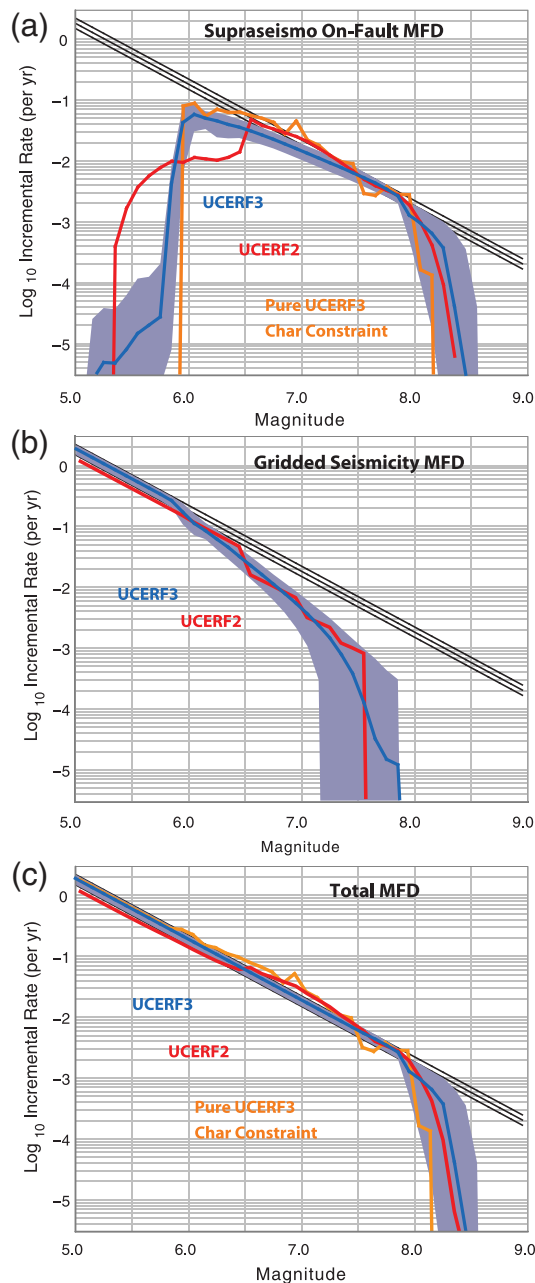


Figure 18. Magnitude–frequency distributions for the entire California region for all UCERF3 logic-tree branches, with comparison to mean results from UCERF2. (a) Supra-seismogenic on-fault MFDs for UCERF3 are shown in blue, with the minimum and maximum among all branches being represented by the shaded region. The average result from UCERF2 is shown in red for comparison. (b) Same as (a), but for gridded seismicity (subseismogenic on-fault ruptures plus truly off-fault sources). (c) Total MFDs, representing the sum of the MFDs in (a) and (b). The black lines in all plots represent reference Gutenberg–Richter distributions for the alternative values of the *Total* $M \geq 5$ Event Rate. Also shown with orange in (a) and (c) are UCERF3 MFDs obtained by applying the fault section MFD constraint (equation set 7 in Table 6) with infinite weight, which reveals the overprediction of regional rates when one assumes UCERF2-like MFDs for each fault. Note that the gridded seismicity MFDs for UCERF2 have had aftershocks added back in by reversing the Gardner–Knopoff filter described in the text.

California, is in the center of the Creeping section of the San Andreas fault (SAF), where the mean slip rate is reduced by 80% to 5 mm/yr to account for creep. The inversion is unable to match this rapid slip-rate change, giving a high value of 10 mm/yr. All other UCERF3 slip rate overpredictions are within 20% of the targets, and virtually all those greater than 10% can be explained by fitting relatively high palaeoseismic event rates.

Overall, UCERF3 underpredicts slip rates more than it overpredicts them, particularly in southern California (where many faults are slightly blue in Fig. 19). On average, total on-fault solution moment rates are 4% below the targets, primarily due to limitations on total event rates by the regional MFD constraint. Although some fault sections have slip-rate reductions of as much as a factor of 2, all can be explained by either the paleoseismic rate constraint being incompatible with the slip-rate constraint (e.g., the Whittier alt 1 fault section) or by the regional MFD constraint coupled with a lack of fault connectivity needed to produce larger events (e.g., the Santa Susana East [connector] fault section). Only six fault sections have final branch-averaged slip rates that fall outside the range defined by the alternative deformation models, and all of these cases fall within the *Geologic* bounds.

Paleoevent Rate Data. UCERF3 paleoseismic event rate misfits are listed in the U3 Fault Section Data file (in the sheets labeled “PaleoEventRateFits” and “ProxyEventRateFits”; see [Data and Resources](#)). Results for paleoseismic sites along the SAF are compared with UCERF2 results in Figure 20 with slip rate fits, to clarify why rates vary along strike. All UCERF3 data fit well, given the uncertainties, and generally fit better than in UCERF2.

Misfits on the North Coast, Santa Cruz, Big Bend, and Mojave North sections of the San Andreas fault are dominated by inconsistencies between paleoevent rate and slip-rate constraints. The average slip-rate discrepancy for Parkfield, which reflects the *a priori* constraint on the 25-year recurrence interval of historical $\sim M$ 6 events, is at odds with other inversion constraints, possibly as a result of deficiencies in modeling the aseismic processes on this fault.

Average slip rates on the Cholame, Carrizo, and Coachella sections are underpredicted. Paleoseismic event rates are also underpredicted on the latter two, which raises the question of why the inversion does not simply add more events to satisfy these data. As a result of the regional MFD constraint, adding earthquakes there requires subtracting such events from other areas, which degrades the slip-rate fits. Both slip rates and event rates can be fit well on these sections if the MFD constraint is removed altogether, but this leads to a significant overprediction of the regional event rates near M 7.

Removing the MFD constraint also puts a high rate of smaller events at the northern end of the Cholame section. These events fill in the precipitous drop in modeled slip rates toward the north (Fig. 20), as required by the Parkfield *a priori* constraint (Appendix N, [Page et al., 2013](#)). This issue is

Table 13
Average Cumulative Magnitude–Frequency Distributions for UCERF3 and UCERF2*

Magnitude	UCERF3			UCERF2			U3/U2 Total Ratio
	Total	Faults	Gridded	Total	Faults	Gridded	
5.0	8.26E+00	4.59E-01	7.80E+00	5.80E+00	3.53E-01	5.45E+00	1.42
5.1	6.56E+00	4.59E-01	6.10E+00	4.66E+00	3.53E-01	4.31E+00	1.41
5.2	5.21E+00	4.59E-01	4.75E+00	3.76E+00	3.53E-01	3.41E+00	1.39
5.3	4.14E+00	4.59E-01	3.68E+00	3.04E+00	3.53E-01	2.69E+00	1.36
5.4	3.28E+00	4.59E-01	2.83E+00	2.46E+00	3.53E-01	2.11E+00	1.33
5.5	2.61E+00	4.59E-01	2.15E+00	2.01E+00	3.51E-01	1.66E+00	1.30
5.6	2.07E+00	4.59E-01	1.61E+00	1.64E+00	3.48E-01	1.29E+00	1.26
5.7	1.64E+00	4.59E-01	1.18E+00	1.34E+00	3.42E-01	1.00E+00	1.22
5.8	1.30E+00	4.58E-01	8.45E-01	1.10E+00	3.34E-01	7.71E-01	1.18
5.9	1.03E+00	4.54E-01	5.80E-01	9.11E-01	3.24E-01	5.87E-01	1.14
6.0	8.20E-01	4.12E-01	4.08E-01	7.55E-01	3.15E-01	4.40E-01	1.09
6.1	6.50E-01	3.54E-01	2.96E-01	6.31E-01	3.03E-01	3.27E-01	1.03
6.2	5.15E-01	3.03E-01	2.12E-01	5.30E-01	2.93E-01	2.37E-01	0.97
6.3	4.08E-01	2.58E-01	1.50E-01	4.48E-01	2.82E-01	1.65E-01	0.91
6.4	3.22E-01	2.18E-01	1.04E-01	3.79E-01	2.71E-01	1.08E-01	0.85
6.5	2.55E-01	1.82E-01	7.23E-02	3.20E-01	2.57E-01	6.30E-02	0.80
6.6	2.01E-01	1.51E-01	4.96E-02	2.56E-01	2.09E-01	4.76E-02	0.78
6.7	1.58E-01	1.25E-01	3.35E-02	2.06E-01	1.71E-01	3.52E-02	0.77
6.8	1.24E-01	1.02E-01	2.22E-02	1.62E-01	1.37E-01	2.51E-02	0.76
6.9	9.72E-02	8.29E-02	1.43E-02	1.26E-01	1.08E-01	1.71E-02	0.77
7.0	7.58E-02	6.69E-02	8.86E-03	9.40E-02	8.34E-02	1.06E-02	0.81
7.1	5.88E-02	5.36E-02	5.19E-03	7.02E-02	6.26E-02	7.56E-03	0.84
7.2	4.53E-02	4.25E-02	2.82E-03	5.16E-02	4.66E-02	5.03E-03	0.88
7.3	3.46E-02	3.32E-02	1.36E-03	3.72E-02	3.43E-02	2.92E-03	0.93
7.4	2.60E-02	2.54E-02	5.71E-04	2.68E-02	2.51E-02	1.75E-03	0.97
7.5	1.92E-02	1.90E-02	1.87E-04	1.90E-02	1.82E-02	7.87E-04	1.01
7.6	1.38E-02	1.37E-02	5.94E-05	1.32E-02	1.32E-02	0.00E+00	1.04
7.7	9.43E-03	9.40E-03	2.71E-05	9.35E-03	9.35E-03	0.00E+00	1.01
7.8	5.97E-03	5.95E-03	1.21E-05	6.08E-03	6.08E-03	0.00E+00	0.98
7.9	3.30E-03	3.30E-03	0.00E+00	3.35E-03	3.35E-03	0.00E+00	0.98
8.0	2.01E-03	2.01E-03	0.00E+00	1.47E-03	1.47E-03	0.00E+00	1.37
8.1	1.07E-03	1.07E-03	0.00E+00	5.09E-04	5.09E-04	0.00E+00	2.09
8.2	4.20E-04	4.20E-04	0.00E+00	9.99E-05	9.99E-05	0.00E+00	4.21
8.3	4.55E-05	4.55E-05	0.00E+00	7.26E-06	7.26E-06	0.00E+00	6.27
8.4	4.68E-06	4.68E-06	0.00E+00	1.08E-06	1.08E-06	0.00E+00	4.34
8.5	1.56E-06	1.56E-06	0.00E+00	0.00E+00	0.00E+00	0.00E+00	Inf

*“Faults” refers to supra-seismogenic on-fault ruptures; “Gridded” refers to the gridded seismicity, and “Total” includes both; each rate is given in events per year. “U3/U2 Total Ratio” is the ratio of total values from UCERF3 and UCERF2. These rates include aftershocks, where those for the UCERF2 gridded seismicity were added using the Gardner–Knopoff filter described in the text. UCERF2 on-fault values include aleatory variability of magnitude for a given rupture area, whereas values for UCERF3 do not.

also apparent in the UCERF2 results. From a hazard perspective, it is more important to get the total rate of events correct than to satisfy slip rates exactly, so we kept the regional MFD constraint to prevent the inflation of total event rates.

UCERF3 event rates on the southern SAF average about 25% below our best paleoseismic estimates (Table 8). The worst case is Carrizo, where the mean model rate (an observable paleoevent every 193 years) is 40% below the best paleo-rate estimate (one every 115 years). In UCERF2, the average paleoconstraint for Carrizo was an event every 225 years (Fig. 20), so the paleoestimate has been revised by almost a factor of 2. The average UCERF3 model rate is relatively consistent with the UCERF2 model average (one every 193 year versus one every 185 years, respectively);

therefore, the hazard change in UCERF3 is minimal. Hazard-ratio maps, presented in the [Hazard Curves and Maps](#) section, will show that this is generally true of the entire SAF.

The misfits on the southern SAF nevertheless point to some possible inconsistencies that we should strive to understand and resolve in the future. Until we do so, however, minimizing changes with respect to UCERF2 is appropriate, especially since matching the paleoseismic data better will increase hazard. Nevertheless, the uncertainties reflected in Figure 20 indicate general agreement, as well as the existence of some UCERF3 branches that do fit the southern SAF data better (meaning these branches could be given higher weight if users could justify doing so).

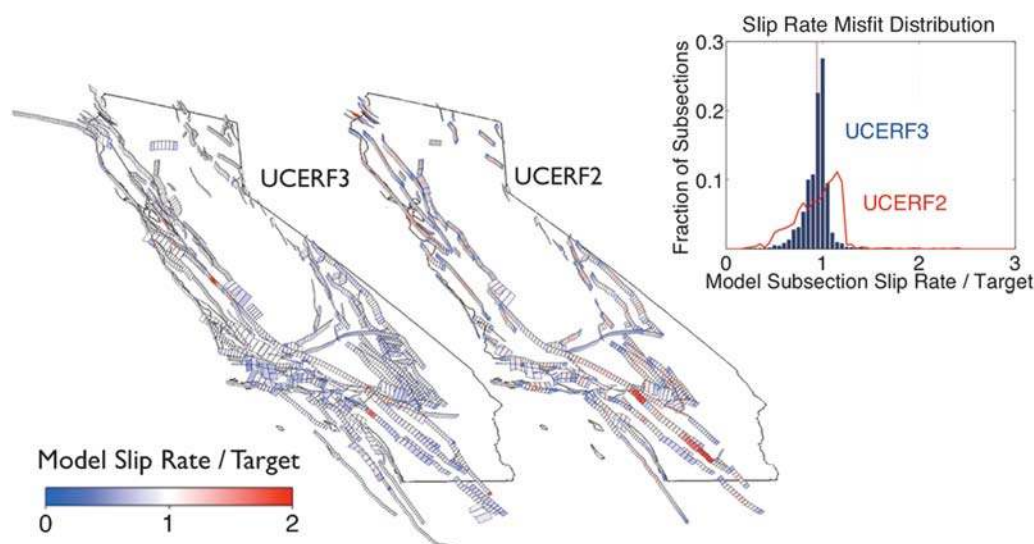


Figure 19. Average subsection slip rate misfits for both UCERF3 (*Fault Model 3.1*) and UCERF2 (relative to UCERF2 slip rates), shown as ratios of final implied slip rates divided by deformation model slip rates (reduced by coupling coefficient) and averaged over all logic-tree branches. Equivalent plots for each deformation model (branch subsets) are given in Appendix N (Page *et al.*, 2013). The distribution of subsection slip-rate misfits is shown for UCERF2 and UCERF3 at the upper right, with the means plotted as vertical dashed lines (0.95 and 0.94 for UCERF2 and UCERF3, respectively) and with standard deviations of 0.24 for UCERF2 and 0.13 for UCERF3.

None of the UCERF3 model rates at the 31 paleoseismic sites are outside of the 95% confidence bounds on the data, and the reduced chi-squared value for the UCERF3 event rate fit is 0.72, indicating that, on the whole, UCERF3 overfits the paleoseismic event rate data (Appendix N, Page *et al.*, 2013). Although the model systematically underpredicts event rates on the southern SAF, these sites do not represent independent data because the sites are seeing the same period of time and many of the same events. UCERF2 rates, for comparison, are outside of the (UCERF3) 95% confidence bounds at five of the sites.

Plots like Figure 20 are available for all the faults that have paleoseismic constraints (see Paleoseismic Data Fits under U3 Supplementary Figures in [Data and Resources](#)). The data fits on these faults are generally better than on the SAF, with discrepancies in the mean model being attributable to conflicts between slip rate and paleoevent rate constraints.

A Posteriori Model Evaluation. Each inversion run provides quantitative metrics on how well the final model fits each data constraint (see Appendix N, Page *et al.*, 2013). In principal, these data could be used to adjust logic-tree branch weights *a posteriori* (e.g., using Bayes theorem with the *a priori* branch weights listed in Fig. 3). Likewise, some of the pre-inversion metrics, such as the implied off-fault coupling coefficients discussed in the [Inversion Setup and Associated Gridded Seismicity](#) section, could be used to rank models. We have not attempted any such branch-weight modifications here, however, because doing so will require more careful analysis in terms of avoiding cases in which a good fit to data is actually the result of two incorrect components canceling each other.

Fits to Data Not Used in the Inversion

One type of observation not included in the inversion is the extent to which paleoseismically inferred events are observed to co-rupture neighboring trench sites simultaneously (event correlation, or lack thereof). For example, such inferences are an important component of the “stringing pearls” methodology of [Biasi and Weldon \(2009\)](#). Appendix N (Page *et al.*, 2013) demonstrates that currently available correlation data not only agree well with UCERF3 results, but also generally agree better than those implied by UCERF2. The interpretive uncertainties are admittedly large with respect to these correlation data because samples are limited, and correlation does not necessarily mean rupture in the same event due to uncertainty in the event dates.

Appendix N also compares UCERF3 results to a few different multifault rupture statistics, such as how often ruptures involve fault sections with different names and how many times ruptures jump across fault steps of various distance thresholds. Even considering data uncertainties and interpretive assumptions, the analysis implies that, if anything, UCERF3 has too few multifault ruptures, not too many.

[Wells \(2013\)](#) presented a preliminary update to the [Wells and Coppersmith \(1994\)](#) global database, including a list of magnitude, rupture area, rupture length, and average slip for a number of historical earthquakes. Figure 21 compares the histogram of observed rupture lengths based on 258 events in the dataset with the frequency of rupture lengths predicted by the UCERF3 branch-averaged model, which agree quite well. Again, if anything UCERF3 underpredicts the rate of the longest events. However, this comparison assumes both a uniform sampling of global event sizes and that California

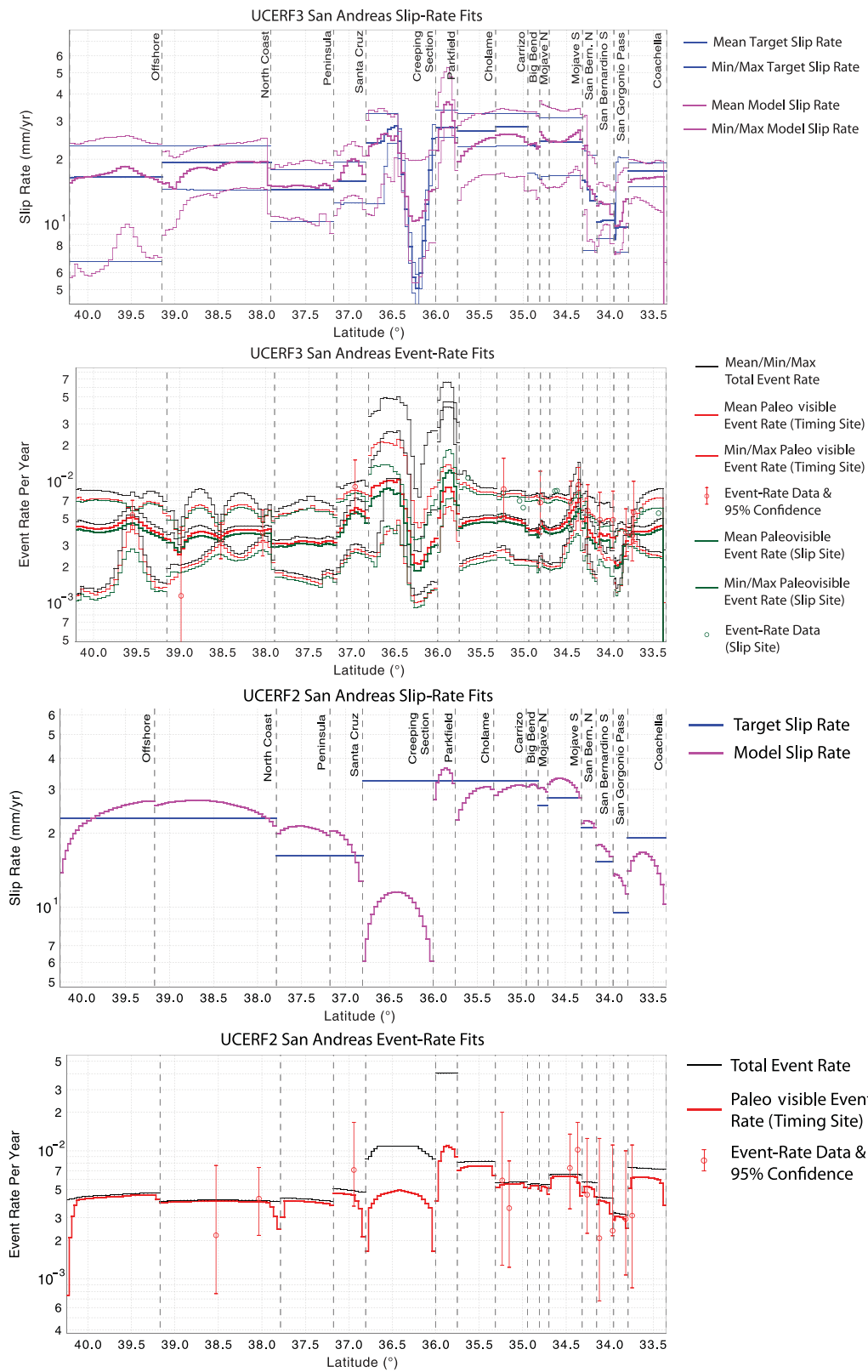


Figure 20. Latitudinal plots showing slip rate and paleoseismic data fits for the southern San Andreas fault, for both UCERF3 (top) and UCERF2 (bottom). The paleoseismic data on the UCERF2 plot are those used in that study, whereas the version of this figure in Appendix N (Page *et al.*, 2013) compares UCERF2 results to UCERF3 data. “Paleo visible” means that rupture rates have been reduced by P_r^{paleo} in equation set (2) (see Table 6) to reflect what might be seen in a trench.

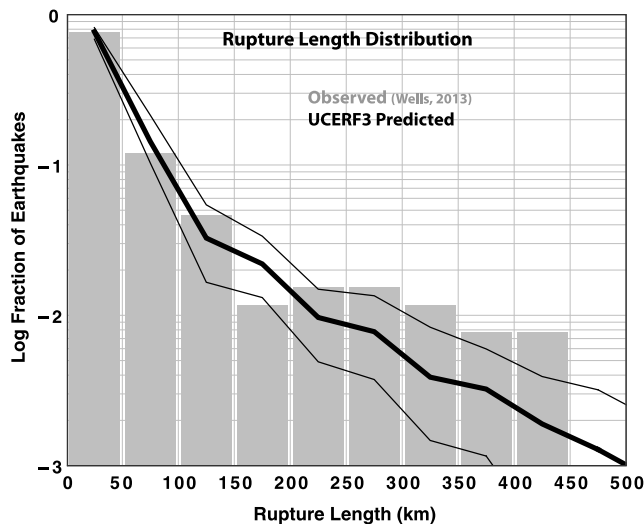


Figure 21. The observed rupture lengths from a global data compilation of 258 earthquakes (Wells, 2013), compared to the distribution implied by UCERF3 (thicker black line represents branch-averaged values, and thin lines represent the minimum and maximum among all branches). Curves have been normalized to density functions (values sum to 1) for comparison purposes.

has the same observed distribution, both of which could be questioned.

The preceding analyses indicate that UCERF3 is reasonable with respect to multifault rupture statistics and that our exclusion of the improbability constraint (equation set 4) seems to be justified. Good statewide statistics do not, however, guarantee that the data for individual faults are also well fit. The fault-by-fault review meetings (Table 3) did not reveal egregious problems. To allow users to judge for themselves, we have generated participation rate maps that show the frequency with which other fault sections co-rupture (or participate) with any given section (see Fault Section Participation Maps under U3 Supplementary Figures in [Data and Resources](#)), as exemplified for the Cucamonga fault in

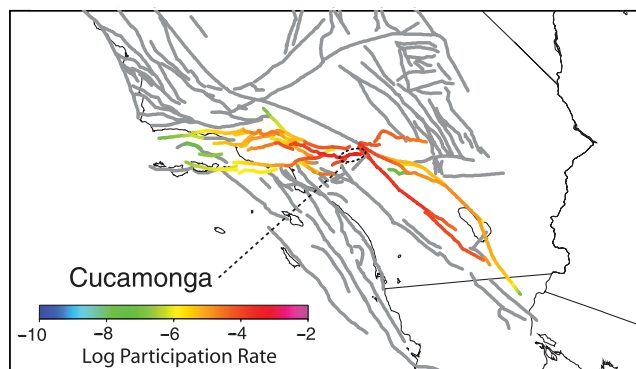


Figure 22. Map showing the rate at which the Cucamonga co-ruptures (participates) with other fault sections for the branch-averaged UCERF3 model (for *Fault Model 3.1*). Such plots for other fault sections are available in the Fault Section Participation Maps under U3 Supplementary Figures (see [Data and Resources](#)).

Figure 22. Note that this figure does not show a rupture, but rather the combined sum of many different ruptures that connect with Cucamonga in different ways.

Noda and Lapusta (2013) recently presented a “plausible physical mechanism” for ruptures passing completely through the creeping section of the SAF, which had zero probability of occurrence in UCERF2. The branch-averaged recurrence intervals for UCERF3 are as follows: 150,000 years between the center of the Offshore and Coachella sections, 2500 years between the center of the North Coast and Mojave sections, and 900 years between the Parkfield and Santa Cruz sections. While these recurrence intervals seem reasonable to us, we also caution that they have high uncertainties due to several modeling assumptions.

Another evaluation metric is the coefficient of variation (COV) for slip at a site, computed as the standard deviation of paleo-observable slip per event divided by the mean. Figure 23 shows a histogram of subsection COVs for the reference logic-tree branch. The center of the peak is about 0.42, which is a central value among alternative scaling relationships; *EllsworthB* produces the smallest value (about 0.33), and *HanksBakun08* produces the largest value (0.47). These results are only a bit less than the values of 0.45–0.5 inferred by Hecker *et al.* (2013) from a global paleoseismic data compilation. However, the latter includes intraevent variability (along-strike variability within a given observed rupture), whereas our values only include the amount of that captured by our average *Tapered* slip model for D_{sr} (or none for the equally weighted *Boxcar* branches). Our values are therefore roughly consistent. However, evaluation of this will be more relevant for any future GR logic-tree branches, as the Hecker *et al.* (2013) study concluded that their observed COVs are incompatible with a GR model.

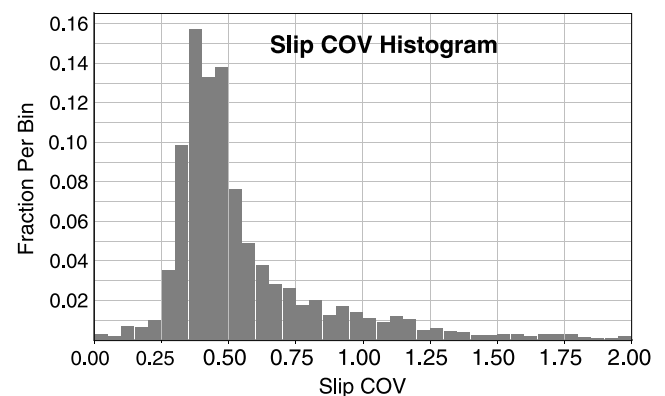


Figure 23. The coefficient of variation (COV) for average slip per event, in which each sample is the standard deviation of slip on a subsection divided by the mean slip, taken among all subsections for the reference logic-tree branch inversion. The rates of each rupture and the probability of paleoseismic observance ($p_r^{\text{paleo-slip-proxy}}$) have been accounted for in generating this plot.

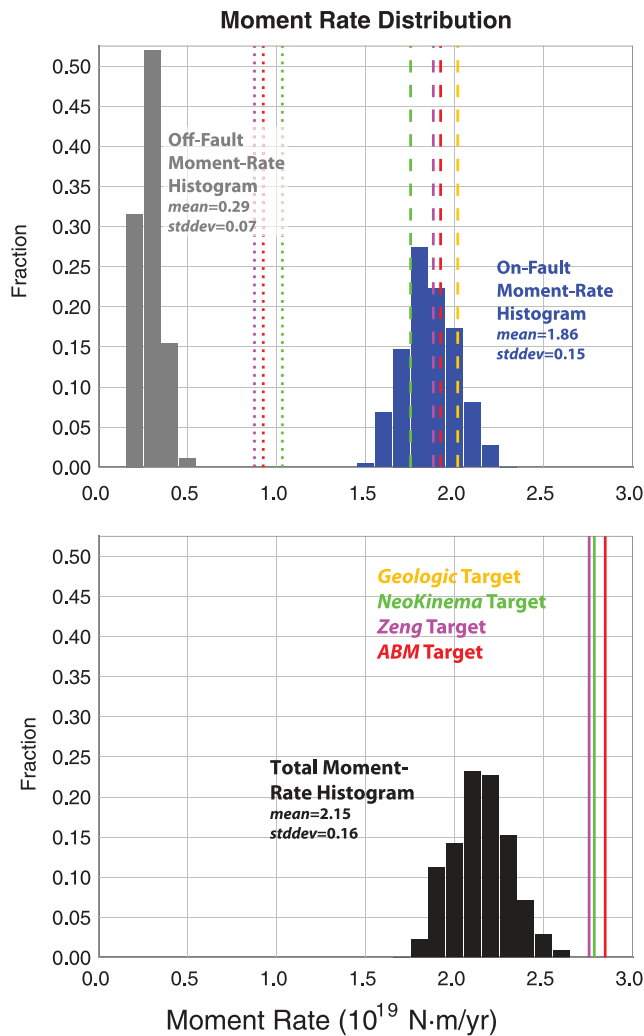


Figure 24. The distribution of regional moment rates implied by UCERF3 logic-tree branches (including their weights), in which blue represents total on-fault (including subseismogenic ruptures), gray is the off-fault, and black is the total combined rate. The vertical lines (dotted lines for off-fault and dashed lines for on-fault values) represent the various model targets as listed in Table 5 and as labeled in the bottom figure legend.

Hazard-Related Metrics

This section presents evaluation metrics that are particularly relevant to hazard implications.

Total Regional Moment Rates. Figure 24 shows the regional moment rate distributions implied by the UCERF3 logic-tree branches, as well as the deformation model targets listed in Table 5. The solution on-fault values are in general agreement with the targets, but the off-fault rates are well below deformation model values. As discussed above (e.g., under [Deformation Models](#) section), the off-fault moment rates are not explicitly used in UCERF3, whereas the model values are implied by the choice of total regional earthquake rate, maximum magnitude off fault, and other branch choices. The reason for this off-fault discrepancy re-

mains unresolved, although it may be associated with assumptions made in calculating the deformation model values (Appendix C, [Parsons et al., 2013](#)). We also note that the coupling coefficients implied by geodetic deformation in broad regions are subject to considerable uncertainty, with values between 20% and 100% being cited in the literature (e.g., [Ward, 1998](#); [Kagan, 2002a,b](#); [Jenny et al., 2004](#); [Masson et al., 2005](#); [Pancha et al., 2006](#); [Rontogianni, 2008](#)). The total moment rate implied by the earthquake catalog is 2.29×10^{19} N·m/yr, in good agreement with the average model values of both UCERF3 (2.15×10^{19} N·m/yr) and UCERF2 (2.27×10^{19} N·m/yr).

Fault Section Participation MFDs. Hazard at a site is often dominated by one or more nearby faults, so a particularly important metric is the participation MFD, which quantifies the rate at which ruptures occur on each fault section (even if they nucleate elsewhere). While these MFDs were prescribed in UCERF2, UCERF3 derives them by finding the range of models that fit the data. The characteristic MFD nucleation constraint (equation set 7) overdetermines the inversion for fault section MFDs, so the remaining concerns are whether simulated annealing can find the global minimum and whether the results are robust with respect to equation-set weights (both of which are quantified in the [Sensitivity Tests](#) section).

Because it is not practical to look at the participation MFDs for all ~2600 fault subsections, we aggregate results back onto the 350 main fault sections, which also aids in making meaningful comparisons to UCERF2. Results for all fault sections are provided under Fault Section MFDs in the U3 Supplementary Figures (see [Data and Resources](#)), with Figure 25 providing a few representative examples. Participation MFDs for the two SAF sections (Peninsula and Mojave N) are very consistent between UCERF2 and UCERF3. For the two other San Francisco Bay area faults (Calaveras N and Hayward N), UCERF3 has a wider range of magnitudes and lower total rates of supra-seismogenic ruptures. Of the two Los Angeles region examples, (San Cayetano and Cucamonga) both have lower total UCERF3 rates because they participate in larger magnitudes. In fact, Cucamonga represents the biggest rate change that is due primarily to methodological differences (the inclusion of multifault ruptures, as depicted in Fig. 22). Both of these cases were viewed as an improvement by participants of the fault-by-fault review meetings (Table 3), and the Cucamonga multifault ruptures are supported by the static and dynamic-stress modeling of [Anderson et al. \(2003\)](#).

The UCERF2 fault section MFDs are generally smoother than those for UCERF3, which is only because the former have aleatory variability in magnitude for a given rupture area (a Gaussian magnitude PDF applied to each characteristic rupture, with a standard deviation of 0.12 and truncated at ± 2 standard deviations). For example, there are only 10 different magnitudes for all characteristic model events on the northern SAF in UCERF2, so without this aleatory

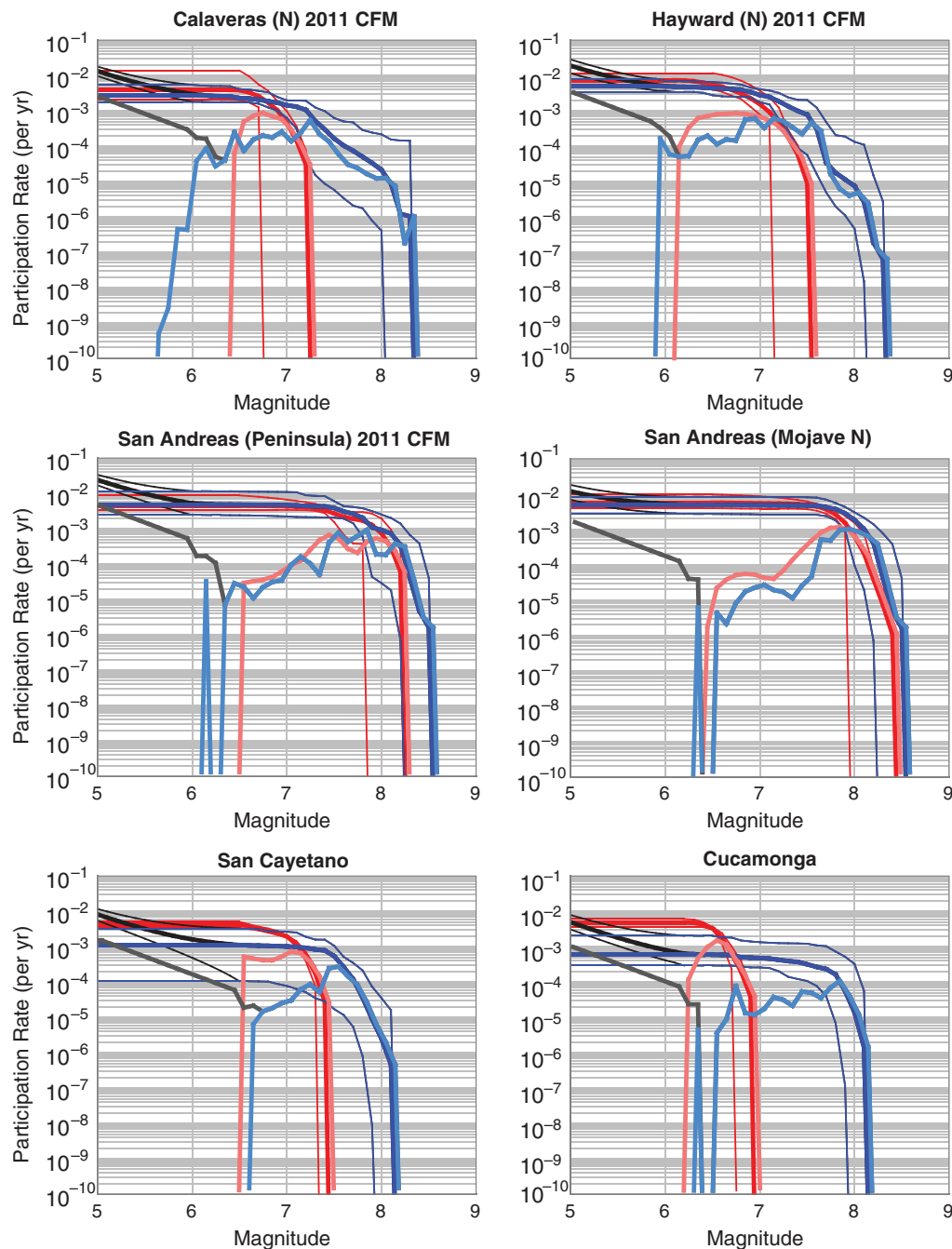


Figure 25. Examples of fault section participation MFDs averaged over all logic-tree branches and weighted accordingly, in which UCERF3 results are in blue and UCERF2 are in red. The corresponding fault sections are as labeled. The darker colored lines are cumulative distributions, and the lighter colored lines are incremental. The black and gray curves are UCERF3 MFDs with subseismogenic rupture added (total on-fault MFD). The thinner lines represent cumulative-distribution minimum and maximum among all logic-tree branches. It is important to understand that “participation” includes all ruptures that touch any part of the parent fault section (even if a large rupture extends only a few subsections in at one end). For this reason, participation MFDs at a point on the fault (e.g., a paleoseismic trench) will be less than or equal to those shown here. Results for other fault sections are provided in Fault Section MFDs in the U3 Supplementary Figures (see [Data and Resources](#)).

variability UCERF2 results would be spikier than those of UCERF3. Whether or not to apply such aleatory variability in UCERF3 is a hazard modeling question not addressed in this report, except to note that the option exists for users who want it. The point here is that UCERF2 fault section MFDs are not really any smoother than those of UCERF3.

Subregion MFDs. Figure 26 shows the mean and range of nucleation MFDs, for both UCERF2 and UCERF3, in rectangular regions surrounding San Francisco (SF), Los Angeles (LA), and in the vicinity of the Northridge fault. These box regions are mapped in Figure 27, which also shows the ratio of *Off-Fault Spatial Seis PDFs (SpatialPDF)* between

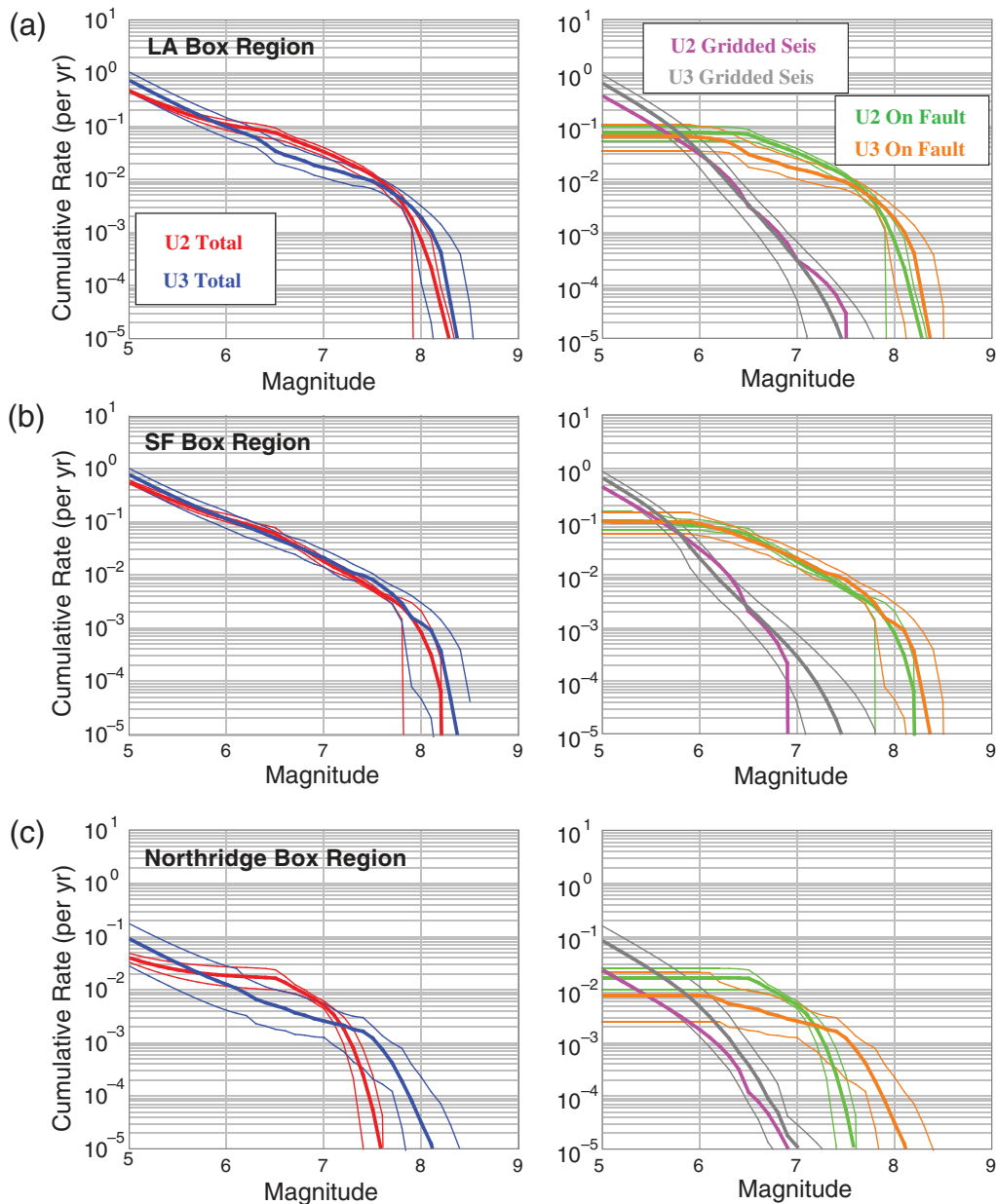


Figure 26. (a) Total branch-averaged cumulative MFD for the Los Angeles (LA) region depicted in Figure 27. Blue is for UCERF3, red is for UCERF2, and the thin lines represent the minimum and maximum over all branches. Aftershocks have been added back in for UCERF2 by reversing the procedure described in the [Gardner–Knopoff Aftershock Filter](#) section. (b) and (c) Equivalent plots for the San Francisco (SF) and Northridge regions depicted in Figure 27.

UCERF2 and UCERF3 and the ratio of branch-averaged, on-fault moment rates. Note that the MFDs shown in Figure 26 are cumulative and that aftershocks have been added back in for UCERF2 (by reversing the procedure described in the [Gardner–Knopoff Aftershock Filter](#) section). Table 14 lists the number of fault sections, the moment rate, and various event rates inside each of these regions.

The UCERF3 MFDs for the Los Angeles region are more consistent with a GR distribution, with lower mean rates from M 6.0 to 7.7 and higher mean rates above, as expected from the inclusion of multifault ruptures. The range of MFDs from the respective logic trees generally overlaps, except between M 6.5

and M 7.0 and just barely at M 5. The UCERF3 rate of $M \geq 5$ is about 58% greater than for UCERF2 (Table 13), which is consistent with the branch-averaged 43% increase in $R_{M \geq 5}^{\text{total}}$. The total rate of $M \geq 6.7$ events has gone down by a factor of 2 in UCERF3 due to the inclusion of multifault ruptures. Although 40 new fault sections were added to the Los Angeles region in UCERF3, the new deformation models actually lowered the average total moment rate by about 7% (Table 14).

The UCERF2 and UCERF3 MFDs for the San Francisco region are much more consistent. The rate of $M \geq 5$ events has increased by 39% in UCERF3, which also is generally consistent with the effective 43% increase in $R_{M \geq 5}^{\text{total}}$. The rate of

Table 14
Number of Fault Sections and Total Rates in Various Subregions*

	LA Region		SF Region		Northridge Region	
	U3	U2	U3	U2	U3	U2
Number of Fault Sections	102	62	67	34	18	11
On-Fault Moment Rate [†]	4.18	4.51	3.12	2.91	0.43	0.36
Total Rate $M \geq 5$ (per year)	0.736	0.465	0.780	0.561	0.091	0.040
Total Rate $M \geq 6.7$ (per year)	0.025	0.053	0.035	0.037	0.0036	0.011

*The Los Angeles (LA), San Francisco (SF), and Northridge regions are shown in Figure 27.

U3 corresponds to UCERF3 and U2 to UCERF2, both averaged over all logic-tree branches.

Aftershocks are included, as described in the Figure 26 caption.

[†]Moment rates are in units of 10^{18} N·m/yr.

$M \geq 6.7$ events is essentially unchanged, while the rates of $M \geq 7.5$ are about 48% higher, which reflects a trade-off between the inclusion of multifault ruptures and an $\sim 7\%$ increase in moment rate from the addition of 33 new fault sections (Table 14).

The UCERF3 MFD for the Northridge box (Fig. 26c) follows GR much more so than that of UCERF2. In fact, we included this region precisely because the strongly characteristic UCERF2 MFD was found to produce runaway aftershock sequences in preliminary Northridge earthquake ETAS simulations (Field, 2012). The inclusion of multifault ruptures has cut the average rate of $M \geq 6.7$ events by a factor of 3, even though UCERF3 has a 19% moment rate increase in this area (Table 14). This change represents a significant improvement over UCERF2.

Participation Rate Maps. Figure 28 compares the mean UCERF3 participation rate maps for various magnitude

thresholds with those for UCERF2. The ratio for $M \geq 5$ is generally high as a result of the increase in $R_{M \geq 5}^{\text{total}}$, although there are some low areas near faults. The ratios for $M \geq 6.7$ are more extreme, including low areas near the UCERF2 type C zones in northeast California, high areas where new faults have been added (e.g., offshore San Diego), and some low values on preexisting faults, reflecting lowered rates because of the inclusion of multifault ruptures. More areas are capable of $M \geq 7.7$ events in UCERF3 due to an increase in $M_{\text{max}}^{\text{(off-fault)}}$, and more areas generate $M \geq 8$ events due to multifault ruptures. Such events on Elsinore and Death Valley faults are seen in UCERF2 but not UCERF3, because the former includes aleatory magnitude–area variability.

Implied Segmentation. Figure 29 from Appendix N (Page *et al.*, 2013) shows model-implied segmentation along the SAF for both UCERF3 and UCERF2. As expected, segmentation is much less pronounced in the new model, which can significantly influence hazard. For example, in a strictly segmented model, a site on a segment boundary has twice as many events at zero distance, on average, than a site halfway down a segment, which is a potential factor of 2 difference in hazard. The effect is less when both single and multisegment ruptures are included, as with UCERF2 type A faults, but strict segmentation was effectively applied to adjacent type B faults in UCERF2. This effect partially explains a hazard reduction identified for the city of Oakland in the next section.

Hazard Curves and Maps. Perhaps the most important questions for UCERF3 are (1) how and why have hazard estimates changed relative to UCERF2? and (2) what are the most influential UCERF3 logic-tree branches? This section addresses these questions, concluding that the dominant factors are deformation models (slip rates) and the new smoothed seismicity model, with methodological differences (multifault ruptures) being important in some places.

A seismic-hazard curve gives the probability of exceeding various earthquake-shaking levels over a specified time period (typically 50 years for building codes) for a site. The shaking can be characterized by a ground-motion parameter, or intensity measure type, with the most widely used including peak ground acceleration (PGA) and spectral accel-

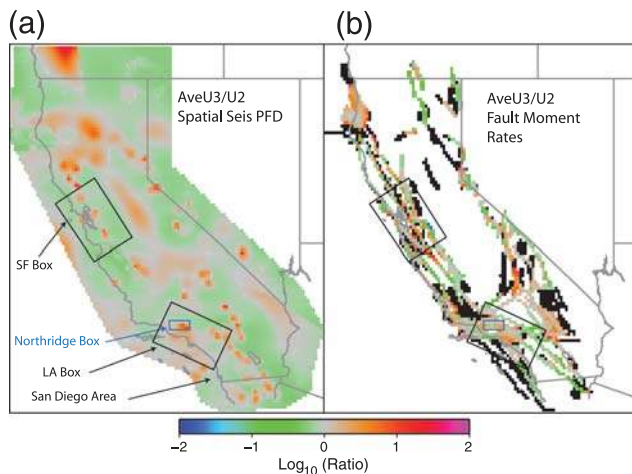


Figure 27. UCERF2 to UCERF3 ratios. (a) Ratio of the average UCERF3 to UCERF2 *Off-Fault Spatial Seis PDF*, equal to $0.5(U2_{\text{sm}} + U3_{\text{sm}})/U2_{\text{sm}}$, in which $U2_{\text{sm}}$ is the UCERF2 smoothed seismicity map (Fig. 14a) and $U3_{\text{sm}}$ is the UCERF3 smoothed seismicity map (Fig. 14b). This ratio does not include the overall regional rate increase for $R_{M \geq 5}^{\text{total}}$. (b) Ratio of branch-averaged, on-fault moment rates between UCERF3 and UCERF2; infinite values are shown in black (due to new faults being added where none existed in UCERF2).

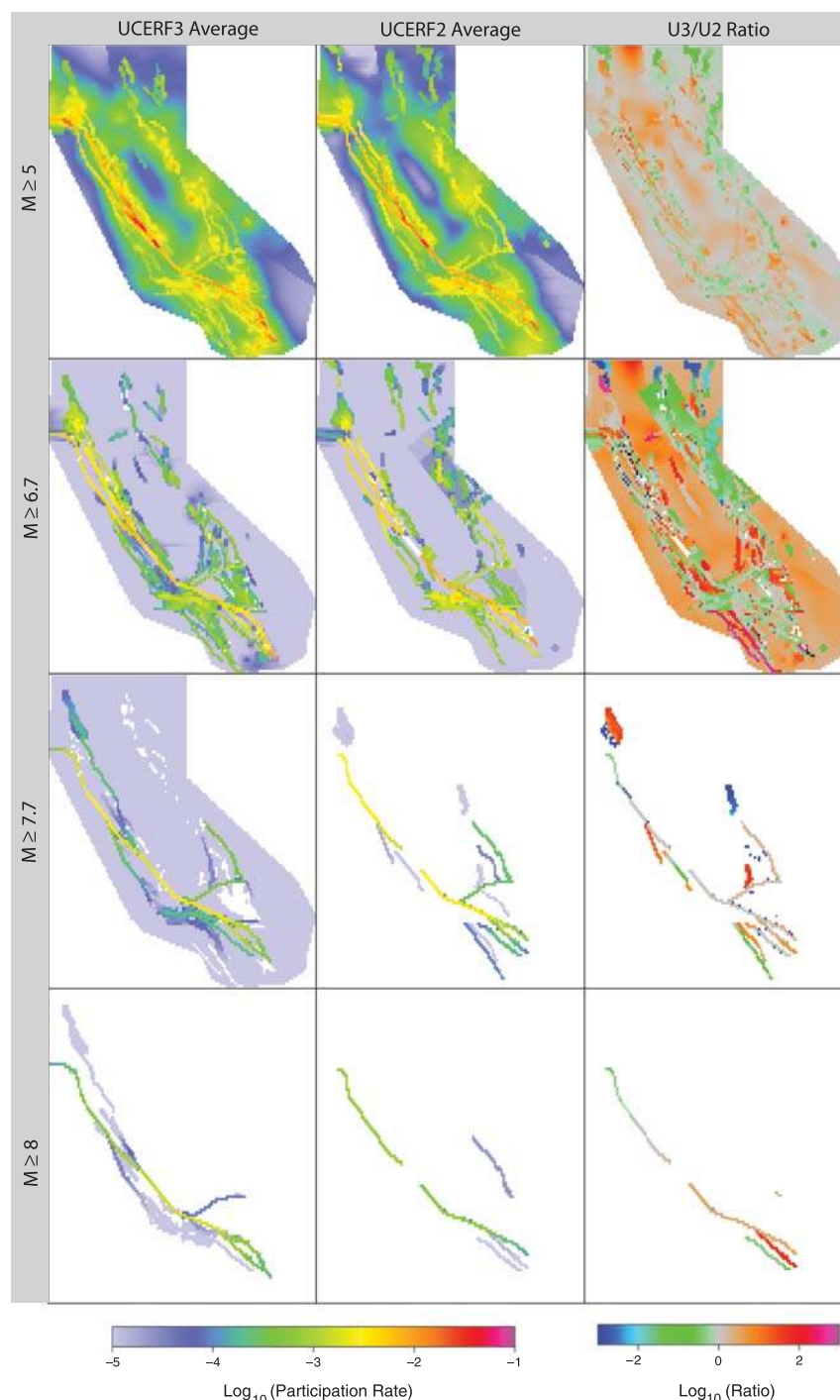


Figure 28. Branch-averaged participation rate maps for UCERF3 and UCERF2 and for the ratio of the two (UCERF3/UCERF2). For the ratios, zero values are white, values above the color scale maximum (10^3) are black, and infinite values are white (where the UCERF2 denominator is zero). These plots have had aftershocks removed in order to make the comparison to UCERF2. The zero patches in the UCERF3 $M \geq 7.7$ map represent the polygons for faults that have a maximum magnitude $M < 7.7$.

eration (SA) at 0.33, 1, and 5 Hz periods (0.33, 1, and 5 Hz SA, respectively). For example, the seismic design provisions recommended by the BSSC (2009) use 1 and 5 Hz SA. To support engineering design and building codes, the USGS NSHMP publishes probabilistic ground-motion maps, which show the shaking levels that have a certain probability of being ex-

ceeded over a given time period (the hazard-curve x -axis value corresponding to some y -axis level, with the latter typically being the 2%- or 10%-in-50-year exceedance probability; see Fig. 30 for an example).

To understand UCERF3 implications, a wide variety of hazard curves and maps have been generated using Open-

San Andreas Fault System Segmentation

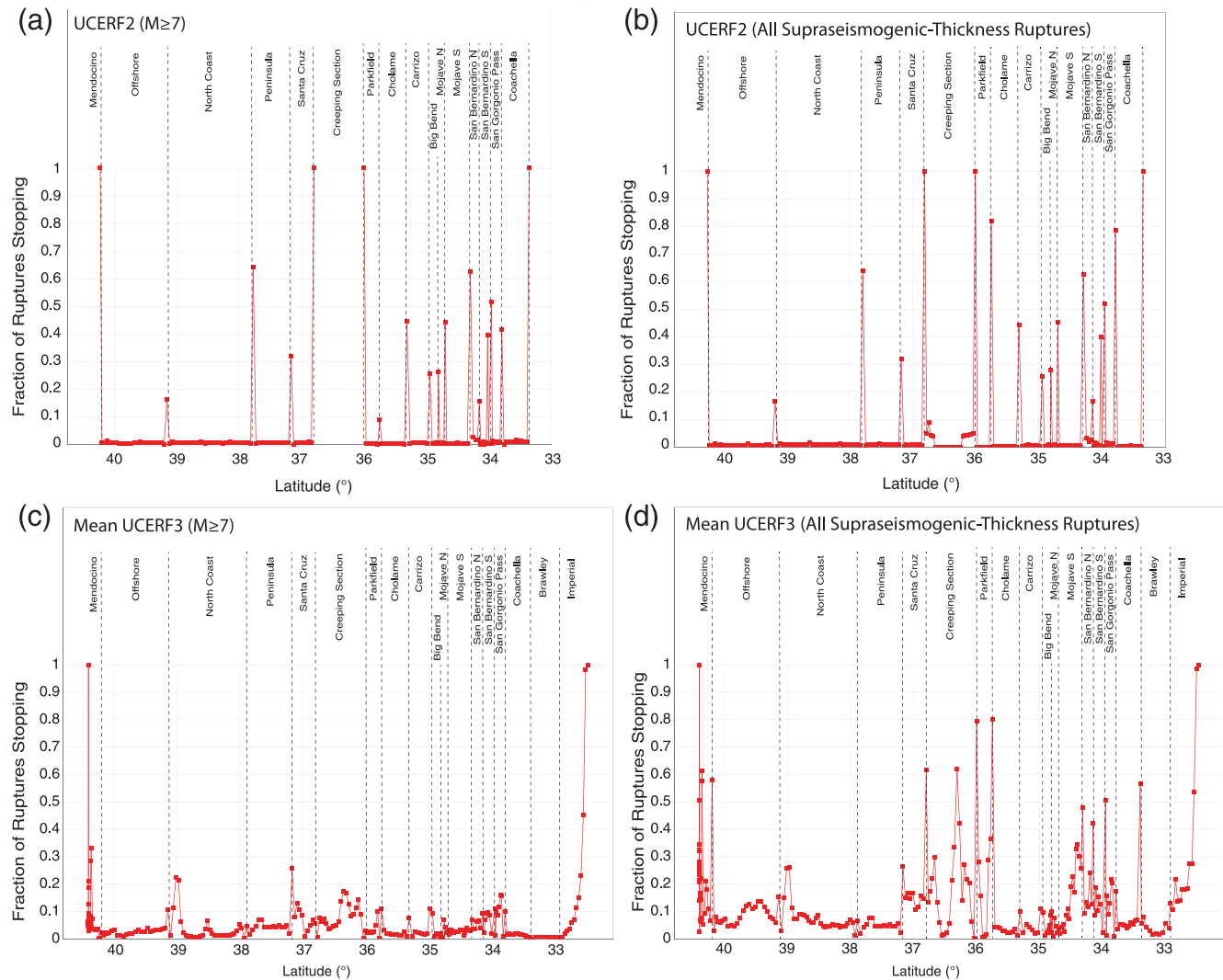


Figure 29. Latitudinal plots showing average model-implied segmentation on the SAF system for UCERF2 (top) and UCERF3 (bottom). The right side includes all supra-seismogenic ruptures, whereas the left side is for only $M \geq 7$ events. The Brawley and Imperial faults were not included in UCERF2 (and are therefore not shown for this model). Red points show the rate at which neighboring subsections do not rupture together, normalized by the total rate of ruptures involving those two subsections. Thus, when the red line reaches 1 there is strict segmentation, and no ruptures break through that location.

SHA (Field *et al.*, 2013; see [Data and Resources](#)), which was the only PSHA code that could accommodate UCERF3 (at least at that time). Doing so, however, required considerable effort in terms of implementing and verifying details needed for a precise replication of official 2008 NSHMP values (based on the USGS NSHMP FORTRAN Code). Documentation of such implementation details will be provided in a forthcoming report, but results for all UCERF3 hazard calculations are currently available, with explanations, as U3 Supplementary Figures (see [Data and Resources](#)).

The results cited here come from this database. To ensure meaningful comparisons, the same set of ground-motion models employed by NSHMP 2008 (for crustal faults) has been used. Although a wide array of hazard metrics are available at the website in the U3 Supplementary Figures, includ-

ing the risk-targeted ground motions now being considered by the BSSC (Luco *et al.*, 2007), we focus only on those needed to make important points here.

Table 15 lists a number of sites where hazard curves have been computed, along with various UCERF3/UCERF2 hazard ratios (or more precisely, ratios of ground motions that have a certain probability of exceedance). The first 21 National Earthquake Hazards Reduction Program (NEHRP) sites are those used by the BSSC when considering updates to seismic design provisions, and those listed as “Other” have been of particular interest to the WGCEP (e.g., added during review). The full hazard-curve results for all these sites, from which the data in Table 15 were obtained, are available under Hazard Curves in the U3 Supplementary Figures (see [Data and Resources](#)). To complement these test-

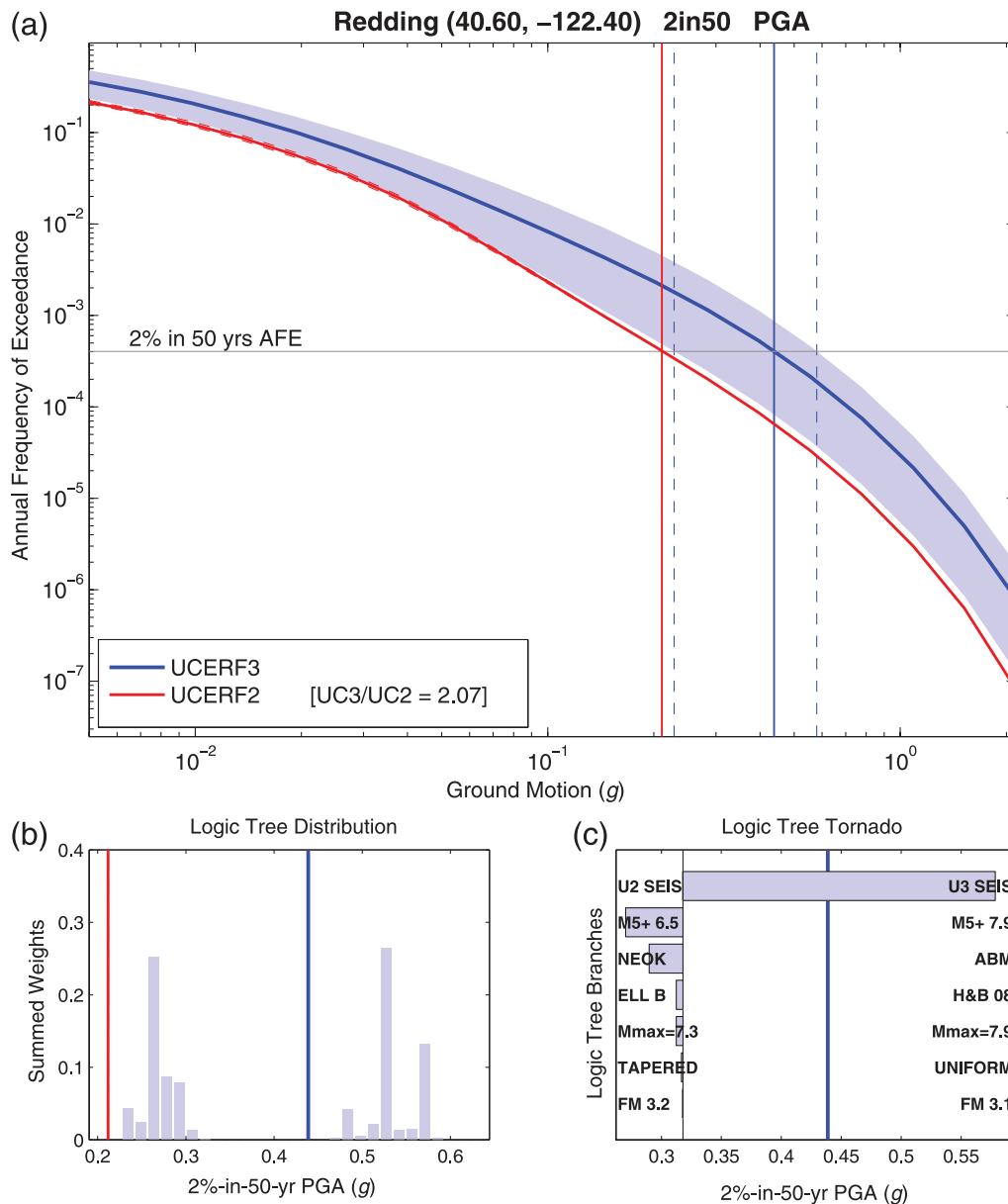


Figure 30. Hazard curve example for PGA at the Redding site listed in Table 15. (a) Comparison of UCERF3 and UCERF2 hazard curves. The blue and red lines mark the weighted mean hazard curve across all UCERF3 and UCERF2 (time-independent) logic-tree branches, respectively. The light blue shaded region delineates the minimum and maximum hazard values among all UCERF3 branches, and the dashed red lines are the same for UCERF2 (just barely visible to the left). The horizontal gray line marks the 2%-in-50-year probability of exceedance level. The vertical lines mark the mean (solid) and minimum and maximum (dashed) 2%-in-50-year ground-motion values. (b) Distribution of 2%-in-50-year ground motions across the UCERF3 logic tree (considering branch weights). Color coding of the vertical lines is the same as at the top. (c) Tornado diagram (e.g., Porter *et al.*, 2012), indicating the influence of each UCERF3 logic-tree branch on the overall uncertainty. The swings away from the thin vertical line represent the influence of changing each branch option, one at a time, relative to the branch corresponding to the median, and ignoring branch weights.

site calculations, we computed a variety of probabilistic ground-motion maps. Figure 31 shows the UCERF3/UCERF2 ratio map for 2%-in-50-year PGA (abbreviated as “2in50 PGA” hereafter).

One goal has been to understand and justify all important hazard differences between UCERF3 and UCERF2, which we define as greater than 10% changes in probabilistic ground motion. Sites with such discrepancies are shown as

non-yellow areas in Figure 31. Although considerable effort has been put into understanding all such cases, we focus here on the more discrepant and informative examples.

The biggest change listed in Table 15 is a factor of 2.32 increase for 2in50 PGA at the Redding site, the location of which is plotted in Figure 31b. The PGA hazard curve for Redding is shown in Figure 30, together with a tornado diagram and histogram revealing the influence of alternative

Table 15

Ratios of UCERF3 to UCERF2 Ground-Motion Exceedance Values for Various Sites, Intensity Measures, and Return Periods*

Site Name	Latitude (°)	Longitude (°)	Group	2% in 50 years				10% in 50 years				RTGM	
				PGA	5 Hz SA	1 Hz SA	0.25 Hz SA	PGA	5 Hz SA	1 Hz SA	0.25 Hz SA	5 Hz	1 Hz
Century City	34.05	-118.40	NEHRP	1.07	1.07	1.04	1.04	1.07	1.05	1.02	1.00	1.06	1.02
Concord	37.95	-122.00	NEHRP	1.02	0.98	1.01	1.09	0.96	0.93	0.94	1.01	0.97	0.98
Irvine	33.65	-117.80	NEHRP	0.91	0.91	0.90	0.98	0.98	0.98	0.92	0.90	0.94	0.91
Long Beach	33.80	-118.20	NEHRP	1.15	1.13	1.11	1.06	1.13	1.11	1.04	1.00	1.12	1.07
Los Angeles	34.05	-118.25	NEHRP	0.94	0.93	0.95	1.09	0.94	0.93	0.91	0.96	0.93	0.93
Monterey	36.60	-121.90	NEHRP	0.96	0.94	0.96	0.99	0.93	0.93	0.96	0.99	0.97	0.98
Northridge	34.20	-118.55	NEHRP	1.20	1.18	1.16	1.20	1.15	1.13	1.06	1.03	1.15	1.09
Oakland	37.80	-122.25	NEHRP	0.85	0.83	0.87	0.99	0.81	0.78	0.80	0.90	0.81	0.83
Riverside	33.95	-117.40	NEHRP	1.03	1.02	0.97	1.02	0.98	0.97	0.88	0.85	0.99	0.91
Sacramento	38.60	-121.50	NEHRP	1.11	1.10	1.07	1.10	1.04	1.02	1.02	1.06	1.05	1.03
San Bernardino	34.10	-117.30	NEHRP	0.90	0.89	0.88	1.03	0.89	0.86	0.79	0.81	0.88	0.83
San Diego	32.70	-117.15	NEHRP	1.18	1.19	1.12	1.00	1.37	1.36	1.23	1.06	1.21	1.12
San Francisco	37.75	-122.40	NEHRP	0.94	0.93	0.91	0.92	0.92	0.90	0.89	0.90	0.91	0.90
San Jose	37.35	-121.90	NEHRP	1.07	1.07	1.12	1.20	1.05	1.04	1.08	1.18	1.04	1.09
San Luis Obispo	35.30	-120.65	NEHRP	1.09	1.08	1.07	1.09	1.03	1.02	1.00	0.99	1.06	1.04
San Mateo	37.55	-122.30	NEHRP	0.96	0.95	0.95	0.96	0.96	0.96	0.95	0.96	0.95	0.95
Santa Barbara	34.45	-119.70	NEHRP	0.91	0.88	0.93	1.00	0.83	0.81	0.81	0.89	0.86	0.89
Santa Cruz	36.95	-122.05	NEHRP	1.03	1.03	1.04	1.07	1.03	1.03	1.05	1.06	1.04	1.05
Santa Rosa	38.45	-122.70	NEHRP	0.88	0.88	0.87	0.93	0.87	0.85	0.82	0.85	0.88	0.86
Vallejo	38.10	-122.25	NEHRP	1.28	1.23	1.26	1.25	1.13	1.10	1.12	1.12	1.13	1.16
Ventura	34.30	-119.30	NEHRP	0.94	0.94	0.96	1.08	0.94	0.92	0.89	0.94	0.91	0.92
Bakersfield	35.35	-119.00	Other	1.06	1.06	1.06	1.07	1.02	1.02	0.99	0.97	1.04	1.01
Big Sur	36.25	-121.75	Other	1.26	1.22	1.24	1.17	0.94	0.94	0.96	0.95	1.13	1.17
Brawley	33.00	-115.55	Other	1.09	1.08	1.14	1.38	1.10	1.08	1.08	1.12	1.08	1.09
Brookings	42.05	-124.25	Other	2.06	2.12	1.98	1.81	1.67	1.66	1.52	1.54	1.91	1.80
Carson City	39.15	-119.75	Other	1.19	1.26	1.19	0.98	1.18	1.22	1.15	1.00	1.22	1.16
Coalinga	36.15	-120.40	Other	1.03	1.03	0.98	1.02	1.06	1.05	0.97	0.95	1.05	0.98
Cucamonga	34.20	-117.55	Other	0.53	0.53	0.67	0.98	0.57	0.57	0.60	0.77	0.57	0.64
Death Valley	36.35	-116.85	Other	0.58	0.56	0.60	0.73	0.57	0.58	0.58	0.61	0.58	0.62
Diablo Canyon	35.20	-120.85	Other	0.90	0.85	0.84	0.92	0.88	0.87	0.88	0.89	0.88	0.88
Eureka	40.80	-124.20	Other	1.05	1.02	1.07	1.04	1.17	1.16	1.10	1.02	1.06	1.08
Fresno	36.75	-119.75	Other	1.22	1.22	1.14	1.09	1.15	1.15	1.08	1.06	1.17	1.11
Malibu West	34.05	-118.95	Other	0.73	0.68	0.71	0.95	0.89	0.86	0.83	0.91	0.77	0.78
Morgan Hill	37.15	-121.65	Other	0.94	0.93	1.05	1.24	0.94	0.94	1.01	1.19	0.96	1.03
Palm Springs	33.85	-116.55	Other	0.93	0.90	0.90	0.94	0.91	0.91	0.88	0.89	0.91	0.88
Palmdale	34.50	-118.00	Other	0.95	0.93	0.93	0.97	0.92	0.92	0.87	0.86	0.93	0.91
Pasadena	34.15	-118.15	Other	0.86	0.85	0.91	1.09	0.78	0.76	0.79	0.91	0.82	0.86
Redding	40.60	-122.40	Other	2.32	2.29	1.67	1.18	2.21	2.19	1.42	1.12	2.15	1.55
Reno	39.55	-119.80	Other	0.93	0.94	0.84	0.71	1.00	1.02	0.93	0.82	0.99	0.89
San Onofre	33.40	-117.55	Other	1.05	1.04	1.03	1.02	0.99	0.99	0.95	0.92	1.04	0.99
AC01	34.42	-118.10	PBR	0.98	0.97	0.98	1.02	0.95	0.94	0.93	0.94	0.95	0.95
ACTN	34.46	-118.18	PBR	0.97	0.96	0.98	1.02	0.94	0.92	0.92	0.93	0.94	0.94
BKBU	34.56	-117.73	PBR	0.98	0.99	0.98	1.00	0.98	1.00	0.94	0.89	0.99	0.95
GLBT	33.96	-117.38	PBR	1.03	1.01	0.97	1.02	0.97	0.96	0.87	0.84	0.98	0.90
GOPH	33.90	-117.36	PBR	1.02	1.01	0.96	1.00	0.97	0.96	0.88	0.84	0.98	0.91
GV03	34.28	-117.23	PBR	0.67	0.66	0.69	0.86	0.71	0.70	0.67	0.74	0.70	0.68
LBUT2	34.59	-117.81	PBR	0.98	0.99	0.98	1.01	0.98	0.99	0.94	0.90	0.99	0.95
LMAT	33.79	-117.40	PBR	1.10	1.11	1.03	0.96	1.13	1.14	1.03	0.92	1.11	1.02
LPER	33.89	-117.16	PBR	0.82	0.78	0.77	0.88	0.77	0.76	0.68	0.68	0.79	0.74
MKBD	33.88	-117.39	PBR	1.03	1.03	0.97	1.00	0.99	0.99	0.90	0.86	1.00	0.93
MRVY	33.93	-117.17	PBR	0.83	0.80	0.82	0.95	0.76	0.74	0.66	0.69	0.79	0.75
NUEVO	33.78	-117.15	PBR	0.93	0.90	0.88	0.94	0.87	0.86	0.80	0.78	0.89	0.84
PACI2	34.39	-118.05	PBR	0.99	0.98	0.99	1.03	0.95	0.94	0.93	0.94	0.95	0.95
PBWL	34.41	-117.86	PBR	1.00	1.00	0.95	0.98	1.02	1.03	0.96	0.88	1.03	0.96
PEDLEY1	33.99	-117.46	PBR	1.04	1.03	0.99	1.02	0.99	0.98	0.90	0.87	0.99	0.92

(continued)

Table 15 (Continued)

Site Name	Latitude (°)	Longitude (°)	Group	2% in 50 years				10% in 50 years				RTGM	
				PGA	5 Hz SA	1 Hz SA	0.25 Hz SA	PGA	5 Hz SA	1 Hz SA	0.25 Hz SA	5 Hz	1 Hz
PERR2	33.79	−117.24	PBR	0.97	0.95	0.91	0.96	0.93	0.93	0.86	0.83	0.95	0.89
PERRM	33.80	−117.25	PBR	0.96	0.95	0.91	0.96	0.93	0.92	0.86	0.83	0.95	0.89
PIBU	34.65	−117.85	PBR	0.99	1.00	0.99	1.01	0.98	0.99	0.94	0.91	0.99	0.95
SW01	34.30	−117.34	PBR	0.79	0.78	0.81	0.95	0.77	0.75	0.72	0.78	0.77	0.76
UCR	33.96	−117.32	PBR	0.99	0.96	0.92	1.01	0.94	0.92	0.82	0.80	0.94	0.86

*In the Group column, “NEHRP” sites are from table C11.4-1 of the 2009 Recommended Seismic Provisions for New Buildings and Other Structures (BSSC, 2009). Those listed as “Other” are WGCEP-chosen sites, and those listed as “PBR” are locations of precariously balanced rocks (James Brune, written comm., 2012). PGA, 5 Hz SA, 1 Hz SA, 0.25 Hz SA, and RTGM are risk-targeted ground motions described by [Luco et al. \(2007\)](#).

logic-tree branches, relative to a median branch. The *Spatial-SeisPDF* logic-tree branch is clearly most influential at this site; the two options (*UCERF2* versus *UCERF3 Smoothed Seis*) create a strong bimodal distribution of ground-motion levels. This is because Redding is situated near a high-seismicity area that is clearly visible in the *UCERF3 Smoothed Seis* model but spreads into other regions in the *UCERF2 Smoothed Seis* model. Adding the new *Spatial-SeisPDF* option has therefore increased the hazard at Redding, as well as at other sites indicated in Figure 31b (which represent areas of correlation between Fig. 27a and Fig. 31a). However, the more focused smoothing kernels have also reduced the hazard at areas further from the seismicity clusters.

San Diego has a factor of 1.37 increase for 10in50 (10%-in-50-year) PGA, which is the largest change among the NEHRP sites in Table 15. This increase is clearly attributable to the addition of new offshore faults, including the following, which are in black in Figure 27: Carlsbad, Thirty Mile Bank, San Clemente, San Diego Trough north, San Diego Trough south, Oceanside, and half of Coronado Bank (the latter was used in only one of two UCERF2 fault models). Figure 31c highlights this and other areas influenced by the addition of faults or by changes in average fault moment rates.

Cucamonga exhibits the biggest decrease among all sites in Table 15, with a factor of 0.53 reduction for 2in50 PGA, which can also be seen in the ratio map of Figure 31d. As noted previously in the context of Figure 25, the rate of $M \geq 6.7$ events on the Cucamonga fault has dropped by a factor of 3, due entirely to the inclusion of multifault ruptures (going from $M \sim 6.7$ single-segment ruptures in UCERF2, to also participating in events up to $M \sim 8$ in UCERF3). Therefore, this fault also represents the biggest methodological change with respect to hazard. Another example is the San Cayetano fault section, as indicated in Figures 31d and 25. We reiterate that both these cases were deemed a significant improvement at the fault-by-fault review meetings (Table 3).

The Oakland site shows the largest reduction amongst NEHRP sites in Table 15, a drop of 22% for 10in50 5 Hz SA, which is more challenging in terms of parsing influences. The hazard in Oakland is dominated by the nearby Hayward North fault section, which actually had a 90% increase in the average moment rate. This increase is apparently countered by it now participating in more multifault ruptures; for example,

the 10,000-year event has gone from $M \sim 7.3$ in UCERF2 to $M \sim 7.7$ in UCERF3 (Fig. 25). Another significant factor, revealed by high-resolution hazard maps, is that Oakland is situated near a UCERF2 segment boundary, which gives it a higher rate of events in close proximity than at other locations along the fault. Removing the strong influence of this segment boundary in UCERF3 therefore contributed to reducing the hazard in Oakland (another methodological influence).

Other sites of interest include Los Angeles, which has only a minor reduction ($< 10\%$) for the location in Table 15, and San Francisco, which also shows minor differences in Table 15. An exception for the San Francisco site is the 10in50 1 Hz SA, which dropped by 11%. Evaluation of the tornado diagram for this location (shown under Hazard Curves in the U3 Supplementary Figures section; see [Data and Resources](#)) implies that average slip-rate changes are responsible. Sacramento, another site of interest, exhibits an 11% increase for 2in50 PGA. The associated tornado diagram indicates that gridded seismicity is most influential, so the change can be attributed to the total regional rate increase for UCERF3.

To summarize, the following are generally found to be most influential in terms of UCERF2 to UCERF3 hazard changes (listed in descending order of importance, although this has a heavy spatial dependence):

- addition of new faults and average moment rate changes on existing faults,
- addition of the *UCERF3 Smoothed Seis* option,
- inclusion of multifault ruptures in UCERF3, and
- the effective 43% increase in the total rate of $M \geq 5$ events.

This conclusion generally applies to all ground-motion parameters and probability levels examined.

To help quantify the influence of UCERF3 epistemic uncertainties, 2in50 PGA maps were computed for all 1440 logic-tree branches. We then averaged over the options on each branch separately and normalized by the total average to reveal the influence of each. The process is illustrated in Figure 32 for *Deformation Models*, where each option is represented by an average over the associated subset of maps (360 given the four branch options in this example) divided by the average over all 1440 maps. Figure 32 reveals a strong

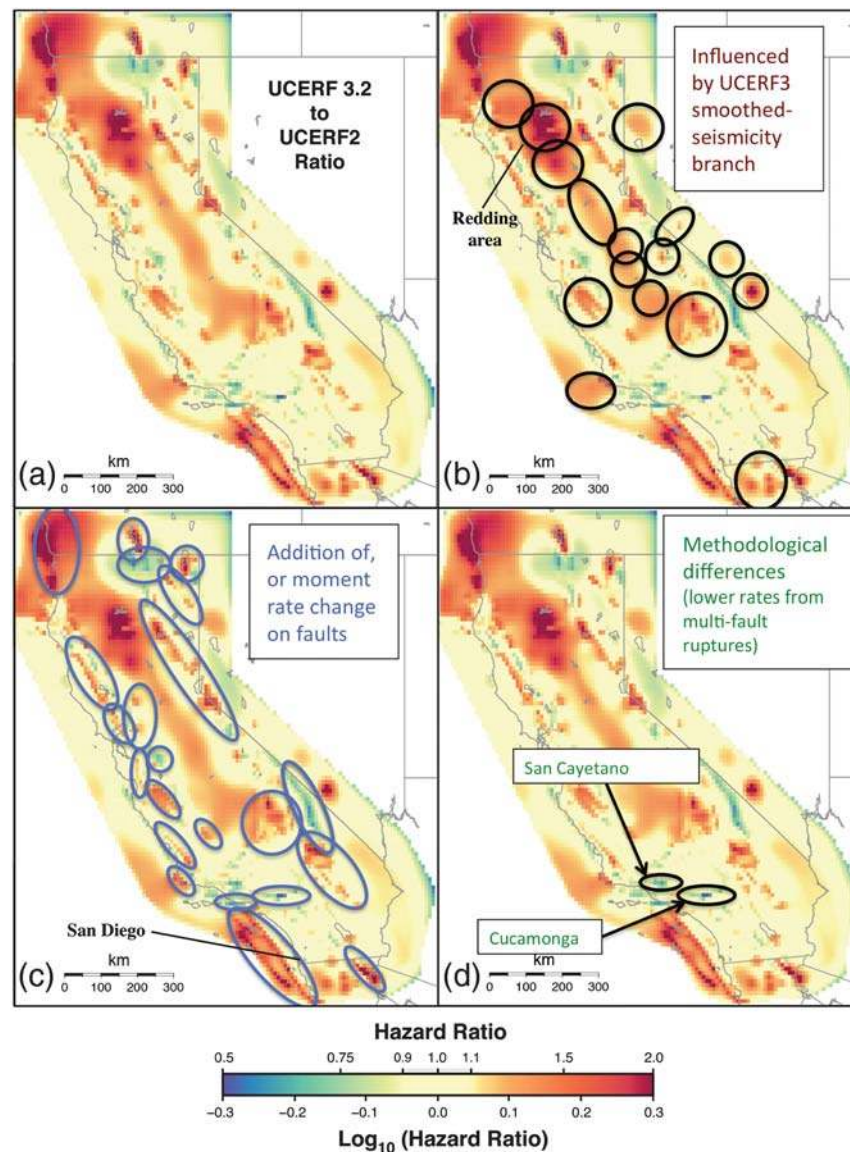


Figure 31. (a) Ratio of UCERF3 2%-in-50 year PGA map divided by that for UCERF2. The ground-motion prediction equations used for these calculations are the same ones used in the NSHMP 2008 maps. Ovals show areas where discrepancies can be explained by (b) addition of the *UCERF3 Smoothed Seism* option; (c) addition of new faults or average moment rate changes on existing faults; and (d) methodological changes in terms of including multifault ruptures.

influence from the block boundaries used in the ABM model (red areas), which was the basis for down weighting this model (because some of these areas may be model artifacts).

The resultant “Branch Ratio Hazard Maps” for all UCERF3 epistemic uncertainties are available in the U3 Supplementary Figures (see [Data and Resources](#)). The most influential choices in descending order of overall importance are *Deformation Models*, *UCERF2* versus *UCERF3 Smoothed Seis*, and *Scaling Relationships*. *Fault Models* and *Total $M \geq 5$ Event Rate* have some influence in specific areas, while $M_{\text{max}}^{\text{(off-fault)}}$ and *Slip Along Rupture (D_{sr})* have very little influence. These conclusions are generally applicable to other return periods and ground-motion parameters, although we reemphasize the spatial dependence of such conclusions.

Sensitivity Tests

Simulated Annealing Convergence and Nonuniqueness.

We first consider how well the simulated annealing algorithm converges, which depends on the problem and how long the inversion algorithm is run. We also consider the problem of nonuniqueness, in particular how the simulated annealing samples the null space. Given that there can be an infinite, yet bounded, number of viable models in this situation, the more appropriate question is how many runs are needed to obtain stable averages of individual solutions. We refer to both of these issues as convergence because the convergence and nonuniqueness problems cannot be separated in our tests.

Whether the inversion is overdetermined, underdetermined, or mixed depends on the evaluation metric of interest.

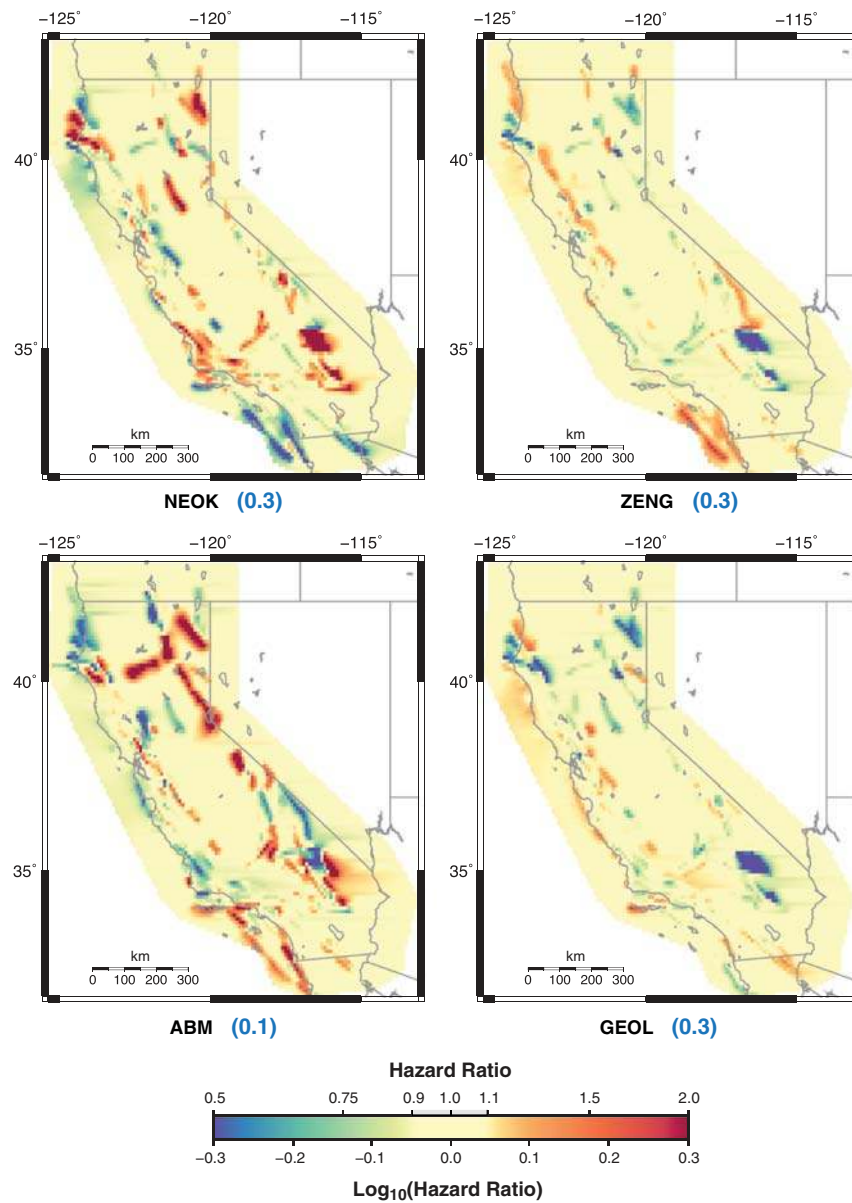


Figure 32. Branch-ratio maps showing the influence of each deformation model on 2%-in-50 year PGA. These ratios are obtained by averaging results over deformation-model subset branches and then dividing by the total average. Numbers in blue indicate the weights each model is given in UCERF3.

We are solving for more than 250,000 unknown rupture rates (f_r) with about 37,000 equality constraints (Appendix N, [Page et al., 2013](#)), so clearly individual solutions are nonunique. But what about metrics that are more relevant to seismic hazard, such as fault section participation MFDs and hazard curves? What about branch-averaged results versus what is resolved on individual branches? Here we quantify sensitivity to each of these, and conclude that convergence is not an issue for hazard-related metrics.

Individual Logic-Tree Branches. To test convergence for individual branches, we ran 200 simulated annealing inversions for the reference model (bold typeface options in Fig. 3). About 10,000 non-zero-rate (or above-water-level,

as defined in the [Characteristic Branches](#) section) ruptures are needed to fit the data on a single run, which is only ~4% of all possible ruptures. Figure 33 shows how this number varies as a function of the number of runs averaged. For example, averaging 10 runs, as done for each branch in UCERF3, increases the number to ~38,000 (~15% of ruptures), and averaging 200 runs increases the number to ~115,000 (~46%). This indicates that each solution samples a different set of ruptures in satisfying the data, as expected for an underdetermined problem. The roll off in Figure 33 suggests that an infinite number of runs might yield 50%–60% ruptures above water level, implying that half the ruptures are excluded on this particular branch; this is conjecture, however.

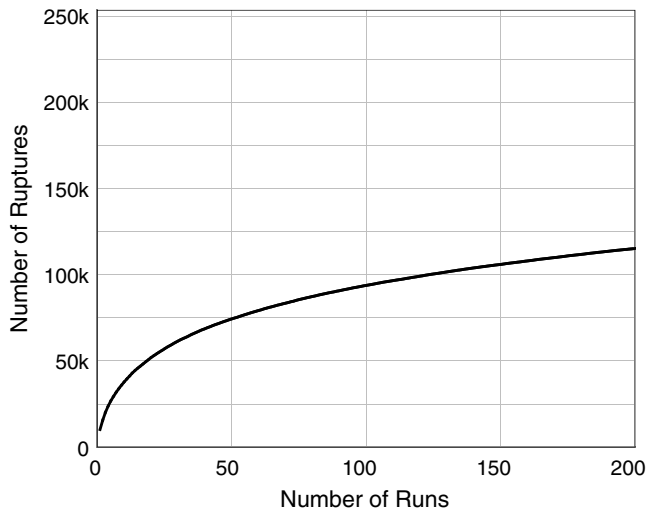


Figure 33. Number of above-water-level ruptures as a function of the number of simulated annealing runs averaged (for the reference branch). The maximum value on the y axis is the total number of possible ruptures (~250,000).

We attempted to quantify the number of runs needed to resolve mean rupture rates to some level of precision. However, interpretations were complicated by the fact that most rates are at water level (producing a bimodal distribution with a relatively high spike at the water level). Therefore, the mean rupture rates are difficult to resolve on individual branches, although we did find that those with higher rates are also better resolved.

Fault section participation MFDs represents a more appropriate metric for hazard. For a given magnitude event, standard PSHA for a site is relatively insensitive to rupture-endpoint differences—and completely so if the closest point to the rupture surface is the same. Figure 34 shows three participation MFDs obtained from the 200 reference branch runs. In terms of $M > 6.7$ rate variability among the 200 solutions, defined as the sample standard deviation s divided by the sample mean μ , these represent the worst, median, and best cases among all fault sections. The number of inversion runs N needed to obtain well-resolved average

estimates (those with the upper 95% confidence bound ($\mu + \frac{1.96s}{\sqrt{N}}$) within 10% of the mean) is

$$\mu + \frac{1.96s}{\sqrt{N}} \leq 1.1\mu,$$

in which $\frac{s}{\sqrt{N}}$ is the sample standard deviation of the mean. Solving for N , we obtain

$$N = \left(\frac{19.6s}{\mu} \right)^2.$$

With the sample statistics shown in Figure 34, the implied number of runs needed for well-resolved $M \geq 6.7$ event rates is 1294 for the worst case (Richfield), 9 for the median case (Puente Hills), and 1 for the best case (San Jacinto–Anza). The median is near the number of runs chosen for each branch in UCERF3 (10), which implies that roughly half our fault sections have well-resolved rates on individual branches. The worst case implies that, for some fault sections, many more runs would be needed to get well-resolved rates on individual branches. However, these turn out to be the least hazardous faults, because there is anti-correlation between variability and mean rate. For example, the worst case in Figure 34 also has the lowest rate of $M \geq 6.7$ events among all fault sections (with an average repeat time exceeding a million years). All fault sections that have average $M \geq 6.7$ repeat times less than 1000 years are well resolved, and the mean fractional uncertainty for all faults, weighted by the mean rate of each section, is 1.04.

We have also conducted this same analysis with respect to hazard curves. Specifically, from the 200 reference branch runs and for all test locations in Table 15, we computed sample means and standard deviations for 2in50 and 1in100 (1%-in-100-year) ground-motion levels for PGA, 5 Hz SA, 1 Hz SA, and 0.25 Hz SA. The 1in100, representing a 10,000-year return period, and 0.25 Hz SA were added to test more extreme circumstances (in which more uncertainty might be expected). In terms of variability (s/μ), the worst case is 2in50 5 Hz SA at Brookings (located just north of California on the Oregon coast). The fractional uncertainty for this worst case, $(\mu + \frac{1.96s}{\sqrt{N}})/\mu$, is 1.03 for $N = 10$, meaning the

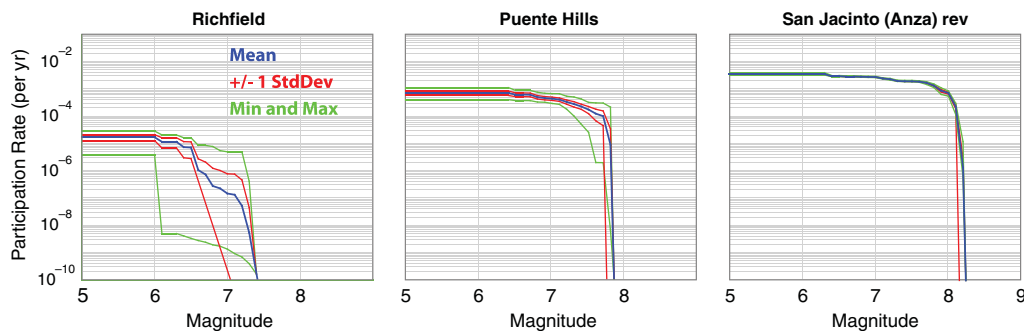


Figure 34. Cumulative participation MFD statistics for 200 simulated annealing runs on the reference branch. The fault section examples shown here represent the worst case, median case, and best case in terms of fractional uncertainty described in the text (which is proportional to the standard deviation [StdDev] divided by the mean).

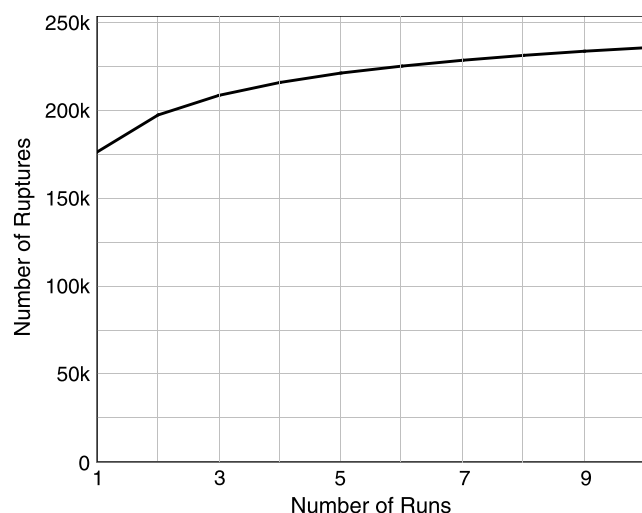


Figure 35. Number of above-water-level ruptures for branch-averaged solutions as a function of the number of simulated annealing runs on each branch (for *Fault Model 3.1*). The maximum value on the y axis is the total number of ruptures (~250,000).

upper 95% confidence bound is 3% above the mean with 10 runs. The median and best cases among this test had fractional uncertainties of 1.004 and 1.0001. These results imply that all customary hazard metrics are well resolved on individual branches given the 10 simulated annealing runs on each in UCERF3. The same conclusions can be drawn by examining the mean and range of hazard curves obtained among the 200 reference branch runs, which are available for each site under Hazard Convergence Tests in U3 Supplementary Figures (see [Data and Resources](#)). Note that the range plotted is the minimum and maximum among all branches, not a standard deviation-based confidence or range, which would require very thin lines to differentiate from the mean.

Branch-Averaged Results. The 1440 different logic-tree branches provide a great deal of additional averaging with respect to mean hazard, and we can use the 10 different runs for each branch to quantify how well such metrics are resolved for branch-averaged results. Figure 35 shows the number of ruptures above water level for branch-averaged results, as a function of how many runs on each branch are included. If only one simulated annealing run is used for each branch, about 176,000 events (76%) are above water level in the branch-averaged model. After averaging over all 10 runs, the full UCERF3 branch-averaged model has about 236,000 ruptures above water level (94%). Mean rupture rates are also much better resolved, but they are still difficult to interpret given bimodal distributions with respect to water levels.

Fault section participation MFDs are also much better resolved for branch average results. Sample means and standard deviations were computed from the 10 different sets, and fractional uncertainties for $M \geq 6.7$ event rates were computed for all fault sections. The worst case found is the Fitzhugh Creek

section, which has a fractional uncertainty of 1.07 (meaning the upper 95% confidence bound is 7% above the mean and would not be visually discernable if plotted as in Fig. 34). The median case implies that half the fault sections have upper 95% confidence bounds that are less than 0.5% above the mean. This implies that branch-averaged participation MFDs are well resolved on all fault sections in UCERF3.

Hazard metrics are extremely well resolved for branch averages. We generated a 2in50 PGA map for each of the 10 branch-averaged models, computed a sample mean and standard deviation from these 10, and then computed the fractional mean uncertainty at each map location. We then repeated this process for 1in100 PGA, 2in50 0.33 Hz SA, and 1in100 0.33 Hz SA. Among all the map sites, probability levels, and ground-motion parameters, the largest fractional uncertainty found was 1.004 (for a site near the northwest corner of California). This implies that for branch-averaged probabilistic ground-motion maps, including all those released by the USGS NSHMP, inversion nonuniqueness is negligible, and even one simulated annealing run on each branch would be adequate (because the 1440 logic-tree branches provide sufficient averaging on their own).

These conclusions apply not only to mean hazard, but to logic tree-implied percentiles as well. For each site listed in Table 15, we computed 2%, 16%, 84%, and 98% fractiles among the 10 sets of runs, for both PGA and 0.33 Hz SA, and for 2in50 and 1in100 probability levels. The worst case found was a fractional uncertainty of 1.006, meaning an upper 95% confidence bound that is just 0.6% above the mean percentile.

Equation-Set Weights. A thorough discussion of how the inversion equation-set weights were applied is given in Appendix N (Page *et al.*, 2013), which includes sensitivity tests conducted on the reference branch, where each equation-set weight was scaled up and down by a factor of 10. It is important to note that this range of weights is considered extreme in that fits to the other data are generally degraded to the point of model rejection. Example hazard curves from these tests are shown in Figure 36, where the range of values from alternative equation-set weights is small compared to that implied by alternative logic-tree branches (results for all sites are given under Hazard Equation-Set Weights Tests in U3 Supplementary Figures; see [Data and Resources](#)). We therefore conclude that accommodating a range of equation-set weights for each branch, which would need to be narrower than that tested, would not significantly change UCERF3 results.

Discussion

We begin this section with a summary of UCERF3 advantages (relative to UCERF2) and then discuss model limitations, both of which are important from a user's perspective. Table 16 lists some of the key assumptions under-

Table 16
Key Assumptions Made in UCERF3*

1. Simplified faults models derived from synthesized data (e.g., geologic mapping, microseismicity, well logs) provide an adequate approximation of fault structure and connectivity at depth.
2. Approximate 20-year GPS observations reflect long-term deformation rates.
3. Model-based transient corrections made to GPS data for past earthquakes and seasonal hydrologic processes are correct, and the apparent outliers that were removed represent measurement error and not real signals.
4. Backslip methods used in deformation models (Zeng, ABM) are adequate.
5. Faults that lack slip-rate constraints can reliably be assigned a categorical value based on recency of activity.
6. Depth extent of large ruptures is modeled appropriately by our scaling relationships.
7. Surface slip observations can be used to estimate slip at depth.
8. Surface creep mostly manifests as a seismogenic area reduction (rather than slip-rate reduction).
9. *Tapered* and/or *Boxcar* models of D_{sr} represent average slip along rupture, even for multifault events.
10. A generic model for the probability of seeing events in a paleoseismic trench applies to all sites (as opposed to site-specific models).
11. Large regions honor the Gutenberg–Richter magnitude–frequency distribution.
12. Magnitude completeness thresholds as function of time, space, and magnitude have been correctly estimated.
13. Seismicity rates vary with time over the course of historical and instrumental observations.
14. Higher-resolution smoothed seismicity maps are applicable to large, damaging earthquakes and for approximately 50-year time periods.
15. Our plausibility filter provides an adequate set of ruptures in terms of quantifying hazard and risk at all locations.

*Most assumptions have at least implicit or partial representation on our logic tree.

lying UCERF3, and we finish this section with possible future improvements.

Improvements Over UCERF2

The UCERF3 long-term model appears largely successful in terms of the original project goals: relaxing segmentation assumptions, incorporating multifault ruptures, fitting a broader range of data better, and sampling a wider range of epistemic uncertainties. This has been accomplished by implementing a system-level, grand inversion framework,

which has the following advantages over previous approaches:

- The rate of all earthquakes is solved for simultaneously.
- A wider range of viable solutions is provided (all those consistent with data).
- The inversion is conceptually simple (summarized in Table 6).
- Results are relatively reproducible (in terms of the influence of expert judgment).
- The framework is extensible (other constraints can easily be added).

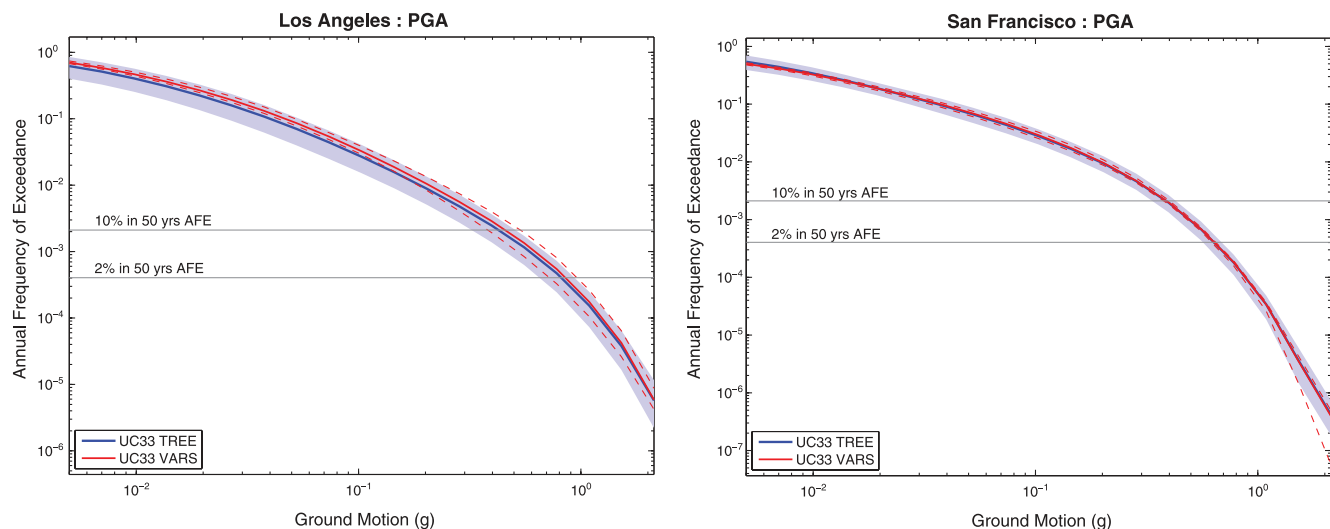


Figure 36. PGA hazard curves for the Los Angeles and San Francisco site listed in Table 15, obtained by varying equation-set weights on the UCERF3 reference branch, as summarized in the main text and detailed in Appendix N (Page *et al.*, 2013). The minimum and maximum curves among these tests are plotted with the red dashed lines, which can be compared with the range implied by alternative logic-tree branches (blue shaded region). The difference between the mean curves (red and blue solid lines) is not meaningful in this comparison. Results for other sites are given under Hazard Equation-Set Weights Tests in the U3 Supplementary Figures (see [Data and Resources](#)).

UCERF2 and previous models were largely prescriptive in terms of making assumptions about magnitude–frequency distributions and in treating different seismic sources separately (e.g., via segmentation assumptions). Although elegantly simple, this approach produces an overprediction of regional M 6.5–7 event rates and ignores the potential influence of multifault ruptures. The UCERF3 approach, in contrast, is more derivative in that fault MFDs are not assumed, but rather derived from a system-level inversion.

Results from the derivative approach are more difficult to understand, especially given a large increase in the number of possible fault-based ruptures (from ~8000 to 250,000). Whereas previous efforts had only to verify that assumed MFDs and rupture extents were correctly implemented, the grand inversion required the development of new tools for exploring the nature of solutions and their implications. UCERF3 also posed considerable computational challenges with respect to solving the large inverse problem thousands of times, and extensive hazard calculations were required to understand the potential influence of solution nonuniqueness. All of these challenges were new to UCERF3 and not fully appreciated at the beginning of the project.

Although the grand-inversion approach is not free of subjectivity, it does provide a more comprehensive framework for checking overall consistency between, and therefore balancing the influence of, different experts. Opinions of the latter were solicited through an unprecedented set of technical, consensus-building workshops (Table 3), with a particularly good example being the series of fault-by-fault review meetings. These not only provided an important reality check for individual faults (not needed in the prescriptive approach taken previously), but also allowed comparisons with new, unpublished data and provided a record of faults needing further scrutiny in future efforts (described in the “ReviewComments” sheet of the U3 Fault Section Data file; see [Data and Resources](#)).

UCERF3 also constitutes an improvement in terms of epistemic uncertainty representation. For example, UCERF2 had only a single logic-tree branch in areas dominated by gridded seismicity (e.g., Sacramento). UCERF3 now has eighteen such branches given the new alternatives for off-fault maximum magnitude, the spatial distribution of seismicity, and the total regional rate of events. Epistemic uncertainties have also been added for fault-based ruptures, including a wider range of slip rates (deformation models), new scaling relationships that represent the possibility that larger ruptures extend below the depth of microseismicity, and alternatives for how average slip varies along strike.

The geologic databases have been substantially revised and expanded, including statewide fault models (Appendix A, [Dawson, 2013](#)), geologic slip data (Appendix B, [Dawson and Weldon, 2013](#)), and paleoseismic recurrence rates (Appendix G, [Weldon, Dawson, and Madden, 2013](#)). Fault polygons have been introduced to associate fault surfaces with deformation volumes (Appendix O, [Powers and Field, 2013](#)). New datasets have been compiled, including

GPS velocities (Appendix C, [Parsons et al., 2013](#)) and displacement-per-event data (Appendix R, [Madden et al., 2013](#)). Geologic and geodetic data have been jointly inverted for a suite of statewide deformation models (Appendix C, [Parsons et al., 2013](#)).

The data on fault creep rates have been greatly enlarged using InSAR measurements, and a new approach has been introduced for extrapolating surface creep rates to average creep rates across the fault surface (Appendix D, [Weldon, Schmidt, et al., 2013b](#)). The probability of detecting ground ruptures at paleoseismic sites has been estimated (Appendix I, [Weldon and Biasi, 2013](#)), and the interpretation of paleoseismic interevent times has been updated (Appendix H, [Biasi, 2013](#)). A revised earthquake catalog (Appendix K, [Felzer, 2013a](#)) has been used to constrain magnitude–frequency distributions (Appendix L, [Felzer, 2013b](#)), to develop a new model of smoothed seismicity (Appendix M, [Felzer, 2013c](#)), and to reconsider the issue of empirically adjusted seismicity rates (Appendix Q, [Felzer, 2013d](#)). Scaling relationships for magnitude and depth of rupture have been reexamined (Appendix E, [Shaw, 2013b](#)), and a dataset relating rupture length to displacement has been developed (Appendix F, [Biasi, Weldon, and Dawson, 2013](#)).

The new deformation models are particularly noteworthy. In addition to a relatively pure *Geologic* model (Appendix B, [Dawson and Weldon, 2013](#)), we have three that are based on kinematically consistent inversions of geodetic and geologic data (Appendix C, [Parsons et al., 2013](#)). This is in contrast to the previous approach, which relied on expert judgment to broker discrepancies between geologic and geodetic observations. The geodetic signal is persistently flat across the southern SAF system, causing models that utilize these data to seek slip in places other than the SAF. The signal expected from geology and paleoseismology, on the other hand, would have a sharper change in observed velocity across the southern SAF (as it is in northern California, although the signal is muted compared to geology there, too). This is a data-driven result, but we do not know how well the short-term GPS data reflect the long-term slip rates; the geologic and paleoseismic constraints suggest that they may not be representative of 10^3 – 10^5 year time scales. Finally, the kinematically consistent deformation models have also provided estimates of off-fault deformation, allowing us to retire the less refined type C zones utilized in previous models.

Observations have been compiled to constrain fault-to-fault rupture probabilities (Appendix J, [Biasi, Parsons, et al., 2013](#)), which not only guided the development of our rupture plausibility filter (Appendix T, [Milner et al., 2013](#)), but will also constitute an important resource for further testing of, and improving upon, UCERF3. With respect to the grand inversion, Appendix N ([Page et al., 2013](#)) documents the simulated annealing algorithm, including parallelization; sensitivity tests, including some based on synthetic datasets; the tuning and testing of final constraint weights; and how well each type of data is fit by final models. Appendix N ([Page et al., 2013](#)) also provides additional implementation details,

such as the treatment of creep and how multifault-rupture statistics compare with various types of observations.

The system-level aspect of the grand inversion makes it well suited for hypothesis testing. Perhaps the best and most important example of this is with respect to the *Gutenberg–Richter* branches, where the hypothesis that each fault nucleates such a distribution of events cannot match all data—not even close. The inversion implies that doing so would require one or more of the following to fall outside the current bounds of consensus-level acceptability: (1) a higher degree of creep both on and off faults, (2) higher long-term rate of earthquakes over the whole region (and significant temporal variability on faults such as the SAF), (3) more fault connectivity throughout the state (e.g., $M \sim 8$ anywhere), and/or (4) lower shear rigidity.

The obvious alternative is that the GR hypothesis does not apply at the local scale of individual faults, which would make reports of the death of the *Characteristic* model (Kagan *et al.*, 2012) greatly exaggerated. Either way, the GR hypothesis is clearly inconsistent with the current UCERF3 modeling framework, which is why it was given zero weight on the logic tree. If the GR hypothesis turns out to be correct, then the explanation for current discrepancies will be equally profound scientifically and quite consequential with respect to hazard. The main point here is that the grand inversion provides an ideal framework for testing this and other such hypotheses, which will not only further our scientific understanding, but will also allow us to identify and focus resources on the questions that matter. Eliminating model options will also reduce epistemic uncertainties and thereby improve hazard and loss assessments.

Finally, the entire UCERF3 development has been followed closely by a participatory scientific review panel, from reviewing original project plans, attending the various meetings and workshops (Table 2), reviewing all appendixes (Table 3), and scrutinizing four different versions of UCERF3. We also hosted two workshops at which results were presented to the broader scientific and engineering communities (Table 2). Furthermore, UCERF3 was evaluated by an NSHMP steering committee, which recommended that it be used in the 2014 national maps.

Model Limitations

In spite of improvements, UCERF3 is still an approximation of the system. For example, we continue to divide between on-fault and off-fault ruptures, whereas nature will surely violate these model boundaries. Our plausibility filter for multifault ruptures also has arbitrary cutoffs, such as the 5 km jumping threshold between faults, and we currently lack any improbability constraint. These limitations, coupled with the fact that the relative geometry of neighboring faults is poorly known at depth, imply we have most certainly included some unlikely ruptures and excluded some that are plausible. In addition, the multifault rupture rates coming out of the grand inversion depend both on how average slip

is distributed along such ruptures (D_{sr}) and how slip rates transition between faults, neither of which is well known.

Some reviewers expressed dissatisfaction with the non-uniqueness of UCERF3 solutions, exemplified by the fact that single inversions leave only about 4% of ruptures above water-level rates. In an attempt to remedy this, we tried applying an additional constraint to, in essence, make the rate of similar ruptures equal. However, doing so effectively made the inversion nonlinear and therefore prohibitively slow in comparison to simply averaging more inversion runs. Each simulated annealing solution can be thought of as one sample among an infinite population of viable models or even as a realization of events for some time period. We do not see this as a problem, but rather an improvement in terms of acknowledging nonuniqueness and sampling a wider range of models; the problem is inherently underdetermined unless you impose segmentation. Fortunately, solution non-uniqueness has a negligible impact on hazard estimates, because results depend more on the participation MFD of faults and much less so on rupture-endpoint details.

Concerns were voiced regularly that our large number of fault-based ruptures was going to be a problem in terms of PSHA computation time. Not only have those concerns turned out to be unfounded (OpenSHA calculation time is about the same as it was for UCERF2, in part because of the increased speed of computers), but our analysis also demonstrates that use of a single inversion solution might be a legitimate way of down sampling the entire event set. Doing so properly, however, will vary between different types of hazard and loss studies, so we do not attempt any generic down-sampling advice here.

Another concern raised during review is whether relaxing segmentation has reduced epistemic uncertainty. For example, the Cucamonga fault section has gone from a relatively high rate of moderate-size events ($M \sim 6.7$) to a lower and relatively uniform rate of events out to $M 8$ (Fig. 25). Technically speaking, this has not reduced epistemic uncertainty, but rather changed the behavior from one extreme to perhaps another. And, while all such cases that have had a perceptible influence on hazard were deemed an improvement at our fault-by-fault review meetings, we acknowledge that there may be some areas in which UCERF3 lacks an adequate characteristic alternative. For example, and in spite of the theoretical modeling of Anderson *et al.* (2003), it is possible that Cucamonga never ruptures with neighboring faults.

To address this possibility, we were asked to explore an inversion that imposes UCERF2 segmentation throughout the system. While we know this would not be correct everywhere, it might be more correct on certain faults. BSSC deadlines prevented us from doing this for UCERF3. Furthermore, one does not need the grand inversion to implement a characteristic model (that would be overkill), and there is no guarantee that UCERF2 is correct with respect to segmentation details anyway. Potential cases like Cucamonga should therefore be handled on a case-by-case basis

(e.g., via site-specific analysis). That being said, Figure 21 implies that we are not grossly overpredicting the rate of multifault ruptures (see also the multifault evaluation metrics in Appendix N, [Page et al., 2013](#)), so we believe UCERF3 is doing better overall and that UCERF2 is a relatively poor approximation in more areas of California.

There is also the possibility that UCERF3 lacks connectivity in areas where it exists, which is another form of epistemic uncertainty left out of the model. Given all these limitations and assumptions, one might deem the grand inversion overly sophisticated or premature. However, we currently lack any alternative for relaxing segmentation and including multifault ruptures. Physics-based earthquake simulators ([Ward, 2000](#); [Rundle et al., 2006](#); [Dieterich and Richards-Dinger, 2010](#); [Tullis et al., 2012](#)) are a promising solution. However, they currently suffer even more from some uncertainties, such as the unknown proximity of faults at depth. Simulator tuning procedures are also needed to match data (e.g., paleoseismic event rates, fault-jumping statistics), and the propagation of epistemic uncertainties poses considerable computational challenges.

We also emphasize that UCERF3 is heavily weighted toward UCERF2, most notably in terms of the *Characteristic UCERF2 Constrained* branch being given exclusive weight, but also in terms of the various limits on multifault ruptures. For example, both *Slip Along Rupture* (D_{sr}) models put high amounts of slip at the midpoint along strike, as compared to the characteristic-slip model ([WGCEP, 1995](#)), so rupture rates are consequently more limited by the slip-rate constraint. These impositions explain why UCERF3 underestimates the observed frequency of multifault ruptures. The analysis in Appendix N ([Page et al., 2013](#)) also implies that we are overfitting much of our data (as did UCERF2 and previous models). All of these factors further limit the range of UCERF3 models.

A final UCERF3 limitation is with respect to fitting some of the paleoseismic data and slip rates on the southern SAF (Fig. 20). As noted, these constraints can be fit perfectly well if the regional MFD constraint is relaxed. Doing so, however, brings back the overprediction of moderate event rates. This trade-off exemplifies the potential long reach of inversion constraints, in which the rate in one location can be influenced by conditions far away. While some reviewers regarded this as physically problematic, others saw it as an appropriate way to achieve system-level balance. With respect to the SAF, some branches do fit the data better, but on average our rates are about 25% low compared to paleoseismic rates. Therefore, while the hazard implied by the SAF has changed little since UCERF2, it is currently underestimated if the latest paleoseismic interpretations are correct.

Future Improvements

The extensibility of the grand-inversion platform will lend itself to several potential improvements. For example, quantification of multifault rupture statistics via observations, dynamic rupture modeling, and physics-based simula-

tions could allow us to improve upon the UCERF3 plausibility filter, both in terms of representing epistemic uncertainties and the addition of improbability constraints. Some other possible improvements include the following (in no particular order):

- Apply deformation-model based options for *Off-Fault Spatial Seis PDF*.
- Explore inversions with UCERF2 segmentation imposed.
- Explore a wider range of models by relaxing the UCERF2 fault section MFD constraint.
- Explore a wider range of models by not overfitting data as much.
- Explore the use of inversion data fits for a *posteriori* adjustment of logic-tree branch weights.
- Try to implement an inversion constraint that will achieve more equality among rupture rates (fewer water-level ruptures).
- Further explore the possibility that points on faults nucleate a Gutenberg–Richter distribution of events.
- Apply more customized and targeted inversion-constraint weights in order to fit certain data better (e.g., on the southern SAF).
- Investigate the discrepancy between off-fault moment rates predicted by the deformation models and those implied by the grand-inversion models.
- Address issues identified for particular faults at the fault-by-fault review meetings (described in the “ReviewComments” sheet of the U3 Fault Section Data file; see [Data and Resources](#)).
- Study creep manifestation and implications further, especially given the discrepancy between off-fault seismic moment rates between UCERF3 and those predicted by the deformation models (Fig. 24).
- Coordinate and integrate fault zone polygon definitions with future deformation model developments.
- Investigate how the characteristic slip model (e.g., [Hecker et al., 2013](#)) could be incorporated into the inversion framework, given that we lack observed estimates on most faults.
- Explore model-based inferences that average slip, for a given length rupture, goes down with increasing number of fault-to-fault jumps (Appendix F; [Biasi, Weldon, and Dawson, 2013](#)).
- Develop and use site-specific models for the probability of seeing events in a paleoseismic trench.
- Explore the applicability of recent seismicity to 50-year forecasts.
- Explore the applicability of different smoothed seismicity algorithms in forecasting large, damaging events and for different forecast durations.

Conclusions and Recommendations

We believe UCERF3 represents a considerable improvement over UCERF2. In addition to the methodological en-

hancements represented by the grand inversion, we have expanded the range of epistemic uncertainty representation. Hazard calculations allow us to conclude that the most influential uncertainties are deformation models (slip rates), the smoothed seismicity algorithm, the total regional rate of events, and scaling relationships. All of these new branches have produced significant and important changes in mean hazard estimates. New faults have also been added to the model, which produce some of the biggest hazard differences relative to UCERF2. The apparent overprediction of M 6.5–7 event rates in UCERF2 has been removed, and UCERF3 includes multifault ruptures like those seen in nature.

The added epistemic uncertainties are generally more influential than the inclusion of multifault ruptures, with at least two notable exceptions identified. However, these conclusions are with respect to traditional NSHMP hazard metrics and may not apply to, for example, statewide loss estimates (in which large, rare events may be more influential). It will therefore be important that practitioners carefully assess the applicability of this model in the context of their particular applications, as results may be sensitive to aspects of the model that differ from the influential factors inferred here. This is particularly true for site-specific studies, in which the nearby influential fault(s) may not have adequate epistemic uncertainty representation in UCERF3.

While the addition of epistemic uncertainties in UCERF3 is mentioned as an accomplishment, this also means we have not yet reached the point at which further study reduces the range of viable models. In fact, we have argued that UCERF3 may still be too limited, implying that a broader range of models could be forthcoming. That this conclusion is being made for one of the most data-rich areas on Earth implies that epistemic uncertainties are likely underestimated elsewhere.

Although the inversion is conceptually simple and extensible, the overall framework and implementation is far more involved than for previous models. UCERF3 relies on an extensive object-oriented programming framework, versus an Excel spreadsheet as used by WGCEP, 1995. However, this will be true of any system-level model, and the only consolation we can provide is the fact that everything is open source and freely available.

The grand inversion has proven to be a powerful tool for quantifying the influence and consistency of various constraints, for exploring a range of models, and for testing hypotheses. There is considerable interactive complexity in the system, however, and further study will be needed to fully understand trade-offs between the various inversion constraints. Such analyses may support applying *a posteriori* weights to UCERF3 branches in the future.

Data and Resources

All calculations were made using OpenSHA (<http://www.OpenSHA.org>, last accessed January 2014; Field *et al.*, 2003) during 2012 and 2013, which in turn utilizes the fol-

lowing for making plots: Generic Mapping Tools (<http://gmt.soest.hawaii.edu>, last accessed January 2012) and JFreeChart (<http://www.jfree.org/jfreechart/>, last accessed March 2012).

The U3 Fault Section Data is available at http://pubs.usgs.gov/of/2013/1165/data/ofr2013-1165_FaultSectionData.xlsx (last accessed January 2014). The U3 Pre-Inversion Analysis Table is available at http://pubs.usgs.gov/of/2013/1165/data/ofr2013-1165_PreInversionAnalysisTable.xlsx (last accessed January 2014).

U3 Supplementary Figures (subdirectories of http://pubs.usgs.gov/of/2013/1165/data/UCERF3_SupplementalFiles/UCERF3.3) include the following (all of which were last accessed January 2014): Paleoseismic Data Fits (http://pubs.usgs.gov/of/2013/1165/data/UCERF3_SupplementalFiles/UCERF3.3/Model/PaleoAndSlipRateFits), Fault Section MFDs (Magnitude–Frequency Distributions) (http://pubs.usgs.gov/of/2013/1165/data/UCERF3_SupplementalFiles/UCERF3.3/Model/FaultMFDs), Fault Section Participation Maps (http://pubs.usgs.gov/of/2013/1165/data/UCERF3_SupplementalFiles/UCERF3.3/Model/FaultParticipation), Implied Segmentation (http://pubs.usgs.gov/of/2013/1165/data/UCERF3_SupplementalFiles/UCERF3.3/Model/FaultSegmentation), Hazard Curves (http://pubs.usgs.gov/of/2013/1165/data/UCERF3_SupplementalFiles/UCERF3.3/Hazard/HazardCurves), Hazard Maps (http://pubs.usgs.gov/of/2013/1165/data/UCERF3_SupplementalFiles/UCERF3.3/Hazard/HazardMaps), Branch Ratio Hazard Maps (http://pubs.usgs.gov/of/2013/1165/data/UCERF3_SupplementalFiles/UCERF3.3/Hazard/BranchRatios), Hazard Convergence Tests (http://pubs.usgs.gov/of/2013/1165/data/UCERF3_SupplementalFiles/UCERF3.3/Hazard/InversionTests/Convergence), and Hazard Equation-Set Weights Tests (http://pubs.usgs.gov/of/2013/1165/data/UCERF3_SupplementalFiles/UCERF3.3/Hazard/InversionTests/EquationSetWeights).

Acknowledgements

The UCERF3 Scientific Review Panel (SRP), which was convened at the beginning of this project, thoughtfully reviewed the many model components and several cycles of WGCEP reports, including this final report and its appendixes. We are especially indebted to the SRP chair, William Ellsworth, who provided WGCEP with outstanding scientific advice throughout the study, and to SRP member, Art Frankel, whose reviews and critiques of the methodology were particularly important in model verification. Bob Anderson and Badie Rowshandel provided very valuable feedback on behalf of the California Earthquake Authority. Helpful reviews were also provided by Mark Petersen and the U.S. Geological Survey (USGS) National Seismic Hazard Mapping Program's Steering Committee, chaired by John Anderson, as well as the California and National Earthquake Prediction Evaluation Councils (CEPEC and NEPEC). We thank many workshop participants for their contributions to the project and their support as UCERF3 came into focus.

We are very grateful to Tran Huynh for her substantial efforts in organizing WGCEP activities and in editing the UCERF reports and appendixes, and to John McRaney for his financial management of the project. The Management Oversight Committee helped WGCEP with project guidance and requisite resources, and Keith Knudson shepherded the main report and appendixes through the USGS publication process. The Southern California

Earthquake Center (SCEC) Community Modeling Environment, University of Southern California (USC) Center for High-Performance Computing and Communications, and the Texas Advanced Computing Center provided access to the high-performance computing resources critical to the grand inversion and hazard calculations. Finally, we thank James Dieterich, two anonymous reviewers, and Associate Editor Ivan Wong for their very helpful reviews.

This study was sponsored by the California Earthquake Authority, the USGS, the California Geological Survey, and SCEC. SCEC is supported in part by the National Science Foundation under Cooperative Agreement EAR-1033462 and by the USGS under Cooperative Agreement G12AC20038. This report is USGS Open-File Report 2013–1165, SCEC contribution number 1792, and California Geological Survey publication number 228.

References

- Algermissen, S. T., D. M. Perkins, P. C. Thenhaus, S. L. Hanson, and B. L. Bender (1982). Probabilistic estimates of maximum acceleration and velocity in rock in the contiguous United States, *U.S. Geol. Surv. Open-File Rept.* 82-1033.
- Anderson, G., B. Aagaard, and K. Hudnut (2003). Fault interactions and large complex earthquakes in the Los Angeles area, *Science* **203**, 1946–1949, doi: [10.1126/science.1090747](https://doi.org/10.1126/science.1090747).
- Andrews, D. J., and E. Schwerer (2000). Probability of rupture of multiple fault segments, *Bull. Seismol. Soc. Am.* **90**, 1498–1506.
- Biasi, G. P. (2013). Appendix H: Maximum likelihood recurrence intervals for California paleoseismic sites, *U.S. Geol. Surv. Open-File Rept. 2013-1165-H*, and *California Geol. Surv. Special Rept. 228-H*.
- Biasi, G. P., and R. J. Weldon (2009). San Andreas fault rupture scenarios from multiple paleoseismic records: Stringing pearls, *Bull. Seismol. Soc. Am.* **99**, 471–498, doi: [10.1785/0120080287](https://doi.org/10.1785/0120080287).
- Biasi, G. P., T. Parsons, R. J. Weldon II, and T. E. Dawson (2013). Appendix J: Fault-to-fault rupture probabilities, *U.S. Geol. Surv. Open-File Rept. 2013-1165-J*, and *California Geol. Surv. Special Rept. 228-J*.
- Biasi, G. P., R. J. Weldon II, and T. E. Dawson (2013). Appendix F: Distribution of slip in ruptures, *U.S. Geol. Surv. Open-File Rept. 2013-1165-F*, and *California Geol. Surv. Special Rept. 228-F*.
- Bird, P. (2009). Long-term fault slip rates, distributed deformation rates, and forecast of seismicity in the western United States from joint fitting of community geologic, geodetic, and stress direction data sets, *J. Geophys. Res.* **114**, no. B11403, doi: [10.1029/2009JB006317](https://doi.org/10.1029/2009JB006317).
- Black, N. M., and D. D. Jackson (2008). Probability of multifault rupture, *Bull. Seismol. Soc. Am.* **98**, 3017–3024, doi: [10.1785/0120070271](https://doi.org/10.1785/0120070271).
- Box, G. E. P. (1979). Robustness in the strategy of scientific model building, in *Robustness in Statistics*, R. L. Launer and G. N. Wilkinson (Editors), Academic Press, New York.
- Brune, J. N., A. Anooshehpour, M. D. Purvance, and R. J. Brune (2006). Band of precariously balanced rocks between the Elsinore and San Jacinto, California, fault zones: Constraints on ground motion for large earthquakes, *Geology* **34**, 137–140.
- Building Seismic Safety Council (BSSC) (2009). *NEHRP Recommended Seismic Provisions for New Building and Other Structures*, Federal Emergency Management Agency, Publication Number P-750, <http://www.fema.gov/media-library/assets/documents/18152/> (last accessed January 2014).
- Cornell, C. A. (1968). Engineering seismic risk analysis, *Bull. Seismol. Soc. Am.* **58**, 1583–1606.
- Cua, G., M. Fischer, T. Heaton, and S. Wiemer (2009). Real-time performance of the Virtual Seismologist earthquake early warning algorithm in southern California, *Seismol. Res. Lett.* **80**, 740–747, doi: [10.1785/gssrl.80.5.740](https://doi.org/10.1785/gssrl.80.5.740).
- Dawson, T. E. (2013). Appendix A: Updates to the California reference fault parameter database: UCERF3 fault models 3.1 and 3.2, *U.S. Geol. Surv. Open-File Rept. 2013-1165-A*, and *California Geol. Surv. Special Rept. 228-A*.
- Dawson, T. E., and R. J. Weldon II (2013). Appendix B: Geologic slip-rate data and geologic deformation model, *U.S. Geol. Surv. Open-File Rept. 2013-1165-B*, and *California Geol. Surv. Special Rept. 228-B*.
- Dieterich, J. H., and K. B. Richards-Dinger (2010). Earthquake recurrence in simulated fault systems, *Pure Appl. Geophys.* **167**, 1087–1184.
- Duan, B. C., and D. D. Oglesby (2006). Heterogeneous fault stresses from previous earthquakes and the effect on dynamics of parallel strike-slip faults, *J. Geophys. Res.* **111**, no. B0, 5309–5324.
- Felzer, K. R. (2007). Calculating California seismicity rates, *U.S. Geol. Surv. Open-File Rept. 2007-1437-I*.
- Felzer, K. R. (2013a). Appendix K: The UCERF3 earthquake catalog, *U.S. Geol. Surv. Open-File Rept. 2013-1165-K*, and *California Geol. Surv. Special Rept. 228-K*.
- Felzer, K. R. (2013b). Appendix L: Estimate of the Seismicity Rate and Magnitude–Frequency Distribution in California from 1850 to 2011, *U.S. Geol. Surv. Open-File Rept. 2013-1165-L*, and *California Geol. Surv. Special Rept. 228-L*.
- Felzer, K. R. (2013c). Appendix M: Adaptive smoothed seismicity model, *U.S. Geol. Surv. Open-File Rept. 2013-1165-M*, and *California Geol. Surv. Special Rept. 228-M*.
- Felzer, K. R. (2013d). Appendix Q: The empirical model, *U.S. Geol. Surv. Open-File Rept. 2013-1165-Q*, and *California Geol. Surv. Special Rept. 228-Q*.
- Felzer, K. R., R. E. Abercrombie, and G. Ekström (2004). A common origin for aftershocks, foreshocks, and multiplets, *Bull. Seismol. Soc. Am.* **94**, 88–99.
- Field, E. H. (2007). Overview of the Working Group for the Development of Regional Earthquake Likelihood Models (RELM), *Seismol. Res. Lett.* **78**, 7–16.
- Field, E. H. (2012). Aftershock statistics constitute the strongest evidence for elastic relaxation in large earthquakes—Take 2, (abstract), *Annual Meeting of the Seismological Society of America*, San Diego, California, 17–19 April 2012.
- Field, E. H., and M. T. Page (2011). Estimating earthquake-rupture rates on a fault or fault system, *Bull. Seismol. Soc. Am.* **101**, 79–92, doi: [10.1785/0120100004](https://doi.org/10.1785/0120100004).
- Field, E. H., G. P. Biasi, P. Bird, T. E. Dawson, K. R. Felzer, D. D. Jackson, K. M. Johnson, T. H. Jordan, C. Madden, A. J. Michael, K. R. Milner, M. T. Page, T. Parsons, P. M. Powers, B. E. Shaw, W. R. Thatcher, R. J. Weldon II, and Y. Zeng (2013). Uniform California Earthquake Rupture Forecast, version 3 (UCERF3)—The time-independent model, *U.S. Geol. Surv. Open-File Rept. 2013-1165*, and *California Geol. Surv. Spec. Rept. 228*, <http://pubs.usgs.gov/of/2013/1165/> (last accessed January 2014).
- Field, E. H., T. E. Dawson, K. R. Felzer, A. D. Frankel, V. Gupta, T. H. Jordan, T. Parsons, M. D. Petersen, R. S. Stein, R. J. Weldon II, and C. J. Wills (2009). Uniform California Earthquake Rupture Forecast, Version 2 (UCERF 2), *Bull. Seismol. Soc. Am.* **99**, 2053–2107, doi: [10.1785/0120080049](https://doi.org/10.1785/0120080049).
- Field, E. H., T. H. Jordan, and C. A. Cornell (2003). OpenSHA: A developing community-modeling environment for seismic hazard analysis, *Seismol. Res. Lett.* **74**, 406–419.
- Finzi, Y., and S. Langer (2012). Damage in step-overs may enable large cascading earthquakes, *J. Geophys. Res.* **39**, L16303.
- Frankel, A. (1995). Mapping seismic hazard in the central and eastern United States, *Seismol. Res. Lett.* **66**, 8–21.
- Frankel, A. D., and M. D. Petersen (2013). Appendix P: Models of earthquake recurrence and down-dip edge of rupture for the Cascadia subduction zone, *U.S. Geol. Surv. Open-File Rept. 2013-1165-P*, and *California Geol. Surv. Special Rept. 228-P*.
- Frankel, A., C. Mueller, T. Barnhard, D. Perkins, E. Leyendecker, N. Dickman, S. Hanson, and M. Hopper (1996). National Seismic-Hazard Maps: Documentation June 1996, *U.S. Geol. Surv. Open-File Rept. 96-532*.
- Frankel, A. D., M. D. Petersen, C. S. Mueller, K. M. Haller, R. L. Wheeler, E. V. Leyendecker, R. L. Wesson, S. C. Harmsen, C. H. Cramer, D. M. Perkins, and K. S. Rukstales (2002). Documentation for the 2002 up-

- date of the National Seismic Hazard Map, *U.S. Geol. Surv. Open-File Rept.* 2002-420.
- Gardner, J. K., and L. Knopoff (1974). Is the sequence of earthquakes in southern California with aftershocks removed Poissonian? *Bull. Seismol. Soc. Am.* **64**, 1363–1367.
- Granville, V., M. Krivanek, and J.-P. Rasson (1994). Simulated annealing: A proof of convergence, *IEEE Trans. Patt. Anal. Machine Intell.* **16**, 652–656, doi: [10.1109/34.295910](https://doi.org/10.1109/34.295910).
- Hammond, W. C., G. Blewitt, and C. Kreemer (2011). Block modeling of crustal deformation of the northern Walker Lane and Basin and Range from GPS velocities, *J. Geophys. Res.* **166**, no. B04402, doi: [10.1029/2010JB007817](https://doi.org/10.1029/2010JB007817).
- Hanks, T. C., and W. H. Bakun (2008). M -log A observations of recent large earthquakes, *Bull. Seismol. Soc. Am.* **98**, 490.
- Harris, R. A., and S. M. Day (1993). Dynamics of fault interaction—parallel strike-slip faults, *J. Geophys. Res.* **98**, 4461–4472.
- Harris, R. A., R. J. Archuleta, and S. M. Day (1991). Fault steps and the dynamic rupture process: 2-D numerical simulations of a spontaneously propagating shear fracture, *Geophys. Res. Lett.* **18**, 893–896.
- Hauksson, E., J. Stock, K. Hutton, Y. Wenzheng, J. A. Vidal-Villegas, and H. Kanamori (2011). The 2010 M_w 7.2 El Mayor-Cucapah earthquake sequence, Baja California, Mexico and southernmost California, USA: Active seismotectonics along the Mexican Pacific margin, *Pure Appl. Geophys.* **168**, 1255–1277, doi: [10.1007/s00024-010-0209-7](https://doi.org/10.1007/s00024-010-0209-7).
- Hecker, S., N. A. Abrahamson, and K. E. Wooddell (2013). Variability of displacement at a point: Implications for earthquake-size distribution and rupture hazard on faults, *Bull. Seismol. Soc. Am.* **103**, 651–674, doi: [10.1785/0120120159](https://doi.org/10.1785/0120120159).
- Helmstetter, A., Y. Y. Kagan, and D. D. Jackson (2007). High-resolution time-independent grid-based forecast for $M \geq 5$ earthquakes in California, *Seismol. Res. Lett.* **78**, 78–86.
- Holmes, R. R., Jr., L. M. Jones, J. C. Eidenshink, J. W. Godt, S. H. Kirby, J. J. Love, C. A. Neal, N. G. Plant, M. L. Plunkett, C. S. Weaver, A. Wein, and S. C. Perry (2013). U.S. Geological Survey natural hazards science strategy—Promoting the safety, security, and economic well-being of the nation, *U.S. Geol. Surv. Circular 1383-F*, 79 pp.
- Jenny, S., S. Goes, D. Giardini, and H.-G. Kahle (2004). Earthquake recurrence parameters from seismic and geodetic strain rates in the eastern Mediterranean, *Geophys. J. Int.* **157**, 1331–1347, doi: [10.1111/j.1365-246X.2004.02261.x](https://doi.org/10.1111/j.1365-246X.2004.02261.x).
- Johnson, K. M., and J. Fukuda (2010). New methods for estimating the spatial distribution of locked asperities and stress-driven interseismic creep on faults with application to the San Francisco Bay area, California, *J. Geophys. Res.* **115**, no. B12408, doi: [10.1029/2010JB007703](https://doi.org/10.1029/2010JB007703).
- Jordan, T. H., Y.-T. Chen, P. Gasparini, R. Madariaga, I. Main, W. Marzocchi, G. Papadopoulos, G. Sobolev, K. Yamaoka, and J. Zschau (2011). Operational earthquake forecasting: State of knowledge and guidelines for implementation, final report of the International Commission on Earthquake Forecasting for Civil Protection, *Ann. Geophys.* **54**, no. 4, 315–391, doi: [10.4401/ag-5350](https://doi.org/10.4401/ag-5350).
- Kagan, Y. Y. (2002a). Seismic moment distribution revisited: I, Statistical Results, *Geophys. J. Int.* **148**, 520–541.
- Kagan, Y. Y. (2002b). Seismic moment distribution revisited: II, Moment conservation principle, *Geophys. J. Int.* **149**, 731–754.
- Kagan, Y. Y., and D. D. Jackson (2013). Tohoku earthquake: A surprise? *Bull. Seismol. Soc. Am.* **103**, 1181–1194.
- Kagan, Y. Y., D. D. Jackson, and R. J. Geller (2012). Characteristic earthquake model, 1884–2011, RIP, *Seismol. Res. Lett.* **83**, 951–953, doi: [10.1785/0220120107](https://doi.org/10.1785/0220120107).
- Kaiser, A., C. Holden, J. Beavan, D. Beetham, R. Benites, A. Celentano, D. Collett, J. Cousins, M. Cubrinovski, G. Dellow, P. Denys, E. Fielding, B. Fry, M. Gerstenberger, R. Landgridge, C. Massey, M. Motagh, N. Pondard, G. McVerry, J. Ristau, M. Stirling, J. Thomas, S. R. Uma, and J. Zhao (2012). The M_w 6.2 Christchurch earthquake of February 2011: Preliminary report, *New Zeal. J. Geol. Geophys.* **55**, 67–90, doi: [10.1080/00288306.2011.641182](https://doi.org/10.1080/00288306.2011.641182).
- Knuepfer, P. L. K. (1989). Implications of the characteristics of the endpoints of historical surface fault ruptures for the nature of fault segmentation, *U.S. Geol. Surv. Open-File Rept.* 89-315, 193–228.
- Lawson, C. L., and D. J. Hanson (1974). *Solving Least Squares Problems*, Prentice-Hall, Englewood Cliffs, New Jersey.
- Lettis, W., J. Bachhuber, R. Witter, C. Brankman, C. E. Randolph, A. Barka, W. D. Page, and A. Kaya (2002). Influence of releasing step-overs on surface fault rupture and fault segmentation: Examples from the 17 August 1999 İzmit earthquake on the North Anatolian fault, Turkey, *Bull. Seismol. Soc. Am.* **92**, 19–42.
- Luco, N., B. R. Ellingwood, R. O. Hamburger, J. D. Hooper, J. K. Kimball, and C. Kircher (2007). Risk-targeted versus current seismic design maps for the conterminous United States, *SEAOC 2007 Convention Proc.*, Structural Engineers Association of California, Lake Tahoe, California, 26–29 September 2007.
- Machette, M., K. Haller, and L. Wald (2004). Quaternary Fault and Fold Database for the nation, *USGS Fact Sheet FS2004-3033*, 2 pp.
- Madden, C., D. E. Haddad, J. B. Salisbury, O. Zielke, J. R. Arrowsmith, R. J. Weldon II, and J. Colunga (2013). Appendix R: Compilation of slip in the last event data and analysis of last event, repeated slip, and average displacement for recent and prehistoric ruptures, *U.S. Geol. Surv. Open-File Rept.* 2013-1165-R, and *California Geol. Surv. Special Rept.* 228-R.
- Masson, F., J. Chéry, D. Hatzfeld, J. Martinod, P. Vernant, F. Tavakoli, and M. Ghafory-Ashtiani (2005). Seismic versus aseismic deformation in Iran inferred from earthquakes and geodetic data, *Geophys. J. Int.* **160**, 217–226, doi: [10.1111/j.1365-246X.2004.02465.x](https://doi.org/10.1111/j.1365-246X.2004.02465.x).
- McCaffrey, R. (2002). Crustal block rotations and plate coupling, in *Plate Boundary Zones, Geodynamics Series*, S. Stein and J. Freymueller (Editors), Vol. 30, American Geophysical Union, Washington, D.C., 101–122.
- McCaffrey, R. (2005). Block kinematics of the Pacific/North America plate boundary in the southwestern United States from inversion of GPS, seismological, and geologic data, *J. Geophys. Res.* **110**, no. B07401, doi: [10.1029/2004JB003307](https://doi.org/10.1029/2004JB003307).
- Meng, L., J.-P. Ampuero, J. Stock, Z. Duputel, Y. Luo, and V. C. Tsai (2012). Earthquake in a maze: Compressional rupture branching during the 2012 M_w 8.6 Sumatra earthquake, *Science* **337**, 724–726, doi: [10.1126/science.1224030](https://doi.org/10.1126/science.1224030).
- Milner, K. R., M. T. Page, E. H. Field, T. Parsons, G. P. Biasi, and B. E. Shaw (2013c). Appendix T: Defining the inversion rupture set via plausibility filters, *U.S. Geol. Surv. Open-File Rept.* 2013-1165-T, and *California Geol. Surv. Special Rept.* 228-T.
- National Research Council (2011). Hamilton, R. M., R. A. Andrews, R. A. Bauer, J. A. Bullock, S. E. Chang, W. T. Holmes, L. A. Johnson, T. H. Jordan, G. A. Kreps, S. P. Nishenko, A. Z. Rose, L. T. Tobin, and A. S. Whittaker, *National Earthquake Resilience: Research, Implementation, and Outreach*, National Research Council, National Academies Press, Washington, D.C., 198 pp.
- Noda, H., and N. Lapusta (2013). Stable creeping fault segments can become destructive as a result of dynamic weakening, *Nature* **493**, 518–521, doi: [10.1038/nature11703](https://doi.org/10.1038/nature11703).
- Ogata, Y. (1988). Statistical models of point occurrences and residual analysis for point processes, *J. Am. Stat. Assoc.* **83**, 9–27.
- Page, M. T., D. Alderson, and J. Doyle (2011). The magnitude distribution of earthquakes near southern California faults, *J. Geophys. Res.* **116**, no. B12309, doi: [10.1029/2010JB007933](https://doi.org/10.1029/2010JB007933).
- Page, M. T., E. H. Field, K. R. Milner, and P. M. Powers (2013). Appendix N: Grand inversion implementation and testing, *U.S. Geol. Surv. Open-File Rept.* 2013-1165-N, and *California Geol. Surv. Special Rept.* 228-N.
- Page, M. T., E. H. Field, K. R. Milner, and P. M. Powers (2014). The UCERF3 grand inversion: Solving for the long-term rate of ruptures in a fault system, *Bull. Seismol. Soc. Am.* **104**, doi: [10.1785/0120130180](https://doi.org/10.1785/0120130180).
- Pancha, A., J. G. Anderson, and C. Kreemer (2006). Comparison of seismic and geodetic scalar moment rates across the Basin and Range

- Province, *Bull. Seismol. Soc. Am.* **96**, 11–32, doi: [10.1785/0120040166](https://doi.org/10.1785/0120040166).
- Parsons, T., and E. L. Geist (2009). Is there basis for preferring characteristic earthquakes over Gutenberg-Richter distributions on individual faults in probabilistic earthquake forecasting? *Bull. Seismol. Soc. Am.* **99**, 2012–2019, doi: [10.1785/0120080069](https://doi.org/10.1785/0120080069).
- Parsons, T., K. M. Johnson, P. Bird, J. M. Bormann, T. E. Dawson, E. H. Field, W. C. Hammond, T. A. Herring, R. McCaffrey, Z.-K. Shen, W. R. Thatcher, R. J. Weldon II, and Y. Zeng (2013). Appendix C: Deformation models for UCERF3.3, *U.S. Geol. Surv. Open-File Rept. 2013-1165-C*, and *California Geol. Surv. Special Rept. 228-C*.
- Petersen, M. D., T. Cao, K. W. Campbell, and A. D. Frankel (2007). Time-independent and time-dependent seismic hazard assessment for the State of California: Uniform California Earthquake Rupture Forecast Model 1.0, *Seismol. Res. Lett.* **78**, 99–109.
- Petersen, M. D., A. D. Frankel, S. C. Harmsen, C. S. Mueller, K. M. Haller, R. L. Wheeler, R. L. Wesson, Y. Zeng, O. S. Boyd, D. M. Perkins, N. Luco, E. H. Field, C. J. Wills, and K. S. Rukstales (2008). Documentation for the 2008 update of the United States National Seismic Hazard Maps, *U.S. Geol. Surv. Open-File Rept. 2008-1128*.
- Petersen, M. D., C. S. Mueller, A. Frankel, and Y. Zeng (2007). Spatial seismicity rates and maximum magnitudes for background earthquakes, *U.S. Geol. Surv. Open-File Rept. 2007-1437-J*.
- Plesch, A., J. Shaw, C. Benson, W. Bryant, S. Carena, M. Cooke, J. Dolan, G. Fuis, E. Gath, L. Grant, E. Hauksson, T. Jordan, M. Kamerling, M. Legg, S. Lindvall, H. Magistrale, C. Nicholson, N. Niemi, M. Oskin, S. Perry, G. Planansky, T. Rockwell, P. Shearer, C. Sorlien, M. Süs, J. Suppe, J. Treiman, and R. Yeats (2007). Community fault model (CFM) for southern California, *Bull. Seismol. Soc. Am.* **97**, 1793–1802, doi: [10.1785/0120050211](https://doi.org/10.1785/0120050211).
- Porter, K. A., E. H. Field, and K. Milner (2012). Trimming the UCERF2 hazard logic tree, *Seismol. Res. Lett.* **83**, 815–828, doi: [10.1785/0220120012](https://doi.org/10.1785/0220120012).
- Powers, P. M., and E. H. Field (2013). Appendix O: Gridded seismicity sources, *U.S. Geol. Surv. Open-File Rept. 2013-1165-O*, and *California Geol. Surv. Special Rept. 228-O*.
- Reasenber, P. A., T. C. Hanks, and W. H. Bakun (2003). An empirical model for earthquake probabilities in the San Francisco Bay region, California 2002–2031, *Bull. Seismol. Soc. Am.* **93**, 1–13.
- Reid, H. F. (1911). The elastic-rebound theory of earthquakes, *Univ. Calif. Pub. Bull. Dept. Geol. Sci.* **6**, 413–444.
- Rontogianni, S. (2008). Comparison of geodetic and seismic strain rates in Greece by using a uniform processing approach to campaign GPS measurements over the interval 1994–2000, *J. Geodyn.* doi: [10.1016/j.jog.2010.04.008](https://doi.org/10.1016/j.jog.2010.04.008).
- Rundle, P. B., J. B. Rundle, K. F. Tiampo, A. Donnellan, and D. L. Turcotte (2006). Virtual California: Fault model, frictional parameters, applications, *Pure Appl. Geophys.* **163**, no. 9, 1819–1846.
- Savage, J. C., and M. Lisowski (1993). Inferred depth of creep on the Hayward fault, central California, *J. Geophys. Res.* **98**, no. B1, 787–793.
- Schorlemmer, D., M. C. Gerstenberger, S. Wiemer, D. D. Jackson, and D. A. Rhoades (2007). Earthquake likelihood model testing, *Seismol. Res. Lett.* **78**, 17–29.
- Segall, P., and D. D. Pollard (1980). Mechanics of discontinuous faults, *J. Geophys. Res.* **85**, 4337–4350.
- Senior Seismic Hazard Analysis Committee (1997). *Recommendations for Probabilistic Seismic Hazard Analysis: Guidance on Uncertainty and Use of Experts*, U.S. Nuclear Regulatory Commission, U.S. Dept. of Energy, Electric Power Research Institute; NUREG/CR-6372, UCRL-ID-122160, Vol. 1/2. (Also a review of the document by National Academy Press, Washington, D.C., 73 pp.)
- Shaw, B. E. (2009). Constant stress drop from small to great earthquakes in magnitude-area scaling, *Bull. Seismol. Soc. Am.* **99**, 871, doi: [10.1785/0120080006](https://doi.org/10.1785/0120080006).
- Shaw, B. E. (2013a). Earthquake surface slip-length data is fit by constant stress drop and is useful for seismic hazard analysis, *Bull. Seismol. Soc. Am.* **103**, 876, doi: [10.1785/0120110258](https://doi.org/10.1785/0120110258).
- Shaw, B. E. (2013b). Appendix E: Evaluation of magnitude-scaling relationships and depth of rupture: Recommendation for UCERF3, *U.S. Geol. Surv. Open-File Rept. 2013-1165-E*, and *California Geol. Surv. Special Rept. 228-E*.
- Shaw, B. E., and J. H. Dieterich (2007). Probabilities for jumping fault segment stepovers, *Geophys. Res. Lett.* **34**, L01307, doi: [10.1029/2006GL027980](https://doi.org/10.1029/2006GL027980).
- Tullis, T. E., K. Richards-Dinger, M. Barall, J. H. Dieterich, E. H. Field, E. M. Heien, L. H. Kellogg, F. F. Pollitz, J. B. Rundle, M. K. Sachs, D. L. Turcotte, S. N. Ward, and M. B. Yikilmaz (2012). A comparison among observations and earthquake simulator results for the allcal2 California fault model, *Seismol. Res. Lett.* **83**, 994–1006.
- van Stiphout, T., S. Wiemer, and W. Marzocchi (2010). Are short-term evacuations warranted? Case of the 2009 L'Aquila earthquake, *Geophys. Res. Lett.* **37**, doi: [10.1029/2009gl042352](https://doi.org/10.1029/2009gl042352).
- Wald, D. J., B. C. Worden, K. Lin, and K. Pankow (2005). ShakeMap manual: technical manual, user's guide, and software guide, *U.S. Geol. Surv. Tech. Methods 12-A1*, 132 pp.
- Ward, S. N. (1998). On the consistency of earthquake moment release and space geodetic strain rates: Europe, *Geophys. J. Int.* **135**, 1011–1018, doi: [10.1046/j.1365-246X.1998.t01-2-00658.x](https://doi.org/10.1046/j.1365-246X.1998.t01-2-00658.x).
- Ward, S. N. (2000). San Francisco Bay area earthquake simulations: A step toward a standard physical earthquake model, *Bull. Seismol. Soc. Am.* **90**, 370–386.
- Weichert, D. H. (1980). Estimation of the earthquake recurrence parameters for unequal observation periods for different magnitudes, *Bull. Seismol. Soc. Am.* **70**, 1337–1346.
- Weldon, R. J., II, and G. P. Biasi (2013). Appendix I: Probability of detection of ground rupture at paleoseismic sites, *U.S. Geol. Surv. Open-File Rept. 2013-1165-I*, and *California Geol. Surv. Special Rept. 228-I*.
- Weldon, R. J., II, G. P. Biasi, C. J. Wills, and T. E. Dawson (2007). Overview of the southern San Andreas fault model; Appendix E in the Uniform California Earthquake Rupture Forecast, version 2 (UCERF 2), *U.S. Geol. Surv. Open-File Rept. 2007-1437-E*, and *California Geol. Surv. Special Rept. 203-E*.
- Weldon, R. J., II, T. E. Dawson, and C. Madden (2013). Appendix G: Paleoseismic sites recurrence database, *U.S. Geol. Surv. Open-File Rept. 2013-1165-G*, and *California Geol. Surv. Special Rept. 228-G*.
- Weldon, R. J., II, D. A. Schmidt, L. J. Austin, E. M. Weldon, and T. E. Dawson (2013). Appendix D: Compilation of creep rate data for California faults and calculation of moment reduction due to creep, *U.S. Geol. Surv. Open-File Rept. 2013-1165-D*, and *California Geol. Surv. Special Rept. 228-D*.
- Wells, D. (2013). Updated empirical relationships among magnitude, rupture area, rupture length, and surface displacement (abstract), *Seismol. Res. Lett.* **84**, 309.
- Wells, D. L., and K. J. Coppersmith (1994). New empirical relationships among magnitude, rupture length, rupture width, rupture area and surface displacement, *Bull. Seismol. Soc. Am.* **84**, 974–1002.
- Wesnousky, S. G. (2006). Predicting the endpoints of earthquake ruptures, *Nature* **444**, 358–360, doi: [10.1038/nature05275](https://doi.org/10.1038/nature05275).
- Working Group on California Earthquake Probabilities (WGCEP) (1988). Probabilities of large earthquakes occurring in California on the San Andreas fault, *U.S. Geol. Surv. Open-File Rept. 88-398*, 62 pp.
- Working Group on California Earthquake Probabilities (WGCEP) (1990). Probabilities of large earthquakes in the San Francisco Bay region, California, *U.S. Geol. Surv. Circ. 1053*, 51 pp.
- Working Group on California Earthquake Probabilities (WGCEP) (1995). Seismic hazards in southern California: probable earthquakes, 1994–2024, *Bull. Seismol. Soc. Am.* **85**, 379–439.
- Working Group on California Earthquake Probabilities (WGCEP) (2003). Earthquake probabilities in the San Francisco Bay region: 2002–2031, *U.S. Geol. Surv. Open-File Rept. 2003-214*.

- Working Group on California Earthquake Probabilities (WGCEP) (2007). The Uniform California Earthquake Rupture Forecast, Version 2 (UCERF 2), *U.S. Geol. Surv. Open-File Rept. 2007-1437*.
- Zechar, J. D., D. Schorlemmer, M. Liukis, J. Yu, F. Euchner, P. J. Maechling, and T. H. Jordan (2010). The Collaboratory for the Study of Earthquake Predictability perspectives on computational earth science, *Concurrency Computat. Pract. Exper.* **22**, 1836–1847, doi: [10.1002/cpe.1519](https://doi.org/10.1002/cpe.1519).
- Zechar, J. D., D. Schorlemmer, M. J. Werner, M. C. Gerstenberger, D. A. Rhoades, and T. H. Jordan (2013). Regional Earthquake Likelihood Models I: First-order results, *Bull. Seismol. Soc. Am.* **103**, 787–798.
- Zeng, Y., and Z.-K. Shen (2014). Fault network modeling of crustal deformation in California constrained using GPS and geologic observations, *Tectonophysics* **612/613**, 1–17, doi: [10.1016/j.tecto.2013.11.030](https://doi.org/10.1016/j.tecto.2013.11.030).
- U.S. Geological Survey, Denver Federal Center
PO Box 25046, MS 966
Denver, Colorado 80225-0046
(E.H.F., P.M.P., Y.Z.)
- Arizona State University
School of Earth and Space Exploration
PO Box 876004
Tempe, Arizona 85287-6004
(R.J.A.)
- University of Nevada Reno
Nevada Seismological Laboratory MS-174
1664 N. Virginia St.
Reno, Nevada 89557
(G.P.B.)
- Department of Earth, Planetary, & Space Sciences
University of California
Los Angeles, California 90095-1567
(P.B., D.D.J.)
- California Geological Survey
345 Middlefield Road MS 520
Menlo Park, California 94025
(T.E.D., A.J.M., T.P.)
- U.S. Geological Survey
525 S. Wilson Avenue
Pasadena, California 91106
(K.R.F., M.T.P.)
- Department of Geological Sciences
Indiana University
1001 E. 10th St.
Bloomington, Indiana 47405
(K.M.J.)
- University of Southern California
Southern California Earthquake Center
3651 Trousdale Parkway #169
Los Angeles, California, 90089-0742
(T.H.J., K.R.M.)
- College of Earth, Ocean, and Atmospheric Sciences
Oregon State University
104 CEOAS Administration Building
Corvallis, Oregon 97331-5503
(C.M.)
- Lamont Doherty Earth Observatory
Columbia University
Palisades, New York 10964
(B.E.S.)
- U.S. Geological Survey MS 977
345 Middlefield Road
Menlo Park, California 94025
(W.R.T.)
- Department of Geological Sciences
University of Oregon
Eugene, Oregon 97403-1272
(R.J.W.)

Manuscript received 17 June 2013